Theoretical Study on Spin-Dependent Two-Component Relativistic Wavefunction Method

スピンに依存した 2 成分相対論的波動関数法に関する理論的研究

June 2017

Masahiko NAKANO
中野　匡彦

Theoretical Study on Spin-Dependent Two-Component Relativistic Wavefunction Method

スピンに依存した 2 成分相対論的波動関数法に関する理論的研究

June 2017

Waseda University
Graduate School of Advanced Science and Engineering
Department of Chemistry and Biochemistry,
Research on Electronic State Theory

Masahiko NAKANO
中野　匡彦

Contents

Acronyms and abbreviations

The following acronyms and abbreviations are adopted throughout this thesis. Several abbreviations not included in this list are defined as combinations of these acronyms/abbreviations.

AO	atomic orbital
AOC	average of configuration
BPD	Binkley–Pople–Dobosh
BSS	Barysz–Sadlej–Snijders
CBS	complete-basis-set
CC	coupled-cluster
CCSD	coupled-cluster singles and doubles
CCSDT	coupled-cluster singles, doubles, and triples
CCSDTQ	coupled-cluster singles, doubles, triples, and quadruples
CCSD(T)	coupled-cluster singles, doubles with a perturbative triples correction
$CCSD(2)_{TQ}$	coupled-cluster singles and doubles with second-order triples and quadruples corrections
CI	configuration interaction
D	Davidson
DC	Dirac–Coulomb
DCB	Dirac–Coulomb–Breit
D&C	divide-and-conquer
DFT	density functional theory
DIIS	direct inversion in the iterative subspace

DKH	Douglas–Kroll–Hess
DKH*n*	*n*th-order Douglas–Kroll–Hess
DODS	different orbitals for different spins
EA	electron affinity
EDA	energy density analysis
EDIIS	energy direct inversion in the iterative subspace
EE	Euler equations
FM	Fægri–Manne
FOA	frozen-orbital approximation
FP	fixed point
FW	Foldy–Wouthuysen
GHF	generalized Hartree–Fock
GMP2	second-order generalized Møller–Plesset perturbation theory
GS	Guest–Saunders
GSO	generalized spin-orbital
HF	Hartree–Fock
HS	highest spin
IODKH	infinite-order Douglas–Kroll–Hess
IODKH/IODKH	infinite-order Douglas–Kroll–Hess method for many-electron systems
IOTC	infinite-order two-component
IP	ionization potential
KROHF	Kramers-restricted open-shell Hartree–Fock
KRHF	Kramers-restricted Hartree–Fock
KT	Koopmans' theorem
KUHF	Kramers-unrestricted Hartree–Fock
LS	lowest spin

LUT	local unitary transformation
MaxAD	maximum absolute deviation
MD	McWeeny–Diercksen
MO	molecular orbital
MS	molecular spinor
MP	Møller–Plesset
MP*n*	*n*th-order Møller–Plesset perturbation theory
MPPT	Møller–Plesset perturbation theory
NESC	normalized elimination of the small components
NR	non-relativistic
PGB	Plakhutin–Gorelik–Breslavskaya
R	Roothaan
RA	regular approximation
RESC	relativistic scheme by eliminating small components
RH	Roothaan–Hall
RHF	restricted Hartree–Fock
ROHF	restricted open-shell Hartree–Fock
RS	Rayleigh–Schrödinger
SCF	self-consistent field
SD	spin-dependent
SESC	symmetrized elimination of the small components
SF	spin-free
SO	spin–orbit
SODS	same orbitals for different spins
TCE	tensor contraction engine
TSCW	torsional spin current wave
TSW	torsional spin wave

UESC	unnormalized elimination of the small components
UHF	unrestricted Hartree–Fock
UMP2	second-order unrestricted Møller–Plesset perturbation theory
X2C	exact two-component
ZORA	zeroth-order regular approximation

The nomenclature of two-component Hamiltonians in this thesis is as follows:

$$SS\text{-}OOOOO/TTTTT, \tag{1}$$

where *SS* denotes the level of the treatment of spin (SF or SD), and *OOOOO* and *TTTTT* denote the levels of one- and two-electron parts of the Hamiltonian (NR, DKH*n*, IODKH, and so forth), respectively. For example, SF-IODKH/NR represents *the one-electron IODKH Hamiltonian with the two-electron NR Coulomb interaction in the SF formalism*.

Chapter 1

General introduction

Quantum chemical calculation is a powerful tool to analyze or predict chemical and physical properties of atoms and molecules such as structures, interactions, and reactivities. Large-scale quantum chemical calculations can now be readily performed with a high degree of accuracy for organic- or bio-molecules consisting of light elements through the recent development of sophisticated theories and programs. In contrast, accurate and efficient black-box treatment is still difficult for molecules including heavy elements, since relativistic effects, which are vital in the chemical and physical properties of heavy elements, are not appropriately considered by many quantum chemical programs.

Relativistic effects are classified into SF and SD effects [1]. The SF effects, including the so-called mass-velocity and Darwin interactions, mainly contribute to the contraction of s/p-orbitals and the expansion of d/f-orbitals. The SD effects, including the SO and other magnetic interactions, contribute to the energy level splitting and the coupling of multiple spin states, which results in phosphorescence and inter-system crossing. Theories and algorithms that can appropriately describe these relativistic effects in the quantum chemical calculations must be based on wave equations that satisfy the Lorentz invariance, i.e., the fundamental physical condition arising from special relativity, instead of the NR Schrödinger equation.

Modern relativistic quantum chemistry is based on the Dirac equation [2], which is Lorentz-invariant with respect to the motion of a single electron. The Dirac-equation-based formalism is called the four-component method because the wavefunction of the

Dirac equation contains four components, corresponding to electrons and positrons each with both alpha- and beta-spins.

A wide variety of two-component methods have been developed to describe only the electronic states, which play an important role in chemistry, by decoupling them from the positronic states using several mathematical operations [3,4]. The two-component methods remedy many of the problems that occur in the four-component methods: for example, the enormous computational cost and difficulty of obtaining a physical interpretation of the solutions due to the positronic components. Since the development of the IODKH method by Barysz, Sadlej, and Snijders in 2002 [5-8], the X2C method [9-13], which exactly reproduces the solutions of the four-component Dirac equation, has become the standard two-component approach. The IODKH and X2C methods were originally developed for one-electron systems. The IODKH/IODKH method proposed by Seino and Hada in 2008 achieved highly accurate two-component calculations for many-electron systems [14]. Furthermore, the LUT scheme proposed by Seino and Nakai in 2012 enables more efficient two-component relativistic quantum chemical calculations, with computational costs that scale linearly [15-17].

The two-component relativistic quantum chemical calculations are typically based on the GHF method [18-27]. GHF defines an orbital by the superposition of alpha and beta spin bases, enabling each spin-quantized axis to rotate independently. Thus, GHF can describe non-collinear spin states, i.e., non-one-dimensional spin orientations, which are seen in electronic structures under SO interactions and geometrically frustrated spin systems, for example. Through these two-component relativistic quantum chemical calculations, one can, in principle, analyze the electronic structures of heavy-element or non-collinear spin systems. However, there are many barriers to be overcome from the

viewpoint of routinely performing these calculations. For example, the low convergence behavior of the SCF procedure in GHF calculations that consider the SD relativistic effects is problematic. The interpretation of the calculated results is complicated by the hybridization of multiple spin states. Therefore, methods that consider the SD relativistic effect in a post-treatment to NR or SF relativistic calculations have been widely used [1,28]. Although this type of treatment is effective for light-element systems, the relativistic effects in heavy-element systems cannot be treated correctively. The relativistic effects must be rigorously considered from the HF stage to obtain results that are qualitatively and quantitatively reasonable across the whole periodic table.

In the context of these challenges, the author herein has developed highly accurate and efficient SD two-component relativistic wavefunction methods based mainly on the IODKH and IODKH/IODKH methods. This thesis consists of eight chapters, including the general introduction mentioned in this chapter. The outline of each chapter is as follows.

In Chapter 2, the theoretical background of the present thesis is summarized. The basic concepts and equations of the four- and two-component methods, IODKH-related methods, and two-component HF methods including GHF and KRHF [29-32] are briefly reviewed. The author also tackled the development of theoretical methodologies in the SF framework, although the present thesis mainly focuses on those in the SD framework. Their low computational cost allows the SF calculations to act as a valuable initial assessment for the SD calculations. Thus, Chapter 2 also reports the implementation of higher-order electron correlation methods in accordance with the SF relativistic Hamiltonians and their extension to the linear-scaling D&C scheme [33-35] using TCE [36-42], which is a computerized symbolic algebra system. TCE supports the derivation

and implementation of the complicated working equations of the higher-order correlation methods. Numerical assessments demonstrate that the D&C-based higher-order correlation methods provide reliable correlation energies with significantly less computational cost than the D&C-free methods.

Chapter 3 assesses the SCF convergence behavior of the GHF method, which is one of the practical problems in SD calculations. Four acceleration algorithms are implemented to obtain efficient SCF convergence of GHF: the damping algorithm, DIIS algorithm [43,44], EDIIS algorithm [45], and a combination of the DIIS and EDIIS algorithms [45,46]. Numerical assessments demonstrate the effectiveness of the DIIS and EDIIS combination algorithm for GHF calculations in comparison with the other discussed algorithms.

In Chapters 4 and 5, new types of the two-component HF methods are proposed based on time-reversal symmetry. The problems in the GHF method, including the poor SCF convergence behavior, are mainly due to the absence of spin-related symmetry constraints in the GHF wavefunction. The KRHF method, which preserves time-reversal symmetry, is another representative scheme for SD calculations. However, KRHF is applicable only in closed-shell systems. These chapters develop KUHF and KROHF, i.e., two-component HF methods for open-shell systems that partially and fully preserve time-reversal symmetry, respectively. Chapter 4 discusses the KUHF method. Numerical assessments demonstrate that KUHF gives wavefunctions that are simpler than GHF and similar to UHF wavefunctions, with better SCF convergence behavior. Chapter 5 discusses the KROHF method. The ambiguity of the KROHF Fock operator affects the spinor energy values and SCF convergence behavior. The use of a canonical parametrization of KROHF to satisfy KT and obtain physically meaningful spinor energies is discussed.

Chapter 6 extends the IODKH and IODKH/IODKH methods to the GMP2 method [47-50], i.e., one of the fundamental electron correlation theories that use the GHF wavefunction as a reference state, to improve computational accuracy. The author has derived and implemented a universal formulation of the GMP2 method in accordance with SD two-component many-electron Hamiltonians. Numerical assessments demonstrate that the present GMP2 method using the SD-IODKH/IODKH Hamiltonian reproduces the correlation energies of the four-component MP2 method with less computational cost.

In Chapter 7, an application of the two-component methods developed in the previous chapters to frustrated spin systems is demonstrated. This chapter focuses on equilateral hydrogen rings, which are representative examples of molecules with frustrated spin characteristics. The basic properties of these systems are examined from the viewpoint of potential energy curves and spin expectation values using the GHF and GMP2 methods.

Finally, in Chapter 8, the general conclusion and prospects of this thesis are presented.

References

[1] K. G. Dyall, K. Faegri, Introduction to Relativistic Quantum Chemistry, Oxford University Press, New York, 2007.

[2] P. A. M. Dirac, *Proc. R. Soc. London, Ser. A* **117**, 610 (1928).

[3] W. Liu, *Mol. Phys.* **108**, 1679 (2010).

[4] T. Saue, *ChemPhysChem* **12**, 3077 (2011).

[5] M. Barysz, A. J. Sadlej, J. G. Snijders, *Int. J. Quantum Chem.* **65**, 225 (1997).

[6] M. Barysz, *J. Chem. Phys.* **114**, 9315 (2001).

[7] M. Barysz, A. J. Sadlej, *J. Chem. Phys.* **116**, 2696 (2002).

[8] D. Kędziera, M. Barysz, *J. Chem. Phys.* **121**, 6719 (2004).

[9] M. Iliaš, T. Saue, *J. Chem. Phys.* **126**, 064102 (2007).

[10] W. Kutzelnigg, W. Liu, *J. Chem. Phys.* **123**, 241102 (2005).

[11] W. Liu, W. Kutzelnigg, *J. Chem. Phys.* **126**, 114107 (2007).

[12] W. Kutzelnigg, W. Liu, *Mol. Phys.* **104**, 2225 (2006).

[13] M. Iliaš, H. J. Aa. Jensen, V. Kellö, B. O. Roos, M. Urban, *Chem. Phys. Lett.* **408**, 210 (2005).

[14] J. Seino, M. Hada, *Chem. Phys. Lett.* **461**, 327 (2008).

[15] J. Seino, H. Nakai, *J. Chem. Phys.* **136**, 244102 (2012).

[16] J. Seino, H. Nakai, *J. Chem. Phys.* **137**, 144101 (2012).

[17] J. Seino, H. Nakai, *J. Chem. Phys.* **139**, 034109 (2013).

[18] R. Seeger, J. A. Pople, *J. Chem. Phys.* **66**, 3045 (1977).

[19] H. Fukutome, *Int. J. Quantum Chem.* **20**, 955 (1981).

[20] J.-L. Calais, *Adv. Quantum Chem.* **17**, 225 (1985).

[21] R. McWeeny, Methods of Molecular Quantum Mechanics, Academic Press, London,

1989.

[22] P.-O. Löwdin, I. Mayer, *Adv. Quantum Chem.* **24**, 79 (1992).

[23] S. Hammes-Schiffer, H. C. Andersen, *J. Chem. Phys.* **99**, 1901 (1993).

[24] S. K. Wolff, D. Jayatilaka, G. S. Chandler, *J. Chem. Phys.* **103**, 4562 (1995).

[25] D. Jayatilaka, *J. Chem. Phys.* **108**, 7587 (1998).

[26] J. L. Stuber, J. Paldus, in: E. J. Brändas, E. S. Kryachko (Eds.), Fundamental World of Quantum Chemistry, Kluwer Academic Publishers, Dordrecht, 2003, p. 67.

[27] M. K. Armbruster, F. Weigend, C. van Wüllen, W. Klopper, *Phys. Chem. Chem. Phys.* **10**, 1748 (2008).

[28] P. Schwerdtfeger, Relativistic Electronic Structure Theory, Part 2. Applications, Elsevier Science, Amsterdam, 2004.

[29] P. Hafner, W. H. E. Schwarz, *Chem. Phys. Lett.* **65**, 537 (1979).

[30] P. Hafner, *J. Phys. B: At., Mol. Opt. Phys.* **13**, 3297 (1980).

[31] N. Rösch, *Chem. Phys.* **80**, 1 (1983).

[32] S. Y. Lee, Y. S. Lee, *J. Comput. Chem.* **13**, 595 (1992).

[33] W. Yang, *Phys. Rev. Lett.* **66**, 1438 (1991).

[34] M. Kobayashi, H. Nakai, in: R. Zaleśny, M. G. Papadopoulos, P. G. Mezey, J. Leszczynski (Eds.), Linear-Scaling Techniques in Computational Chemistry and Physics, Springer, Dordrecht, 2011, p. 97.

[35] M. Kobayashi, H. Nakai, *Phys. Chem. Chem. Phys.* **14**, 7629 (2012).

[36] S. Hirata, *Theor. Chem. Acc.* **116**, 2 (2006).

[37] S. Hirata, *J. Phys. Chem. A* **107**, 9887 (2003).

[38] S. Hirata, *J. Chem. Phys.* **121**, 51 (2004).

[39] S. Hirata, P. D. Fan, A. A. Auer, M. Nooijen, P. Piecuch, *J. Chem. Phys.* **121**, 12197

(2004).

[40] S. Hirata, *J. Chem. Phys.* **122**, 094105 (2005).

[41] P. D. Fan, S. Hirata, *J. Chem. Phys.* **124**, 104108 (2006).

[42] M. Kamiya, S. Hirata, *J. Chem. Phys.* **125**, 074111 (2006).

[43] P. Pulay, *Chem. Phys. Lett.* **73**, 393 (1980).

[44] P. Pulay, *J. Comput. Chem.* **3**, 556 (1982).

[45] K. N. Kudin, G. E. Scuseria, E. Cancès, *J. Chem. Phys.* **116**, 8255 (2002).

[46] A. J. Garza, G. E. Scuseria, *J. Chem. Phys.* **137**, 054110 (2012).

[47] D. Yamaki, Y. Shigeta, S. Yamanaka, H. Nagao, K. Yamaguchi, *Int. J. Quantum Chem.* **80**, 701 (2000).

[48] R. Fukuda, H. Nakatsuji, *J. Chem. Phys.* **123**, 044101 (2005).

[49] T. Yoshizawa, M. Hada, *J. Comput. Chem.* **30**, 2550 (2009).

[50] Y. S. Kim, S. Y. Lee, W. S. Oh, B. H. Park, Y. K. Han, S. J. Park, Y. S. Lee, *Int. J. Quantum Chem.* **66**, 91 (1998).

Chapter 2

Theoretical background

Modern relativistic quantum chemistry is established based on the four-component method, which directly solves the Dirac equation [1]. Unlike the NR Schrödinger equation, the solutions of the Dirac equation are multi-dimensional and mathematically complicated, because they include the positronic states as well as the electronic states. In addition, the existence of the positron-derived small components increases the computational cost of the construction of the four-component Hamiltonian matrix and its diagonalization. Thus, a broad range of the two-component methods, which handle only the electronic states, have been developed through the block-diagonalization of the four-component Hamiltonian by a unitary transformation or the algebraic elimination of the small components. The equivalence of these two derivation approaches is shown in Ref. [2].

The two-component methods are classified from the viewpoint of the algorithm and accuracy. Two major algorithms are used for the two-component calculations, termed the operator and matrix formulations [3]. In the operator formulation, the analytical two-component electronic Hamiltonian is first derived, and the matrix representation of the Hamiltonian is then constructed. In the matrix formulation, in contrast, the matrix representation of the four-component Hamiltonian is first built, and the algebraic two-component Hamiltonian is then constructed. There are also two main categories of two-component methods with respect to the degree of accuracy: the approximate and exact decoupling procedures. Originally, the decoupling of the positronic states was achieved

approximately. The approximate two-component Hamiltonians are correct to a finite order with respect to the reciprocal of the speed of light in comparison with the parent four-component Hamiltonian. For example, the FW [4], DKH [5-12], RA [13-16], and RESC [17] methods are the approximate approaches in the operator formulation; the UESC [18], NESC [18-20], and SESC [21] are the approximate approaches in the matrix formulation. Since the development of the IODKH method (also called the BSS or IOTC method) by Barysz et al. [22-25], several exact decoupling procedures, which reproduce the solutions of the four-component Hamiltonian, have been proposed. The IODKH method is classified as the exact approach in the operator formulation. The one-step [2,26-28] and two-step [29] X2C methods are other exact approaches, which are classified as matrix formulations.

In the present thesis, the author focuses on the IODKH method for the following three reasons. Firstly, the IODKH method provides the accurate and numerically stable Hamiltonian. Secondly, the IODKH method has been extended to the calculations for many-electron systems: the IODKH/IODKH method [30]. Thirdly, an efficient computational technique, termed the LUT method [31,32], has been proposed for the IODKH method (also for the IODKH/IODKH method).

In the two-component methods including IODKH and IODKH/IODKH, the NR wavefunction theories cannot be used in an as-is manner. This is because the two-component Hamiltonians include the SD terms, which results in the spin symmetry breaking of the two-component wavefunction. In addition, the SD terms also lead to the complex wavefunction. For an appropriate description of the SD terms, the complex GHF method [33-42], which does not impose any symmetry constraints, is required. In the case of the two-component calculations for closed-shell systems, the KRHF method [43-46]

can also be used. KRHF exploits time-reversal symmetry corresponding to the generalization of the spin symmetry.

By neglecting the SD terms of the two-component Hamiltonians, the same computational framework can be applied as that used in the NR case. This type of treatment is referred to as the SF, scalar relativistic, or one-component approach. The accuracy of SF calculations is inferior to that of SD calculations in heavy-element systems because the SD terms play a crucial role. However, the computational cost of the SF calculations is lower than that of the SD calculations by one order of magnitude. Thus, the SF calculations are valuable for the initial assessment of a system under consideration, providing guidelines for further calculations that consider the SD terms. The author has also tackled the development of higher-order electron correlation methods in combination with the linear-scaling D&C scheme [47-49] within the SF framework, although the present thesis mainly focuses on the SD theories.

In this chapter, the theoretical background, key concepts, and equations for the present thesis are briefly reviewed. This chapter is organized as follows: Section 2.1 explains the four-component Dirac and DC Hamiltonians. In Sec. 2.2, the general formulation of the two-component Hamiltonians is presented. Then, the IODKH-related methods are described: the IODKH method in Sec. 2.3, the IODKH/IODKH method in Sec. 2.4, and the LUT method in Sec. 2.5. Sections 2.6 and 2.7 explain the GHF and KRHF methods, respectively. Additionally, Sec. 2.8 reports the implementation of the higher-order electron correlation methods and their extension to the D&C scheme in the SF framework.

2.1 Four-component method

The four-component method is based on the Dirac Hamiltonian [1]. The Dirac Hamiltonian for a single electron in the electrostatic potential V under the Born–Oppenheimer approximation is given by

$$h^{\mathrm{D}} = c\boldsymbol{\alpha}\cdot\mathbf{p} + \beta' c^2 + V = \begin{pmatrix} V & c\boldsymbol{\sigma}\cdot\mathbf{p} \\ c\boldsymbol{\sigma}\cdot\mathbf{p} & V - 2c^2 \end{pmatrix}, \tag{2.1}$$

where c denotes the speed of light, $\mathbf{p}$ the momentum operator, and

$$\boldsymbol{\alpha} = \begin{pmatrix} \mathbf{0}_2 & \boldsymbol{\sigma} \\ \boldsymbol{\sigma} & \mathbf{0}_2 \end{pmatrix} \tag{2.2}$$

and

$$\beta' = \begin{pmatrix} \mathbf{0}_2 & \mathbf{0}_2 \\ \mathbf{0}_2 & -2\mathbf{I}_2 \end{pmatrix} \tag{2.3}$$

the Dirac matrices in their standard representation. Here, $\mathbf{I}_n$ and $\mathbf{0}_n$ are the $n \times n$ identity and null matrices, respectively. $\boldsymbol{\sigma}$ is the set of Pauli matrices,

$$\boldsymbol{\sigma} = \left(\sigma_x, \sigma_y, \sigma_z\right), \tag{2.4}$$

where

$$\sigma_x = \begin{pmatrix} 0 & 1 \\ 1 & 0 \end{pmatrix}, \tag{2.5}$$

$$\sigma_y = \begin{pmatrix} 0 & -i \\ i & 0 \end{pmatrix}, \tag{2.6}$$

and

$$\sigma_z = \begin{pmatrix} 1 & 0 \\ 0 & -1 \end{pmatrix}. \tag{2.7}$$

One of the key features of the Dirac Hamiltonian is the Lorentz-invariance property with respect to the motion of the single electron. Namely, the spatial and time variables for an electron are treated on an equal-footing, which is the fundamental condition of the special

relativity.

The wave equation for the Dirac Hamiltonian,

$$h^{\mathrm{D}}\Psi^{4c} = E\Psi^{4c}, \tag{2.8}$$

is termed the Dirac equation, which is the relativistic counterpart of the NR Schrödinger equation. Here, E denotes the energy eigenvalues. The eigenfunctions of the Dirac equation are expressed in a four-spinor form,

$$\Psi^{4c} = \begin{pmatrix} \Psi_1 \\ \Psi_2 \\ \Psi_3 \\ \Psi_4 \end{pmatrix} = \begin{pmatrix} \Psi^{\mathrm{L}} \\ \Psi^{\mathrm{S}} \end{pmatrix}. \tag{2.9}$$

This is the reason why the Dirac-based formalism is called the four-component method. The upper (Ψ^{L}) and lower (Ψ^{S}) two-spinors are collectively termed the large- and small-components, respectively. The large- and small-components possess the positive and negative eigenvalues, respectively. The positive energy eigenvalues correspond to the electronic states. In contrast, the negative eigenvalues arise from positrons in the picture of the Dirac sea [50], where positrons are interpreted as holes of the fully-occupied negative energy states.

The Dirac Hamiltonian is defined for the one-electron system. For the straightforward extension toward many-electron systems, the two-electron NR Coulomb operator $1/r_{ij}\,\mathbf{I}_4$ is simply added to the Dirac Hamiltonian,

$$H^{\mathrm{DC}} = \sum_i h_i^{\mathrm{D}} + \sum_{i<j} \frac{1}{r_{ij}} \mathbf{I}_4, \tag{2.10}$$

where r_{ij} is the inter-electron distances, and $\{i, j\}$ refers to electrons. H^{DC} is termed the DC Hamiltonian. More rigorous relativistic treatment for the two-electron term is

available through the further addition of the Gaunt [51] or Breit [52] operators derived from quantum electrodynamics.

2.2 Two-component method

The four-component method handles both electronic and positronic states as mentioned in the previous section. In many chemical phenomena, however, the effects of positrons are usually negligible. Thus, the decoupling of the positronic states from the four-component framework provides a computationally more efficient approach. Such a method is referred to as the two-component method, which handles only the electronic states. This section provides a brief explanation of the general form of the two-component Hamiltonians.

The two-component Hamiltonians have the following generic form [53]:

$$H^{2c} = \sum_i h_i^{2c} + \sum_{i<j} g_{ij}^{2c} , \tag{2.11}$$

where h and g denote the one- and two-electron parts of the Hamiltonian, respectively. At the same level as the DC theory, the one- and two-electron parts are generalized as

$$h_i^{2c} = h_i^{SF} + h_i^{SD} \tag{2.12}$$

with

$$h_i^{SD} = \boldsymbol{\sigma}_i \cdot \boldsymbol{\Omega}_i(X_i^{SD}) \tag{2.13}$$

and

$$g_{ij}^{2c} = g_{ij}^{SF} + g_{ij}^{SD1} + g_{ij}^{SD2} + g_{ij}^{SD3} \tag{2.14}$$

with

$$g_{ij}^{\mathrm{SD1}} = \boldsymbol{\sigma}_i \cdot \boldsymbol{\Omega}_i(X_{ij}^{\mathrm{SD1}}), \tag{2.15}$$

$$g_{ij}^{\mathrm{SD2}} = \boldsymbol{\sigma}_j \cdot \boldsymbol{\Omega}_j(X_{ij}^{\mathrm{SD2}}), \tag{2.16}$$

and

$$g_{ij}^{\mathrm{SD3}} = \boldsymbol{\sigma}_i \cdot \boldsymbol{\Omega}_i\left(\boldsymbol{\sigma}_j \cdot \boldsymbol{\Omega}_j(X_{ij}^{\mathrm{SD3}})\right), \tag{2.17}$$

respectively. Here, the superscripts SF and SD indicate being the SF and SD terms, respectively; $\boldsymbol{\sigma}$ is the set of Pauli matrices [Eq. (2.4)]; X is the scalar one- and two-electron operator; and $\boldsymbol{\Omega}$ is the vectorial momentum cross-product operator,

$$\boldsymbol{\Omega}_i(X) = \mathbf{p}_i X \times \mathbf{p}_i, \tag{2.18}$$

with the momentum operator $\mathbf{p} = \left(p^x, p^y, p^z\right)$. The components of $\boldsymbol{\Omega}_i = \left(\Omega_i^x, \Omega_i^y, \Omega_i^z\right)$ are defined as

$$\Omega_i^x(X) = \left(\mathbf{p}_i X \times \mathbf{p}_i\right)_x = p_i^y X p_i^z - p_1^z X p_i^y, \tag{2.19}$$

$$\Omega_i^y(X) = \left(\mathbf{p}_i X \times \mathbf{p}_i\right)_y = p_i^z X p_i^x - p_i^x X p_i^z, \tag{2.20}$$

and

$$\Omega_i^z(X) = \left(\mathbf{p}_i X \times \mathbf{p}_i\right)_z = p_i^x X p_i^y - p_i^y X p_i^x. \tag{2.21}$$

In Eq. (2.17), $\boldsymbol{\Omega}$ is used recursively,

$$\boldsymbol{\Omega}_i(\boldsymbol{\Omega}_j(X_{ij})) = \mathbf{p}_i\left(\mathbf{p}_j X_{ij} \times \mathbf{p}_j\right) \times \mathbf{p}_i. \tag{2.22}$$

It should be noted that Eq. (2.22) has a tensor structure; that is, the electrons i and j are in completely different Hilbert spaces.

2.3 IODKH method

This section provides a brief explanation on the IODKH method [22-25], which is one of the most accurate two-component methods. In the IODKH method, the Dirac Hamiltonian of Eq. (2.1) is exactly block-diagonalized to decouple the electronic (h^+) and positronic (h^-) Hamiltonians by a unitary transformation U,

$$U_i^\dagger h_i^{\mathrm{D}} U_i = \begin{pmatrix} h_i^+ & \mathbf{0}_2 \\ \mathbf{0}_2 & h_i^- \end{pmatrix}. \tag{2.23}$$

Using the generalized notation for the two-component Hamiltonians presented in the previous section, the electronic Hamiltonian $h_i^+ = h_i^{\mathrm{IODKH}}$ obtained through the transformation is expressed as

$$\begin{aligned} h_i^{\mathrm{SF}} = \Gamma_i^\dagger \Big[& p_i^2 b_i + K_i V_i K_i + \alpha^2 K_i b_i \mathbf{p}_i V_i \cdot \mathbf{p}_i b_i K_i \\ & + \alpha \left\{ K_i V_i b_i K_i p_i - K_i b_i \mathbf{p}_i V_i \cdot \mathbf{p}_i p_i^{-1} K_i \right\} Y_i \\ & + \alpha Y_i^\dagger \left\{ K_i b_i p_i V_i K_i - K_i p_i^{-1} \mathbf{p}_i V_i \cdot \mathbf{p}_i b_i K_i \right\} \\ & + Y_i^\dagger \left\{ \frac{p_i^2}{1 - e_{p_i}} + p_i^{-1} K_i \mathbf{p}_i V_i \cdot \mathbf{p}_i K_i p_i^{-1} + \alpha^2 p_i K_i b_i V_i b_i K_i p_i \right\} Y_i \Big] \Gamma_i \mathbf{I}_2 \end{aligned} \tag{2.24}$$

and

$$\begin{aligned} X_i^{\mathrm{SD}} = i \Gamma_i^\dagger \Big[& \alpha^2 K_i b_i V_i b_i K_i - \alpha K_i b_i V_i p_i^{-1} K_i Y_i \\ & - \alpha Y_i^\dagger K_i p_i^{-1} V_i b_i K_i + Y_1^\dagger p_i^{-1} K_i V_i K_i p_i^{-1} Y_i \Big] \Gamma_i, \end{aligned} \tag{2.25}$$

where

$$\alpha = \frac{1}{c} \tag{2.26}$$

denotes the fine-structure constant;

$$K_i = \left(\frac{e_{p_i} + 1}{2e_{p_i}} \right)^{1/2}, \tag{2.27}$$

$$b_i = \frac{1}{e_{p_i} + 1}, \tag{2.28}$$

and

$$e_{p_i} = \left(1 + \alpha^2 p_i^2\right)^{1/2} \tag{2.29}$$

denote the kinematic factors. Γ_i is the normalization factor defined by

$$\Gamma_i = \frac{1}{\sqrt{1 + Y_i^\dagger Y_i}}, \tag{2.30}$$

where Y_i is determined by solving the so-called *R*-operator equation, i.e., a condition to exactly block-diagonalize the Dirac Hamiltonian,

$$\begin{aligned}
&\left(e_{p_i} Y_i + Y_i e_{p_i}\right)\mathbf{I}_2 \\
&= \alpha^3 \left(p_i K_i b_i V_i K_i \mathbf{I}_2 - p_i^{-1} K_i \mathbf{p}_i V_i \cdot \mathbf{p}_i b_i K_i \mathbf{I}_2 - i p_i^{-1} K_i \boldsymbol{\sigma}_i \cdot \boldsymbol{\Omega}_i \left(V_i\right) b_i K_i \right) \\
&+ \alpha^2 \left(p_i^{-1} K_i \mathbf{p}_i V_i \cdot \mathbf{p}_i p_i^{-1} K_i Y_i \mathbf{I}_2 + i p_i^{-1} K_i \boldsymbol{\sigma}_i \cdot \boldsymbol{\Omega}_i \left(V_i\right) p_i^{-1} K_i Y_i - Y_i K_i V_i K_i \mathbf{I}_2 \right) \\
&+ \alpha^4 \left(p_i K_i b_i V_i b_i K_i p_i Y_i \mathbf{I}_2 - Y_i K_i b_i \mathbf{p}_i V_i \cdot \mathbf{p}_i b_i K_i \mathbf{I}_2 - i Y_i K_i b_i \boldsymbol{\sigma}_i \cdot \boldsymbol{\Omega}_i \left(V_i\right) b_i K_i \right) \\
&+ \alpha^3 Y_i \left(K_i b_i \mathbf{p}_i V_i \cdot \mathbf{p}_i K_i p_i^{-1} \mathbf{I}_2 + i K_i b_i \boldsymbol{\sigma}_i \cdot \boldsymbol{\Omega}_i \left(V_i\right) K_i p_i^{-1} - K_i V_i K_i b_i p_i \mathbf{I}_2 \right) Y_i .
\end{aligned} \tag{2.31}$$

2.4 IODKH method for many-electron systems

This section explains the IODKH/IODKH method [30], which is the extension of the IODKH method for many-electron systems. For the straightforward extension, one should start from the block-diagonalization of the four-component DC Hamiltonian by a unitary transformation,

$$U^\dagger(i,j,\cdots)\left[\sum_i h_i^{\mathrm{D}} + \sum_{i<j} \frac{1}{r_{ij}} \mathbf{I}_4 \right] U(i,j,\cdots) = \sum_i \begin{pmatrix} h_i^+ & \mathbf{0}_2 \\ \mathbf{0}_2 & h_i^- \end{pmatrix} + \sum_{i<j} \begin{pmatrix} g_{ij}^{++} & \mathbf{0}_2 \\ \mathbf{0}_2 & g_{ij}^{--} \end{pmatrix}, \tag{2.32}$$

Here, h_i^+ (h_i^-) and g_{ij}^{++} (g_{ij}^{--}) denote the one- and two-particle parts of the electronic (positronic) Hamiltonian, respectively. However, the exact expression of $U(i,j,\cdots)$ cannot be analytically determined because it involves the coordinates of more-than-two particles. Thus, in the IODKH/IODKH method, the one-body approximation is adopted to define the unitary transformation: the many-body unitary transformation $U(i,j,\cdots)$ is approximately expressed by the direct product of the one-body transformation $U(i)$, which is determined in the one-electron IODKH procedure,

$$U(i,j,\cdots) \approx \bigotimes_i U(i). \tag{2.33}$$

The electron–positron decoupling in the IODKH/IODKH method is not exactly achieved due to this approximation on the unitary transformation. However, the off-diagonal components of the transformed two-electron part are negligibly small, because the two-electron relativistic interaction is commonly smaller than the one-electron interaction. Consequently, the transformed two-electron part of the Hamiltonian $g_{ij}^{++} \approx g_{ij}^{\mathrm{IODKH}}$ is expressed as

$$\begin{aligned} g_{ij}^{\mathrm{SF}} = \Bigg\{ & M_i M_j \frac{1}{r_{ij}} M_j M_i + d_i M_j \mathbf{p}_i \frac{1}{r_{ij}} \cdot \mathbf{p}_i M_j d_i \\ & + M_i d_j \mathbf{p}_j \frac{1}{r_{ij}} \cdot \mathbf{p}_j d_j M_i + d_i d_j \mathbf{p}_i \left(\mathbf{p}_j \frac{1}{r_{ij}} \cdot \mathbf{p}_j \right) \cdot \mathbf{p}_i d_j d_i \Bigg\} \mathbf{I}_2, \end{aligned} \tag{2.34}$$

$$X_{ij}^{\mathrm{SD1}} = i \left(d_i M_j \frac{1}{r_{ij}} M_j d_i + d_i d_j \mathbf{p}_j \frac{1}{r_{ij}} \cdot \mathbf{p}_j d_j d_i \right), \tag{2.35}$$

$$X_{ij}^{\mathrm{SD2}} = i \left(M_i d_j \frac{1}{r_{ij}} d_j M_i + d_i d_j \mathbf{p}_i \frac{1}{r_{ij}} \cdot \mathbf{p}_i d_j d_i \right), \tag{2.36}$$

and

$$X_{ij}^{\mathrm{SD3}} = -d_i d_j \frac{1}{r_{ij}} d_j d_i \,, \tag{2.37}$$

using the generalized notation presented in Sec. 2.2. Here, the kinematic factors are defined by

$$M_i = K_i \left(1 + b_i p_i Y_i\right) \frac{1}{\sqrt{1 + Y_i^\dagger Y_i}} \tag{2.38}$$

and

$$d_i = K_i \left(\alpha b_i - p_i^{-1} Y_i\right) \frac{1}{\sqrt{1 + Y_i^\dagger Y_i}} \,. \tag{2.39}$$

The combination of the one-electron IODKH operator [Eqs. (2.24) and (2.25)] and the transformed two-electron operator [Eqs. (2.34)–(2.37)] are termed the IODKH/IODKH Hamiltonian.

Additionally, the less accurate but simpler treatment is the combination of the one-electron IODKH operator [Eqs. (2.24) and (2.25)] and the untransformed two-electron NR Coulomb operator,

$$g_{ij}^{\mathrm{SF}} = \frac{1}{r_{ij}} \mathbf{I}_2 \tag{2.40}$$

and

$$X_{12}^{\mathrm{SD1}} = X_{12}^{\mathrm{SD2}} = X_{12}^{\mathrm{SD3}} = 0 \,. \tag{2.41}$$

In the present thesis, this type of Hamiltonian is termed IODKH/NR.

2.5 LUT method

The computational bottlenecks of the IODKH and IODKH/IODKH methods are the multiplication of the unitary transformation matrices to decouple the electronic and positronic Hamiltonians. In this section, the LUT method [31,32], which reduces the cost

of the unitary transformation, is briefly explained.

The concept of the LUT method is based on the locality of the relativistic effect. Namely, the unitary transformation for the entire system U is approximated by the direct sum of the unitary transformations U^A defined for the local disjoint subsystems $\{A\}$,

$$U \approx \bigoplus_A U^A . \tag{2.42}$$

Normally, the atomic partitioning is adopted for the subsystem construction, although the arbitrary partitioning is available in principle. The relativistic effects in the one-electron kinetic energy, one-electron potential energy, and two-electron interaction terms are dominant in the atomic (one-center) contributions. Additionally, the relativistic effect in the one-electron potential energy term is also dominant in the inter-atomic (two-center) contributions within a small distance τ. Consequently, the LUT-based, IODKH-transformed one- and two-electron terms are given by

$$\left\langle \mu^A \middle| h_i^{\mathrm{IODKH}} \middle| \nu^B \right\rangle \approx \begin{cases} \left\langle \mu^A \middle| T^{\mathrm{IODKH}} + \sum_{C \notin A} V_C^{\mathrm{NR}} + \sum_{C \in A} V_C^{\mathrm{IODKH}} \middle| \nu^B \right\rangle & (A = B) \\ \left\langle \mu^A \middle| T^{\mathrm{NR}} + \sum_{C \notin A} V_C^{\mathrm{NR}} + \sum_{C \in A,B} V_C^{\mathrm{IODKH}} \middle| \nu^B \right\rangle & (A \neq B,\ R_{AB} \leq \tau) \\ \left\langle \mu^A \middle| T^{\mathrm{NR}} + \sum_{C} V_C^{\mathrm{NR}} \middle| \nu^B \right\rangle & (A \neq B,\ R_{AB} > \tau) \end{cases} \tag{2.43}$$

and

$$\left\langle \mu^A \nu^B \middle| g_{ij}^{\mathrm{IODKH}} \middle| \rho^C \lambda^D \right\rangle \approx \begin{cases} \left\langle \mu^A \nu^B \middle| g_{ij}^{\mathrm{IODKH}} \middle| \rho^C \lambda^D \right\rangle & (A = B = C = D) \\ \left\langle \mu^A \nu^B \middle| g_{ij}^{\mathrm{NR}} \middle| \rho^C \lambda^D \right\rangle & (\text{otherwise}) \end{cases}, \tag{2.44}$$

respectively. Here, the so-called physicists' notation is used,

$$\left\langle \mu \middle| X_i \middle| \nu \right\rangle = \int \mathrm{d}\mathbf{r}_i \chi_\mu^*(i) X_i \chi_\nu(i) \tag{2.45}$$

and

$$\left\langle \mu\nu \left| X_{ij} \right| \rho\lambda \right\rangle = \int \mathrm{d}\mathbf{r}_i \mathrm{d}\mathbf{r}_j \chi_\mu^*(i)\, \chi_\mu^*(j)\, X_{ij} \chi_\rho(i)\, \chi_\lambda(j), \tag{2.46}$$

where $\{\chi_\mu\}$ denotes the AOs, X the arbitrary one- or two-electron operators, and $\mathbf{r}$ the spatial coordinates. R_{AB} is the distance between atoms A and B. T^{IODKH} and V_C^{IODKH} are the V-free and V-dependent parts of the IODKH-transformed one-electron term [Eqs. (2.24) and (2.25)] with the substitution of V with the atomic contribution V_C. g_{ij}^{IODKH} is the IODKH-transformed two-electron term [Eqs. (2.34)–(2.37)]. T^{NR}, V_C^{NR}, and g_{ij}^{NR} are the standard NR kinetic energy, potential energy, and electron repulsion terms,

$$T^{\mathrm{NR}} = \frac{1}{2} p^2 \mathbf{I}_2, \tag{2.47}$$

$$V_C^{\mathrm{NR}} = V_C \mathbf{I}_2, \tag{2.48}$$

and

$$g_{ij}^{\mathrm{NR}} = \frac{1}{r_{ij}} \mathbf{I}_2. \tag{2.49}$$

By applying the LUT method, the computational costs of the IODKH and IODKH/IODKH methods are reduced from $O(N^3)$ to $O(Mn^3)$ and from $O(N^5)$ to $O(Mn^5)$, respectively. Here, N denotes the basis set dimension in the entire system, M the number of atoms in the entire system, and $n < N$ the basis set dimension in the atomic subsystems. In particular, for sufficiently large-scale systems, i.e., $n^3 < n^5 \ll M$, the LUT method enables the linear-scaling computation of the IODKH and IODKH/IODKH procedures.

2.6 GHF method

In the GHF method [33-42], the total electronic wavefunction for an *N*-electron system is expressed by a single Slater determinant,

$$\Psi^{\mathrm{GHF}}\left(\mathbf{x}_1,\mathbf{x}_2,\cdots,\mathbf{x}_N\right)=\left\|\varphi_1\left(\mathbf{x}_1\right)\varphi_2\left(\mathbf{x}_2\right)\cdots\varphi_N\left(\mathbf{x}_N\right)\right\|, \tag{2.50}$$

where φ is the GSOs. The GSO is represented by a linear combination of alpha- and beta-spin components,

$$\varphi_i\left(\mathbf{x}_i\right)=\varphi_i^{\alpha}\left(\mathbf{x}_i\right)+\varphi_i^{\beta}\left(\mathbf{x}_i\right)=\psi_i^{\alpha}\left(\mathbf{r}_i\right)\alpha\left(\omega_i\right)+\psi_i^{\beta}\left(\mathbf{r}_i\right)\beta\left(\omega_i\right) \tag{2.51}$$

with

$$\psi_i^{\alpha}\left(\mathbf{r}_i\right)=\sum_{\mu=1}^{K^{\alpha}}C_{\mu i}^{\alpha}\chi_{\mu}^{\alpha}\left(\mathbf{r}_i\right) \tag{2.52}$$

and

$$\psi_i^{\beta}\left(\mathbf{r}_i\right)=\sum_{\mu=1}^{K^{\beta}}C_{\mu i}^{\beta}\chi_{\mu}^{\beta}\left(\mathbf{r}_i\right). \tag{2.53}$$

Here, χ is the AOs, C is the MO coefficients, and K is the number of the AOs. The variable $\mathbf{x}$ contains the spatial coordinate $\mathbf{r}$ and the spin coordinate ω. Hereafter, these arguments are omitted for simplicity. In addition, the same $\left\{\chi^{\alpha}\right\}$ and $\left\{\chi^{\beta}\right\}$ sets are adopted in this thesis.

The two-component RH equation, i.e., a working equation of GHF, is given in block form,

$$\begin{pmatrix}\mathbf{F}^{\alpha\alpha} & \mathbf{F}^{\alpha\beta}\\ \mathbf{F}^{\beta\alpha} & \mathbf{F}^{\beta\beta}\end{pmatrix}\begin{pmatrix}\mathbf{C}^{\alpha}\\ \mathbf{C}^{\beta}\end{pmatrix}=\begin{pmatrix}\mathbf{S}^{\alpha\alpha} & \mathbf{0}\\ \mathbf{0} & \mathbf{S}^{\beta\beta}\end{pmatrix}\begin{pmatrix}\mathbf{C}^{\alpha}\\ \mathbf{C}^{\beta}\end{pmatrix}\boldsymbol{\varepsilon}, \tag{2.54}$$

where $\mathbf{F}$ denotes the Fock matrix, $\mathbf{S}$ the overlap matrix, and $\boldsymbol{\varepsilon}$ the orbital energies. The Fock and overlap matrix elements are defined as

$$F_{\mu\nu}^{\omega\omega'} = \left\langle \mu\omega \middle| h_i \middle| \nu\omega' \right\rangle + \sum_{\rho\lambda} \sum_{\tau\tau'}^{\{\alpha,\beta\}} D_{\rho\lambda}^{\tau\tau'} \left[\left\langle \mu\omega\, \rho\tau \middle| g_{ij} \middle| \nu\omega'\, \lambda\tau' \right\rangle - \left\langle \mu\omega\, \rho\tau \middle| g_{ij} \middle| \lambda\tau'\, \nu\omega' \right\rangle \right] \tag{2.55}$$

and

$$S_{\mu\nu}^{\omega\omega'} = \left\langle \mu \middle| \nu \right\rangle \delta_{\omega\omega'}, \tag{2.56}$$

respectively. Here, $\delta_{\omega\omega'}$ is the Kronecker delta,

$$\delta_{\omega\omega'} = \begin{cases} 1 & (\omega = \omega') \\ 0 & (\omega \neq \omega') \end{cases}. \tag{2.57}$$

The density matrix of GHF is also expressed in block form,

$$\mathbf{D} = \begin{pmatrix} \mathbf{D}^{\alpha\alpha} & \mathbf{D}^{\alpha\beta} \\ \mathbf{D}^{\beta\alpha} & \mathbf{D}^{\beta\beta} \end{pmatrix} = \begin{pmatrix} \mathbf{C}^{\alpha} \\ \mathbf{C}^{\beta} \end{pmatrix} \mathbf{f} \begin{pmatrix} \mathbf{C}^{\alpha} \\ \mathbf{C}^{\beta} \end{pmatrix}^{\dagger}, \tag{2.58}$$

where $\mathbf{f}$ is the occupation number vector. The total energy expression is given by

$$E^{\mathrm{GHF}} = \frac{1}{2} \mathrm{tr}\left[\mathbf{D} \left(\mathbf{h} + \mathbf{F} \right) \right], \tag{2.59}$$

where $\mathbf{h}$ is the one-electron part of the Fock matrix.

2.7 Time-reversal symmetry and KRHF method

Because the Hamiltonian of a closed-shell system satisfies time-reversal symmetry, the equations of KRHF [43-46] are derived by imposing the time-reversal invariance on GHF. When an arbitrary Hermitian one-electron operator Ω satisfies time-reversal symmetry, i.e., Ω is commutable with the time-reversal operator K,

$$\left[\Omega, K \right] = \Omega K - K\Omega = 0, \tag{2.60}$$

$$K = -i\sigma_y K_0, \tag{2.61}$$

where σ_y is the *y*-component of the Pauli matrices and K_0 is the complex conjugation

operator, the matrix representation of Ω has the following structure,

$$\begin{aligned}\mathbf{\Omega} &= \begin{pmatrix} \mathbf{\Omega}^{\alpha\alpha} & \mathbf{\Omega}^{\alpha\beta} \\ \mathbf{\Omega}^{\beta\alpha} & \mathbf{\Omega}^{\beta\beta} \end{pmatrix} \\ &= \begin{pmatrix} \mathbf{\Omega}^{\alpha\alpha} & \mathbf{\Omega}^{\alpha\beta} \\ -\mathbf{\Omega}^{\alpha\beta *} & \mathbf{\Omega}^{\alpha\alpha *} \end{pmatrix} \\ &= \begin{pmatrix} \Re\mathbf{\Omega}^{\alpha\alpha} + i\Im\mathbf{\Omega}^{\alpha\alpha} & \Re\mathbf{\Omega}^{\alpha\beta} + i\Im\mathbf{\Omega}^{\alpha\beta} \\ -\Re\mathbf{\Omega}^{\alpha\beta} + i\Im\mathbf{\Omega}^{\alpha\beta} & \Re\mathbf{\Omega}^{\alpha\alpha} - i\Im\mathbf{\Omega}^{\alpha\alpha} \end{pmatrix}. \end{aligned} \tag{2.62}$$

Here, $\mathbf{\Omega}^{\alpha\alpha}$ and $\mathbf{\Omega}^{\alpha\beta}$ are Hermitian and skew-symmetric matrices, respectively; the asterisk (*) denotes the complex conjugate. The matrix can be expanded using the Pauli matrices,

$$\mathbf{\Omega} = \mathbf{I}_2 \otimes \Re\mathbf{\Omega}^{\alpha\alpha} + \left(i\sigma_z\right) \otimes \Im\mathbf{\Omega}^{\alpha\alpha} + \left(i\sigma_y\right) \otimes \Re\mathbf{\Omega}^{\alpha\beta} + \left(i\sigma_x\right) \otimes \Im\mathbf{\Omega}^{\alpha\beta}, \tag{2.63}$$

where $\mathbf{I}_2$ denotes the 2×2 identity matrix and $\boldsymbol{\sigma}$ the Pauli matrices in their standard representation [Eqs. (2.4)–(2.7)]. The algebra of the products of the imaginary unit and the Pauli matrices is known to be identical to that of the quaternion units $\breve{i}$, $\breve{j}$, and $\breve{k}$ [54], i.e.,

$$\breve{i} \leftrightarrow i\sigma_z, \quad \breve{j} \leftrightarrow i\sigma_y, \quad \breve{k} \leftrightarrow i\sigma_x. \tag{2.64}$$

Therefore, there is an isomorphic connection between the matrix representation under time-reversal symmetry and quaternions,

$$\mathbf{\Omega} = \begin{pmatrix} \mathbf{\Omega}^{\alpha\alpha} & \mathbf{\Omega}^{\alpha\beta} \\ -\mathbf{\Omega}^{\alpha\beta *} & \mathbf{\Omega}^{\alpha\alpha *} \end{pmatrix} \leftrightarrow {}^{\mathrm{Q}}\mathbf{\Omega} = \Re\mathbf{\Omega}^{\alpha\alpha} + \breve{i}\,\Im\mathbf{\Omega}^{\alpha\alpha} + \breve{j}\Re\mathbf{\Omega}^{\alpha\beta} + \breve{k}\Im\mathbf{\Omega}^{\alpha\beta}. \tag{2.65}$$

Here, the pre-superscript Q indicates being a quaternion matrix. The relationship between time-reversal symmetry and quaternion algebra is described in detail in Ref. [55].

Because the Fock matrix of KRHF can be represented by the same structure as Eq. (2.65), the RH equation for KRHF in complex form is written as

$$\begin{pmatrix} \mathbf{F}^{\alpha\alpha} & \mathbf{F}^{\alpha\beta} \\ -\mathbf{F}^{\alpha\beta *} & \mathbf{F}^{\alpha\alpha *} \end{pmatrix} \begin{pmatrix} \mathbf{C}^{\alpha} \\ \mathbf{C}^{\beta} \end{pmatrix} = \begin{pmatrix} \mathbf{S}^{\alpha\alpha} & \mathbf{0} \\ \mathbf{0} & \mathbf{S}^{\alpha\alpha} \end{pmatrix} \begin{pmatrix} \mathbf{C}^{\alpha} \\ \mathbf{C}^{\beta} \end{pmatrix} \boldsymbol{\varepsilon} . \tag{2.66}$$

By performing a quaternion unitary transformation,

$$\mathbf{U} = \frac{1}{\sqrt{2}} \begin{pmatrix} 1 & \breve{j} \\ \breve{j} & 1 \end{pmatrix}, \tag{2.67}$$

the Fock matrix in KRHF can be block-diagonalized to

$$\mathbf{U}^{\dagger} \begin{pmatrix} \mathbf{F}^{\alpha\alpha} & \mathbf{F}^{\alpha\beta} \\ -\mathbf{F}^{\alpha\beta *} & \mathbf{F}^{\alpha\alpha *} \end{pmatrix} \mathbf{U} = \begin{pmatrix} \mathbf{F}^{\alpha\alpha} + \breve{j}\mathbf{F}^{\alpha\beta} & \mathbf{0} \\ \mathbf{0} & -\breve{k}\left(\mathbf{F}^{\alpha\alpha} + \breve{j}\mathbf{F}^{\alpha\beta}\right)\breve{k} \end{pmatrix}. \tag{2.68}$$

The corresponding transformation of the eigenvectors is

$$\mathbf{U}^{\dagger} \begin{pmatrix} \mathbf{C}^{\alpha} \\ \mathbf{C}^{\beta} \end{pmatrix} = \begin{pmatrix} \mathbf{C}^{\alpha} - \breve{j}\mathbf{C}^{\beta *} \\ \mathbf{C}^{\beta} - \breve{j}\mathbf{C}^{\alpha *} \end{pmatrix}. \tag{2.69}$$

Each block of Eq. (2.68) leads to two equivalent eigenvalue problems whose eigenvalues are common, and the eigenvectors are related by the time-reversal operation. The eigenvalue problem is therefore doubly degenerated in KRHF. The pair of doubly degenerated eigenvectors is called a Kramers pair. Thus, it suffices to consider the upper-diagonal block of Eq. (2.68), and the complex eigenvalue problem can be reduced to a quaternion problem of half the dimension,

$${}^{\mathrm{Q}}\mathbf{F}\,{}^{\mathrm{Q}}\mathbf{C} = {}^{\mathrm{Q}}\mathbf{S}\,{}^{\mathrm{Q}}\mathbf{C}\boldsymbol{\varepsilon} \Leftrightarrow \left(\mathbf{F}^{\alpha\alpha} + \breve{j}\mathbf{F}^{\alpha\beta}\right)\left(\mathbf{C}^{\alpha} - \breve{j}\mathbf{C}^{\beta *}\right) = \mathbf{S}^{\alpha\alpha}\left(\mathbf{C}^{\alpha} - \breve{j}\mathbf{C}^{\beta *}\right)\boldsymbol{\varepsilon} . \tag{2.70}$$

This idea is an analogous to a numerical method where an $n \times n$ complex Hermitian eigenvalue problem can be replaced by a $2n \times 2n$ real symmetric one [56].

From Eq. (2.69), the spin-orbitals of KRHF are expressed as

$${}^{\mathrm{Q}}\varphi_i = \varphi_i^{\alpha} - \breve{j}\varphi_i^{\beta *} . \tag{2.71}$$

On the basis of $\left\{{}^{\mathrm{Q}}\varphi_i\right\}$, the total electronic wavefunction of KRHF is defined as

$$\Psi^{\mathrm{KRHF}} = \left\| {}^{\mathrm{Q}}\varphi_1 \, {}^{\mathrm{Q}}\varphi_2 \cdots {}^{\mathrm{Q}}\varphi_{N/2} \right\|. \tag{2.72}$$

Finally, the total electronic energy is given by

$$E^{\mathrm{KRHF}} = \frac{1}{2}\mathrm{tr}\left[{}^{\mathrm{Q}}\mathbf{D}\left({}^{\mathrm{Q}}\mathbf{h} + {}^{\mathrm{Q}}\mathbf{F} \right) \right]. \tag{2.73}$$

2.8 Large-scale higher-order electron correlation method with SF relativistic Hamiltonian

2.8.1 Introduction

The CI, MPPT, and CC methods are robust theoretical approaches that systematically improve the total energy and the wavefunction of atoms and molecules with increasing order of electron excitations included. Based on these correlated methods, the energetics of many molecules can be predicted with chemical accuracy by considering the contribution of triple or quadruple excitations. One of the examples is the CCSD(T) method [57], which has been widely used in practical applications and benchmark studies through the years [58]. The success of the CCSD(T) model has inspired further development of similar methodologies [59-73]. Despite their reliability, the correlation methods have two severe drawbacks manifesting at high excitation orders.

The first drawback is the immense complexity in the derivation and subsequent implementation of the working equations of the higher-order methods. For example, the total numbers of terms included in the working equations of the CCSD, CCSDT, and CCSDTQ methods are 48, 102, and 183, respectively [74]. The development of general-purpose codes is in fact a major bottleneck in routinely performing calculations based on these methods. The pioneering implementation of the higher-order CC methods was reported by Kállay and Surján [75] using a string-based algorithm, i.e., in a single

algorithmic framework, and by Hirata et al. [76-82] using TCE, which is a computerized symbolic algebra system. TCE permits automatic derivation and implementation of the majority of standard electron correlation methods, i.e., CI, MPPT, CC, and any combination thereof, at an arbitrary order.

The second drawback of the higher-order correlation methods is their tremendous computational cost with respect to the system size n. For example, the computational costs of CCSD, CCSDT, and CCSDTQ are asymptotically $O(n^6)$, $O(n^8)$, and $O(n^{10})$, respectively. A wide variety of fragmentation-based low-scaling techniques have been reported for the electron correlation methods. In such an approach, the system under consideration is divided into several fragments; the electronic energy and properties of the entire system are then obtained by merging the results of these fragment calculations. This approach includes the cluster-in-molecule scheme [83-85], the fragment molecular orbital scheme [86], the incremental scheme [87-89], and the divide-expand-consolidate scheme [90]. The D&C scheme is also one of the fragmentation-based linear-scaling approaches, which was originally developed for the efficient HF and DFT calculations [47,91-94]. Kobayashi and co-workers have reported the development of the D&C-based linear-scaling electron correlation methods at the MP2 [95,96], CCSD [97], CCSD(T) [98], and symmetry adapted cluster [99] levels in the NR framework. Recently, the D&C method was applied to the one-component or SF relativistic electron correlation calculations up to the CCSD(T) level, together with the LUT scheme, i.e., an efficient construction technique for the relativistic Hamiltonian [100]. At this moment, however, the highest excitation level to which a linear-scaling computation is applied is the triples regardless of which specific linear-scaling technique is invoked. A higher-order, linear-scaling electron correlation method is, therefore, desired for a more accurate description

of electronic structures of large-scale systems.

In this section, higher-order CC methods up to connected quadruple excitation and MPPT methods up to fourth order as well as their combinations compatible with the NR and SF relativistic calculations have been implemented by means of TCE, and extended to the linear-scaling D&C method. This section is organized as follows: Section 2.8.2 explains the theory and implementation, where the general D&C-based formulae of the standard CC and MPPT methods are first described and the energy expression of the D&C-based CC methods augmented with the perturbation correction is then presented. Section 2.8.3 presents the numerical assessments of the conventional (D&C-free) and D&C-based correlation methods. Finally, concluding remarks are given in Sec. 2.8.4.

2.8.2 Theory and implementation

2.8.2.1 D&C-based higher-order CC and MPPT methods

This subsection presents the generic D&C-based formulation of the standard CC and MPPT methods at an arbitrary order. In the D&C method, the system under consideration is spatially divided into disjoint subsystems. A set of AOs in a subsystem s is represented by $\mathcal{S}(s)$, where

$$\mathcal{S}(s) \bigcap \mathcal{S}(s') = \varnothing \quad (\forall s \neq s'). \tag{2.74}$$

The union of $\mathcal{S}(s)$ is represented by

$$\mathcal{T} = \bigcup_{s} \mathcal{S}(s), \tag{2.75}$$

which corresponds to a set of AOs in the entire system. To improve the description of the subsystem, a neighboring region referred to as a buffer region is considered in the construction of the subsystem MOs. A set of AOs in the buffer region of s, as denoted

by $\mathcal{B}(s)$, is added to $\mathcal{S}(s)$ in order to construct a set of AOs in the localization region expressed as

$$\mathcal{L}(s) = \mathcal{S}(s) \bigcup \mathcal{B}(s). \tag{2.76}$$

The D&C-based correlation energy is estimated by summing up the correlation energies corresponding to the individual subsystems and is as follows:

$$E_{\mathrm{corr}}^{\mathrm{DC}} = \sum_{s} E_{\mathrm{corr}}^{(s)}. \tag{2.77}$$

The correlation energy $E_{\mathrm{corr}}^{(s)}\left[\mathcal{L}(s)\right]$ of the localization region s can be straightforwardly evaluated from the so-called energy equation defined for s,

$$E_{\mathrm{corr}}^{(s)}\left[\mathcal{L}(s)\right] = \left\langle \Phi_0^{(s)} \middle| \bar{H}_{\mathrm{N}} \middle| \Phi_0^{(s)} \right\rangle, \tag{2.78}$$

where $\left|\Phi_0^{(s)}\right\rangle$ represents the reference wavefunction in each subsystem (localization region) obtained from the (D&C-)HF calculations, and $\bar{H}_{\mathrm{N}}$ is the normal-ordered effective Hamiltonian. However, the sum of the correlation energies over all the localization regions will provide an inappropriate estimate of the correlation energy for the entire system, viz.,

$$E_{\mathrm{corr}}^{(s)} \neq E_{\mathrm{corr}}^{(s)}\left[\mathcal{L}(s)\right], \tag{2.79}$$

because the localization regions overlap with each other owing to the existence of the buffer region. Therefore, the contribution of the correlation energy corresponding to the pure subsystem must be extracted. This is accomplished by using the concept of EDA, which was proposed by Nakai [101]. The EDA technique partitions the energy into atomic contributions in an analogous manner to the Mulliken population analysis. By applying the EDA technique to Nesbet's correlation energy representation [102] and leaving the last quarter integral transformation undone, the correlation energy can be re-written as the

sum of the pure contributions of each subsystem,

$$E_{\mathrm{corr}}^{(s)} = \frac{1}{4} \sum_{p_1,p_2}^{\{\mathrm{particle}\}} \sum_{h_1,h_2}^{\{\mathrm{hole}\}} \sum_{\mu \in \mathcal{S}(s)} C_{\mu h_1}^{(s)*} \left\langle \mu h_2^{(s)} \middle\| p_1^{(s)} p_2^{(s)} \right\rangle \left(T_{h_1 h_2, p_1 p_2}^{(s)} + T_{h_1,p_1}^{(s)} T_{h_2,p_2}^{(s)} - T_{h_1,p_2}^{(s)} T_{h_2,p_1}^{(s)} \right), \quad (2.80)$$

where $C_{\mu h}^{(s)}$ is the subsystem MO coefficients, $T_{h_1 \cdots p_1 \cdots}^{(s)}$ is the subsystem excitation amplitudes, μ refers to the AOs belonging to $\mathcal{S}(s)$, and $h^{(s)}$ and $p^{(s)}$ refer to the particle and hole orbitals of the subsystem s, respectively. Note that the correlation energies of the arbitrary-order CC and MPPT methods are expressed as Eq. (2.80) with the substitution of corresponding amplitudes. The subsystem amplitudes are obtained by solving the so-called amplitude equations straightforwardly defined for each subsystem as

$$\left\langle \Omega_m^{(s)} \middle| \bar{H}_N \middle| \Phi_0^{(s)} \right\rangle = 0 , \quad (2.81)$$

where $\left| \Omega_m^{(s)} \right\rangle$ is the m-tuply excited determinant manifold relative to $\left| \Phi_0^{(s)} \right\rangle$ in the subsystem s.

2.8.2.2 D&C-based CC methods augmented with perturbation correction

The energy contribution of the higher-order electron correlation can be simply evaluated through the RS perturbation theory [103,104]. In this context, the zeroth-order energy is the correlation energy of the parent CC method. The first-order RS correction vanishes by assuming the canonical HF reference. The second-order RS corrections to the CCSD energy have the following generic form:

$$E_{\mathrm{X}} = \sum_{p_1<p_2<\cdots}^{\{\mathrm{particle}\}} \sum_{h_1<h_2<\cdots}^{\{\mathrm{hole}\}} \frac{A_{h_1 h_2 \cdots p_1 p_2 \cdots} B_{h_1 h_2 \cdots p_1 p_2 \cdots}}{D_{h_1 h_2 \cdots p_1 p_2 \cdots}} , \quad (2.82)$$

where $A_{h_1h_2\cdots p_1p_2\cdots}$ and $B_{h_1h_2\cdots p_1p_2\cdots}$ are the tensors that are composed of the excitation amplitudes, the de-excitation coefficients, and the two-electron integrals, and $D_{h_1h_2\cdots p_1p_2\cdots}$ is the energy denominator. For the second-order triple substitution correction [$\mathrm{X} = (2)_{\mathrm{T}}$], $A_{h_1h_2\cdots p_1p_2\cdots}$ and $B_{h_1h_2\cdots p_1p_2\cdots}$ are six-index tensors given by

$$A_{h_1h_2h_3p_1p_2p_3} = \left\langle \Phi_0 \middle| \left(1 + \hat{\Lambda}_1 + \hat{\Lambda}_2\right) \bar{H}_N \middle| \Phi_{h_1h_2h_3p_1p_2p_3} \right\rangle \tag{2.83}$$

and

$$B_{h_1h_2h_3p_1p_2p_3} = \left\langle \Phi_{h_1h_2h_3p_1p_2p_3} \middle| \bar{H}_N \middle| \Phi_0 \right\rangle, \tag{2.84}$$

respectively. The energy denominator is

$$D_{h_1h_2h_3p_1p_2p_3} = \varepsilon_{h_1} + \varepsilon_{h_2} + \varepsilon_{h_3} - \varepsilon_{p_1} - \varepsilon_{p_2} - \varepsilon_{p_3}. \tag{2.85}$$

Here, $\hat{\Lambda}_m$ denotes the *m*-body de-excitation operators and ε denotes the orbital energies. For the quadruple substitution correction [$\mathrm{X} = (2)_{\mathrm{Q}}$], the tensors and energy denominator possess eight indices, as shown below:

$$A_{h_1h_2h_3h_4p_1p_2p_3p_4} = \left\langle \Phi_0 \middle| \left(1 + \hat{\Lambda}_1 + \hat{\Lambda}_2\right) \bar{H}_N \middle| \Phi_{h_1h_2h_3h_4p_1p_2p_3p_4} \right\rangle, \tag{2.86}$$

$$B_{h_1h_2h_3h_4p_1p_2p_3p_4} = \left\langle \Phi_{h_1h_2h_3h_4p_1p_2p_3p_4} \middle| \bar{H}_N \middle| \Phi_0 \right\rangle, \tag{2.87}$$

and

$$D_{h_1h_2h_3h_4p_1p_2p_3p_4} = \varepsilon_{h_1} + \varepsilon_{h_2} + \varepsilon_{h_3} + \varepsilon_{h_4} - \varepsilon_{p_1} - \varepsilon_{p_2} - \varepsilon_{p_3} - \varepsilon_{p_4}. \tag{2.88}$$

The de-excitation coefficients (Λ_1 and Λ_2), which are included in $A_{h_1h_2\cdots p_1p_2\cdots}$, are evaluated by solving the so-called Λ equation,

$$\left\langle \Phi_0 \middle| \left(1 + \hat{\Lambda}_1 + \hat{\Lambda}_2\right) \bar{H}_N \middle| \Omega_m \right\rangle = 0. \tag{2.89}$$

The CCSD method corrected by the terms with $\mathrm{X} = (2)_\mathrm{T}$ and $(2)_\mathrm{Q}$ is referred to as the CCSD(2)$_\mathrm{TQ}$ method [79]. Furthermore, by substituting $\hat{\Lambda}_1 \approx \hat{T}_1^\dagger$ and $\hat{\Lambda}_2 \approx \hat{T}_2^\dagger$ into Eq. (2.83) and retaining only the binary tensor contractions, the formula for the so-called (T) correction, i.e., the perturbative triples correction, is obtained.

To extend these perturbative treatments to the D&C method, the pure subsystem contribution of the correlation energy must be extracted from Eq. (2.82), as described in the previous subsection. However, this approach cannot be directly applied to these perturbative treatments because Eq. (2.82) does not follow Nesbet's energy expression [Eq. (2.80)], as explained for CCSD(T) in a previous study [98]. In the long algebraic expressions of the $(2)_\mathrm{T}$ and $(2)_\mathrm{Q}$ [and also (T)] corrections given in Ref. [105], all the terms of $B_{h_1h_2\cdots p_1p_2\cdots}$ consist of the sum of the tensor products that are generalized as

$$b \sum_{\{t,u,v,w\}} \left(\prod T_{h_1\cdots p_1\cdots} \right) \langle tu | vw \rangle . \tag{2.90}$$

Here, b is the scalar coefficient, $\prod T_{h_1\cdots p_1\cdots}$ is the general form of the product among the single and double excitation amplitudes, *t*, *u*, *v*, and *w* refer to the arbitrary spin-orbitals, and the summation runs over any combination of $\{t,u,v,w\}$. Thus, the perturbation correction for the subsystem s is formulated as follows:

$$E_\mathrm{X}^{(s)} = \sum_{p_1<p_2<\cdots}^{\{\mathrm{particle}\}} \sum_{h_1<h_2<\cdots}^{\{\mathrm{hole}\}} \frac{A_{h_1h_2\cdots p_1p_2\cdots}^{(s)} B_{h_1h_2\cdots p_1p_2\cdots}^{(s)}}{D_{h_1h_2\cdots p_1p_2\cdots}^{(s)}}, \tag{2.91}$$

where $A_{h_1h_2\cdots p_1p_2\cdots}^{(s)}$, $B_{h_1h_2\cdots p_1p_2\cdots}^{(s)}$, and $D_{h_1h_2\cdots p_1p_2\cdots}^{(s)}$ are constructed from the matrix elements of each subsystem. In particular, $B_{h_1h_2\cdots p_1p_2\cdots}^{(s)}$ is defined as

$$B^{(s)}_{h_1h_2\cdots p_1p_2\cdots} = \sum_i b_i^{(s)} \left[\sum_{\{t,u,v,w\}} \left(\prod T^{(s)}_{h_1\cdots p_1\cdots} \right) \sum_{\mu\in\mathcal{S}(s)} C^{(s)*}_{\mu t} \left\langle \mu u^{(s)} \middle| v^{(s)} w^{(s)} \right\rangle \right]_i \tag{2.92}$$

through the EDA partitioning, that is, by leaving the last quarter integral transformation undone. Here, i refers to the term number in the derived algebraic expression of the $(2)_T$, $(2)_Q$, and (T) corrections. It should be noted that there is arbitrariness in Eq. (2.92) associated with the choice of the untransformed spin-orbital from $\{t,u,v,w\}$. The previous study on the D&C-based CCSD(T) method [98] revealed that any choices lead to the comparable correlation energies. Thus, the present implementation adopts the fixed expression of Eq. (2.92), where the one-index transformation for the spin-orbital t (the first index of the two-electron integral) is left undone, for all the correction terms. Besides, the de-excitation coefficients included in $A^{(s)}_{h_1h_2\cdots p_1p_2\cdots}$ are obtained by solving the Λ equation straightforwardly defined for each subsystem as

$$\left\langle \Phi_0^{(s)} \middle| \left(1 + \hat{\Lambda}_1 + \hat{\Lambda}_2\right) \bar{H}_N \middle| \Omega_m^{(s)} \right\rangle = 0 . \tag{2.93}$$

2.8.2.3 Implementation

In the present subsection, the D&C-free/D&C-based MP2, MP3, MP4, CCSD, CCSDT, CCSDTQ, CCSD(T), and $CCSD(2)_{TQ}$ methods were implemented through the symbolic algebra system TCE. For the various orders of the CC and MPPT methods, TCE automates the derivation and implementation of programmable expressions of the energy equation [Eq. (2.80)], the amplitude equation [Eq. (2.81)], the Λ equation [Eq. (2.93)], and the perturbation correction [Eq. (2.91)], as well as the required tensor components in these expressions. The general capabilities and inner workings of TCE have been reported elsewhere [77-79]. The driver codes as well as the integral transformation were manually

written in order to interface with the in-house program suite, which is compatible with both the NR and relativistic Hamiltonians. The one-component or SF relativistic all-electron correlated calculations can be performed by replacing the NR reference wavefunction, i.e., the NR orbital energies (more generally, the Fock matrix elements) and the MO coefficients with the relativistic ones.

The overview of the present implementation is explained as follows. Figure 2.1(a) shows the pseudocode of a manually written driver subroutine of the D&C-based CC and MPPT methods. The outermost loop (line 2) runs over the subsystems that are set up in line 1. For each subsystem, the correlation energy and the excitation amplitudes, $T^{(s)}$, are determined by solving the non-linear amplitude equations in an iterative manner (lines 3–8). It should be noted that this loop for solving the amplitude equations is employed in both the CC and MPPT calculations. However, in the widely used implementation of MPPT for the canonical HF reference, where the Fock matrix is assumed to be diagonal, the correlation energy is directly obtained through a single analytical formula rather than through the iterative evaluation of the amplitudes. In the present implementation, not the diagonal but the entire Fock matrix is used to construct the zeroth-order Hamiltonian. Thus, the present MPPT codes are more general and robust, that is, they are compatible with non-canonical or non-orthogonal reference orbitals. In case of the CC calculations augmented with the RS perturbation theory, a series of the Λ equations is iteratively solved to determine the de-excitation coefficients (lines 10–14). The perturbative energy correction is subsequently evaluated (line 15). At the end of each subsystem calculation, all the excitation amplitudes, de-excitation coefficients, and other intermediates required for the calculations are deleted, and the memory allocated for them is released (lines 16 and 18). This is because the energy, amplitude, and Λ equations are defined for each of

the subsystems. The individual tensor components required in lines 5, 6, 12, and 15 are evaluated through a number of TCE-synthesized subroutines for a unary tensor substitution or a binary tensor contraction.

A general form of the TCE-synthesized subroutines, which provide a tensor $Z^{(s)}$ by contracting two seed tensors $X^{(s)}$ and $Y^{(s)}$ for the subsystem s, is shown in Figure 2.1(b). Here, the so-called tiling algorithm was adopted, as reported in previous studies [77-79]. Thus, the nested outer loops run over the hole and particle tiles (line 1). Here, a tile is a small segment of tensors possessing the same spin symmetry. In the tiling algorithm, all the operations for tensors such as loading, saving, sorting, addition, and multiplication are performed in a tile-wise fashion rather than in an element-wise fashion for efficiency purposes. In the loops of line 1, the canonical relationship (index permutation symmetry) is also considered at the tile level to restrict the loop range. In line 2, the spin symmetry is taken into account, that is, the tensor elements that are symmetrically zero are excluded from arithmetic. For the non-zero cases, the tiles of the seed tensors, $X^{(s)}$ and $Y^{(s)}$, are loaded from the storage (lines 3 and 5). In lines 4 and 6, the tiles are subsequently sorted so that they lead to a unit stride in the following tensor contraction (matrix multiplication) in line 8. In line 7, a factor multiplied in the tensor contraction is determined from the index permutation symmetry. This factor also includes the energy denominator value [Eq. (2.85) or (2.88)] in the case of the perturbation correction. Finally, the tile of the contracted tensor $Z^{(s)}$ is saved to the storage in line 9.

(a)

```
 1  Define subsytems
 2  Loop over subsystems
 3    Initialize T(s)
 4    Loop over iterations for amplitude equations
 5      Calculate T(s)
 6      Calculate correlation energy
 7      Check convergence
 8    End loop
 9    If (calculate perturbation correction) then
10      Initialize Λ(s)
11      Loop over iteration for Λ equations
12        Calculate Λ(s)
13        Check convergence
14      End loop
15      Calculate perturbative energy correction
16      Delete Λ(s)
17    End if
18    Delete T(s)
19  End loop
20  Accumulate subsystem correlation energies
```

(b)

```
 1  Loop over canonical hole/particle tiles
 2    If (non-zero tile by spin symmetry) then
 3      Get one tile of X(s)
 4      Sort X(s)
 5      Get one tile of Y(s)
 6      Sort Y(s)
 7      Calculate factor
 8      Z(s) = factor × X(s) × Y(s)
 9      Add Z(s) to storage
10    End if
11  End loop
```

Figure 2.1. Pseudocodes of (a) a manually written driver subroutine of the D&C-based CC and MPPT methods and (b) a general TCE-synthesized subroutine for binary tensor contraction. The loop for solving the Λ equations is required in case of the CC methods augmented with the second-order RS perturbation correction. $X^{(s)}$, $Y^{(s)}$, and $Z^{(s)}$ denote general tensors defined for the subsystem s.

2.8.3 Numerical assessments

2.8.3.1 Computational details

This subsection assesses the performance of the D&C-based MP2, MP3, MP4, CCSD, CCSDT, CCSDTQ, CCSD(T), and CCSD(2)$_{TQ}$ methods, which were implemented into the in-house program suite. The results of the D&C-free calculations are also shown to verify the present implementation.

The following two levels of Hamiltonians were employed for comparison: the one-electron NR Hamiltonian with the two-electron NR Coulomb interaction (NR/NR) and the SF one-electron IODKH Hamiltonian [24] with the two-electron NR Coulomb interaction (SF-IODKH/NR). In the SF-IODKH/NR calculations, a value of

137.035999676 a.u. was adopted for the speed of light. The point charge model was used to evaluate the nuclear potential terms.

Numerical assessments were performed for hydrogen halides HX (X = F, Cl, Br, I, and At) and their zigzag one-dimensional chains $(HX)_n$ (n = 4–40). The outermost s- and p-electrons were correlated for the halogens. The geometries of HX were fixed as follows unless otherwise indicated. The experimental bond lengths [106] of 0.917, 1.275, 1.414, and 1.609 Å were adopted for X = F, Cl, Br, and I, respectively. The optimized bond length of 1.738 Å, reported in a previous theoretical study [107], was used for X = At. For the $(HX)_n$ calculations, the intra- and inter-molecular bond lengths were optimized at the ωB97X-D [108,109] level using the Stuttgart–Dresden effective core potentials [110-112] and the DZP basis sets [113]. The intra-molecular bond lengths for X = F, Cl, Br, I, and At were 0.973, 1.323, 1.453, 1,639, and 1.729 Å, while the inter-molecular bond lengths were 1.497, 2.341, 2.651, 2.969, and 3.148 Å, respectively. The bond angles were fixed at $\angle XHX = 180°$ and $\angle HXH = 120°$. In the D&C-based calculations for $(HX)_n$, an HX unit was used as a subsystem. The atoms lying within 5.5 Å of each subsystem were treated as the buffer region.

2.8.3.2 D&C-free calculation

This subsection discusses the results of the electron correlation calculations without the D&C technique. First, the behaviors of the potential energy curves for the HAt molecule at the NR/NR and SF-IODKH/NR levels are discussed. Figure 2.2 shows the potential energy curves using the HF, MP2, MP3, MP4, CCSD, CCSD(T), and CCSDT methods. Here, the DZP(-DKH) basis sets [113-116] were adopted. The horizontal axis represents the bond length in Å, while the vertical axis represents the dissociation energy

in kcal/mol. Panel (a) shows the results at the NR/NR level with the RHF reference. In HF, the behavior of the curve is different from those of the other methods. HF underestimates the absolute value of the dissociation energy around the equilibrium region due to a lack of dynamical correlation. Besides, the dissociation energy diverges positively at a large distance. This inaccuracy in the dissociation limit arises from the occupation of the identical spatial orbital by the anti-parallel spin pair. In MP2–4, the reasonably shaped curves are obtained around the equilibrium region. However, they exhibit maxima in the intermediate region, and their energies negatively diverge in the dissociation region. The magnitudes of the maxima are in the order MP2 > MP3 > MP4. The rates of the divergence are expected to be in the order MP3 > MP4 > MP2 from the results at 8.0 Å. The incorrect behaviors of MP2–4 are because the near-degenerate state seen in the dissociation region cannot be generally described by the non-degenerate perturbation theory due to a lack of major static correlation. CCSD and CCSD(T) exhibit the reasonably shaped curves over the entire region. However, they cannot describe the dissociation limit correctly. The energies are overestimated and underestimated by ~3 kcal/mol at 8.0 Å in CCSD and CCSD(T), respectively. In contrast, CCSDT displays the reasonably shaped curve, which converges at the correct dissociation limit. Thus, CCSDT is immune to the inferiority of the RHF reference through the inclusion of the higher-order electron correlation.

Figure 2.2(b) shows the results at the NR/NR level with the UHF reference. The UHF reference improves the behavior of the potential energy curves in all the methods as compared to the RHF reference. Namely, the shapes of the curves are reasonable, and the correct dissociation limit is obtained. In UHF, the absolute value of the dissociation energy around the equilibrium region is considerably underestimated in comparison with

those of the correlation methods, as seen in the RHF case. In MP2–4, the absolute values of the energies around the equilibrium region are improved as compared to those of HF. Another striking feature of MP2–4 is that the curves show a rapid rise in the intermediate region, that is, the curves of MP2–4 possess large curvatures. The rates at which the curves rise decrease in the order MP2 > MP3 > MP4. In CCSD, CCSD(T), and CCSDT, the reasonable curves are obtained with similar behaviors. However, the rates at which the curves rise in the intermediate region slightly differ: CCSD > CCSD(T) > CCSDT.

Figure 2.2(c) shows the potential energy curves at the SF-IODKH/NR level with the UHF reference. The general trends are similar to the NR/NR case, that is, the reasonably shaped curves converging to the correct dissociation limit are obtained. The difference is the shorter equilibrium bond length (by ~0.05 Å) and the smaller absolute value of the dissociation energy around the equilibrium region (by several kcal/mol), which is inconsistent with the chemical intuition, i.e., a shorter bond length leads to a stronger bond. However, this is one of the common relativistic effects, as pointed out by Filatov and Cremer [117]. In this system, the magnitudes of the atomic charges decrease due to the relativistic orbital contraction. The Mulliken charges of the H and At atoms are ±0.08 and ±0.06 a.u. at the NR/NR and SF-IODKH/NR levels, respectively. Consequently, in the SF-IODKH/NR calculation, the polarity of the H–At bond decreases, which results in the smaller absolute value of the dissociation energy.

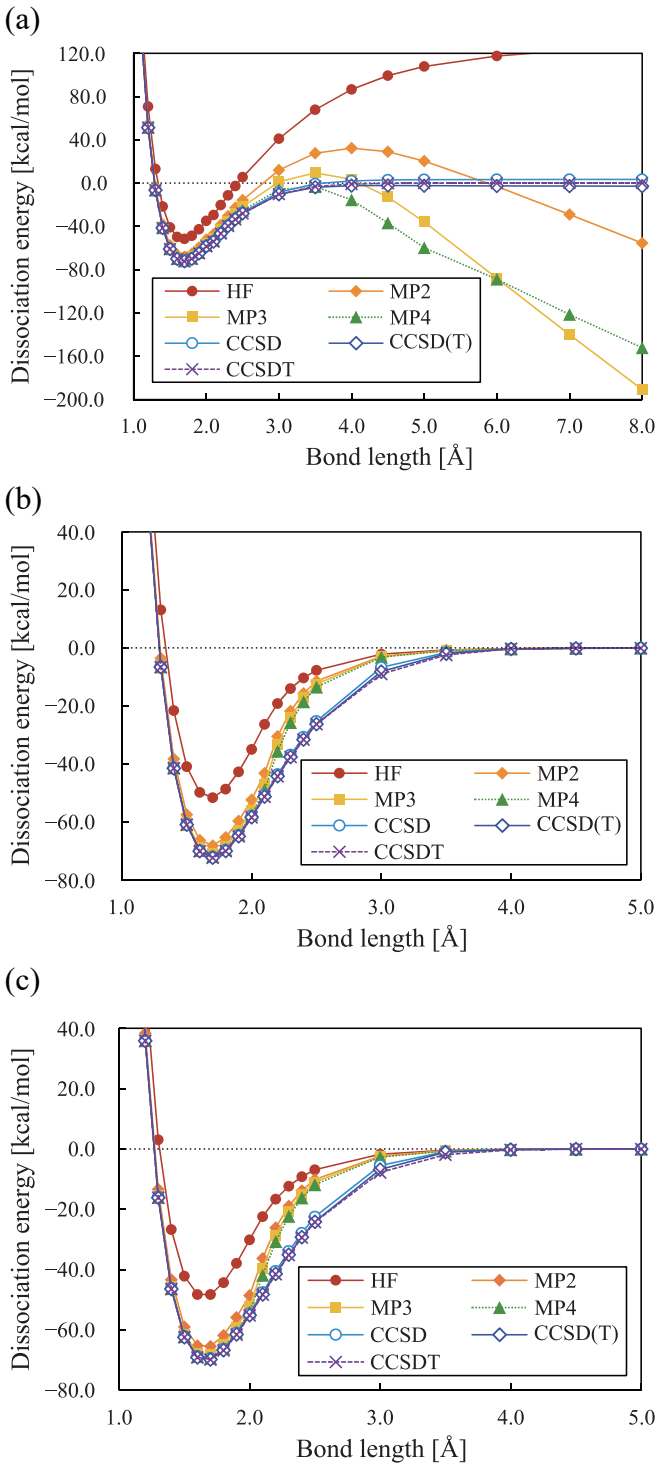

Figure 2.2. Potential energy curves of the HAt molecule using the HF, MP2, MP3, MP4, CCSD, CCSD(T), and CCSDT methods at the (a) NR/NR level with the RHF reference, (b) NR/NR level with the UHF reference, and (c) SF-IODKH/NR level with the UHF reference.

Table 2.1. Equilibrium bond lengths R_e (in Å) and harmonic frequencies ω_e (in cm^{-1}) of the HX molecules (X = F, Cl, Br, and I) using the HF, MP2, CCSD, CCSD(T), and CCSD(2)$_{TQ}$ methods at the NR/NR and SF-IODKH/NR levels. The UHF wavefunction was used as a reference state. The CBS extrapolation was performed with the cc-pVXZ basis sets. The original experimental values [106] are shown in the Exptl. rows, and the deviations from the Exptl. values are shown for the other rows. The relativistic changes Δ are also shown.

Molecule	Method	R_e			ω_e		
		NR/NR	SF-IODKH/NR	Δ	NR/NR	SF-IODKH/NR	Δ
HF	HF	−0.020	−0.020	0.000	337	335	−2
	MP2	0.001	0.001	0.000	−2	−4	−2
	CCSD	−0.003	−0.003	0.000	53	51	−2
	CCSD(T)	0.000	0.000	0.000	3	0	−3
	CCSD(2)$_{TQ}$	0.000	0.000	0.000	3	0	−3
	Exptl.		0.917			4138	
HCl	HF	−0.010	−0.010	0.000	149	144	−5
	MP2	−0.002	−0.002	0.000	50	45	−5
	CCSD	0.000	0.000	0.000	25	19	−6
	CCSD(T)	0.002	0.002	0.000	4	−1	−5
	CCSD(2)$_{TQ}$	0.002	0.002	0.000	3	−2	−5
	Exptl.		1.275			2991	
HBr	HF	−0.007	−0.010	−0.003	147	160	13
	MP2	0.001	−0.002	−0.003	75	70	−5
	CCSD	0.005	0.002	−0.003	48	32	−16
	CCSD(T)	0.007	0.005	−0.002	13	−9	−22
	CCSD(2)$_{TQ}$	0.007	0.005	−0.002	11	−5	−16
	Exptl.		1.414			2648	
HI	HF	−0.001	−0.009	−0.008	182	145	−37
	MP2	0.002	−0.005	−0.007	104	51	−53
	CCSD	0.009	0.002	−0.007	48	29	−19
	CCSD(T)	0.011	0.004	−0.007	33	−11	−44
	CCSD(2)$_{TQ}$	0.011	0.005	−0.006	36	−5	−41
	Exptl.		1.609			2309	

For a more quantitative discussion, Table 2.1 presents the equilibrium bond lengths and the harmonic frequencies for the HX molecules (X = F, Cl, Br, and I) at the NR/NR and SF-IODKH/NR levels using the HF, MP2, CCSD, CCSD(T), and CCSD(2)$_{TQ}$ methods with the UHF reference, and compares them with the experimental data [106]. The original experimental values are shown in the rows labeled as "Exptl.", while the deviations from the experimental values are shown in the other rows. The relativistic changes Δ, which are defined as the differences between the NR/NR and SF-IODKH/NR results, are also presented. Here, the CBS extrapolation [118] was performed based on the calculations with the cc-pVXZ(-DK) basis sets: X = D, T, and Q for the HF calculations and X = T and Q for the correlated calculations. In general, the use of the higher-order correlation methods in tandem with the SF-IODKH/NR Hamiltonian systematically improves the results. The maximum absolute deviation of the bond lengths and the harmonic frequencies from the experimental values are reduced from 0.020 Å and 337 cm^{-1} in the HF calculations at the NR/NR level to 0.005 Å and 5 cm^{-1} in the CCSD(2)$_{TQ}$ calculations at the SF-IODKH/NR level. The latter is theoretically the best combination of all the methods here.

Next, the values of Δ are discussed. For HF and HCl, the relativistic effect does not affect the equilibrium bond lengths in the order of 0.001 Å. On the other hand, the relativistic effect reduces the harmonic frequencies by 2–3 and 5–6 cm^{-1} for HF and HCl, respectively, irrespective of the wavefunction theory. This implies the additivity of the relativistic and electron correlation effects. In contrast, for HBr and HI, where the relativistic effect is more significant, the equilibrium bond lengths shorten by 0.002–0.003 and 0.006–0.008 Å, respectively. The relativistic effect on the harmonic frequencies of HBr and HI varies according to the wavefunction theory, ranging from −22 to 13 cm^{-1}

in HBr and from −53 to −19 cm^{-1} in HI. Thus, the larger the relativistic effect, the more dependent are the results on the choice of the correlation methods.

Consequently, the results shown above are consistent with the well-known behaviors of the CC and MPPT methods [107,117,119,120], indicating the validity of the present implementation of these methods without the D&C technique.

2.8.3.3 D&C-based calculation

This subsection discusses the results of the electron correlation calculations for one-dimensional hydrogen halide chains $(HX)_n$ (X = F, Cl, Br, I, and At) using the D&C technique. First, the accuracy of the D&C-based correlation methods is examined. Table 2.2 shows the correlation energies (in hartrees) of $(HX)_6$ evaluated by MP2, CCSD, CCSD(T), and $CCSD(2)_{TQ}$ with and without the D&C scheme at the SF-IODKH/NR level. The deviations of the D&C-based methods are shown as Δ. Hereafter, the Sapporo-(DKH3-)DZP-2012 basis sets [121,122] and the UHF reference were adopted for the calculations of $(HX)_n$. MP2, CCSD, CCSD(T), and $CCSD(2)_{TQ}$ accord similar small absolute values of Δ to each other, which is less than one millihartree. This indicates the validity of the D&C scheme regardless of the correlation methods. Besides, $CCSD(2)_{TQ}$ shows very similar behavior to CCSD(T) in these systems.

Next, the hydrogen bond energies of $(HX)_n$ are examined. Table 2.3 summarizes the averaged hydrogen bond energies (in kcal/mol) for n = 10–40 evaluated by HF, MP2, CCSD, CCSD(T), and $CCSD(2)_{TQ}$ using the D&C method at the NR/NR and SF-IODKH/NR levels. Here, the averaged hydrogen bond energy is defined as $\left(nE\left[\mathrm{HX}\right]-E\left[(\mathrm{HX})_n\right]\right)/\left(n-1\right)$, where $E\left[\cdots\right]$ indicates the total energy of the system. In all the correlation methods, the bond energies of X = F, Cl, Br, and I asymptotically

increase as n increases at both the NR/NR and SF-IODKH/NR levels. For X = At, although the slightly deviated behavior appears at $n = 10$, the bond energy asymptotically decreases with increasing n. Namely, the influence of the chain lengths becomes smaller with their increase. The HF method gives the lower bond energies than do the correlation methods for X = F, and the non-physical negative bond energies for X = Cl, Br, I, and At. This reflects that the dispersion interaction described by the dynamical correlation positively contributes to the energies of the hydrogen bonds. MP2 and CCSD give the larger and smaller bond energies, respectively, than does $CCSD(2)_{TQ}$, which is theoretically the best method here. These behaviors imply the overestimation and underestimation of the magnitude of the dispersion interaction by MP2 and CCSD, respectively. The energy values obtained by CCSD(T) are very close to those of $CCSD(2)_{TQ}$; the maximum absolute deviation is 0.062 kcal/mol for $(HF)_{40}$ at the SF-IODKH/NR level.

Table 2.2. Correlation energies (in hartrees) of the $(HX)_6$ chains (X = F, Cl, Br, I, and At) using the MP2, CCSD, CCSD(T), and CCSD(2)$_{TQ}$ methods with and without (w/o) the D&C scheme at the SF-IODKH/NR level. The deviations of the D&C-based methods Δ are also shown.

Molecule	MP2			CCSD			CCSD(T)			CCSD(2)$_{TQ}$		
	w/o D&C	D&C	Δ	w/o D&C	D&C	Δ	w/o D&C	D&C	Δ	w/o D&C	D&C	Δ
$(HF)_6$	−1.330612	−1.330612	0.000000	−1.348409	−1.348376	−0.000033	−1.365687	−1.365657	−0.000031	−1.367816	−1.367786	−0.000031
$(HCl)_6$	−0.950040	−0.950026	−0.000014	−1.050525	−1.050513	−0.000011	−1.072010	−1.071995	−0.000014	−1.073681	−1.073667	−0.000014
$(HBr)_6$	−0.815851	−0.815654	−0.000197	−0.899573	−0.899426	−0.000147	−0.918873	−0.918694	−0.000180	−0.920306	−0.920126	−0.000180
$(HI)_6$	−0.701942	−0.701710	−0.000232	−0.787503	−0.787322	−0.000181	−0.804999	−0.804786	−0.000212	−0.806253	−0.806041	−0.000213
$(HAt)_6$	−0.656375	−0.656153	−0.000222	−0.740182	−0.740007	−0.000176	−0.758176	−0.757969	−0.000207	−0.759358	−0.759151	−0.000208

Table 2.3. Averaged hydrogen bond energies (in kcal/mol) of the $(HX)_n$ chains (X = F, Cl, Br, I, and At; n = 10–40) using the HF, MP2, CCSD, CCSD(T), and $CCSD(2)_{TQ}$ methods with the D&C scheme at the NR/NR and SF-IODKH/NR levels.

Molecule	n	NR/NR					SF-IODKH/NR				
		HF	MP2	CCSD	CCSD(T)	$CCSD(2)_{TQ}$	HF	MP2	CCSD	CCSD(T)	$CCSD(2)_{TQ}$
$(HF)_n$	10	9.057	10.709	9.882	10.186	10.131	9.039	10.695	9.864	10.170	10.114
	20	9.752	11.427	10.589	10.898	10.839	9.733	11.414	10.572	10.882	10.822
	30	9.982	11.664	10.827	11.137	11.076	9.964	11.650	10.809	11.120	11.060
	40	10.097	11.782	10.943	11.254	11.193	10.078	11.769	10.926	11.238	11.176
$(HCl)_n$	10	−0.146	1.947	1.234	1.465	1.465	−0.178	1.985	1.270	1.501	1.501
	20	−0.246	2.052	1.331	1.563	1.563	−0.277	2.088	1.366	1.598	1.598
	30	−0.279	2.086	1.363	1.596	1.596	−0.309	2.122	1.397	1.630	1.630
	40	−0.296	2.103	1.379	1.612	1.612	−0.326	2.139	1.413	1.646	1.646
$(HBr)_n$	10	−0.182	1.392	0.844	1.015	1.015	−0.203	1.365	0.816	0.987	0.987
	20	−0.133	1.441	0.889	1.061	1.061	−0.157	1.412	0.858	1.029	1.029
	30	−0.116	1.457	0.903	1.076	1.076	−0.142	1.427	0.871	1.043	1.043
	40	−0.108	1.465	0.911	1.083	1.083	−0.135	1.434	0.878	1.050	1.050
$(HI)_n$	10	−0.778	0.805	0.292	0.459	0.459	−0.724	0.838	0.329	0.491	0.491
	20	−0.755	0.829	0.313	0.480	0.480	−0.704	0.858	0.346	0.509	0.509
	30	−0.748	0.836	0.320	0.487	0.487	−0.698	0.864	0.352	0.515	0.515
	40	−0.744	0.840	0.323	0.490	0.490	−0.695	0.868	0.355	0.518	0.518
$(HAt)_n$	10	−0.776	0.781	0.301	0.461	0.461	−0.715	0.818	0.341	0.497	0.497
	20	−0.766	0.793	0.311	0.471	0.471	−0.709	0.826	0.348	0.504	0.504
	30	−0.770	0.789	0.307	0.467	0.467	−0.715	0.820	0.342	0.498	0.498
	40	−0.773	0.786	0.305	0.465	0.465	−0.718	0.817	0.340	0.496	0.496

Finally, the computational cost of the D&C-based correlation methods is examined. Figure 2.3 shows the system-size dependence of the CPU time of the MP2, MP3, MP4, CCSD, CCSDT, CCSDTQ, CCSD(T), and CCSD(2)$_{TQ}$ calculations for $(HF)_n$ (n = 4–20) with and without the D&C method at the SF-IODKH/NR level. The MPPT and CC results are presented in panels (a) and (b), respectively. The horizontal axis represents the number of molecules n, while the vertical axis represents the CPU times in minutes on a logarithmic scale. The times taken for the HF calculations are not included. The CPU times were measured using 16 cores of an Intel Xeon E5-2690 (2.90 GHz) processor. Based on the D&C approach, the CPU times for all the correlation methods drastically decrease. The computational scaling reduces from $O(n^{5.1})$ to $O(n^{1.1})$ in MP2, $O(n^{6.1})$ to $O(n^{1.1})$ in MP3, $O(n^{7.1})$ to $O(n^{1.1})$ in MP4, $O(n^{6.0})$ to $O(n^{1.1})$ in CCSD, $O(n^{8.1})$ to $O(n^{1.1})$ in CCSDT, $O(n^{10.2})$ to $O(n^{1.1})$ in CCSDTQ, $O(n^{7.1})$ to $O(n^{1.1})$ in CCSD(T), and $O(n^{9.1})$ to $O(n^{1.2})$ in CCSD(2)$_{TQ}$. The fifth power scaling of the present MP2 method is due to solving the amplitude equation iteratively, as explained in Sec. 2.8.2.3. On the other hand, the common implementation of the canonical MP2 method adopts the non-iterative, one-shot algorithm, which is known to approximately scale as the fourth power (disregarding the integral-transformation step). The similar computational times between the (D&C-)CCSD and (D&C-)MP3 methods, both of which scale as the sixth power of the system size, are for the same reason. Consequently, the present D&C-based methods achieve a quasi-linear-scaling computational cost with respect to the system size.

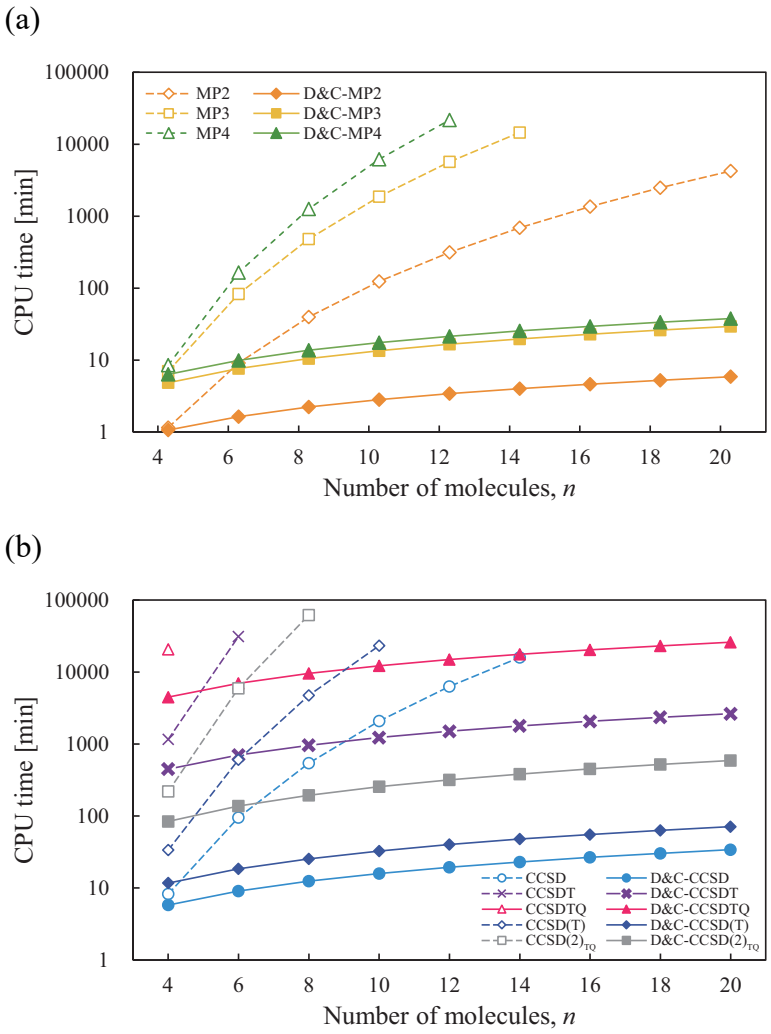

Figure 2.3. System-size dependence of the CPU time of the electron correlation calculations for the $(HF)_n$ chains (n = 4–20) with and without the D&C scheme at the SF-IODKH/NR level: (a) MP2, MP3, and MP4 calculations; (b) CCSD, CCSDT, CCSDTQ, CCSD(T), and $CCSD(2)_{TQ}$ calculations. 16 cores of an Intel Xeon E5-2690 (2.90 GHz) processor were used.

2.8.4 Conclusion

In this section, the higher-order CC and MPPT methods as well as their combinations compatible with the NR and SF relativistic calculations were implemented using the computerized symbolic algebra system TCE, and extended to the linear-scaling D&C scheme. For the standard CC and MPPT methods, such as MP2–4, CCSD, CCSDT, and CCSDTQ, Nesbet's energy expression was applied to the general excitation order to

define the subsystem correlation energy in the D&C scheme, together with the EDA technique. For the CC methods augmented with the perturbation correction, such as CCSD(T) and CCSD(2)$_{TQ}$, which do not follow Nesbet's formula, the general formulation of the D&C-based perturbation correction was proposed by means of the EDA partitioning.

For the numerical assessment of the D&C-free correlation methods, the potential energy curves, equilibrium bond lengths, and harmonic vibration frequencies of hydrogen halides were evaluated. Based on the UHF reference, all the MPPT and CC methods produced the reasonably shaped curves converging at the correct dissociation limit at both the NR/NR and SF-IODKH/NR levels. The equilibrium bond lengths and harmonic frequencies obtained by the combination of SF-IODKH/NR and CCSD(2)$_{TQ}$ agreed well with the experimental data within the errors of 0.005 Å and 5 cm^{-1}, respectively.

The accuracy and the computational cost of the D&C-based correlation methods were also assessed for one-dimensional hydrogen halide chains. The D&C-based methods achieved a high degree of accuracy within millihartree orders of errors from the results of the D&C-free methods. The CPU times of the D&C-based methods were considerably smaller as compared to those of the D&C-free methods. The present methods achieved quasi-linear-scaling computational cost with respect to the system size.

References

[1] P. A. M. Dirac, *Proc. R. Soc. London, Ser. A* **117**, 610 (1928).

[2] M. Iliaš, T. Saue, *J. Chem. Phys.* **126**, 064102 (2007).

[3] W. Liu, *Mol. Phys.* **108**, 1679 (2010).

[4] L. L. Foldy, S. A. Wouthuysen, *Phys. Rev.* **78**, 29 (1950).

[5] M. Douglas, N. M. Kroll, *Ann. Phys. (Leipzig)* **82**, 89 (1974).

[6] B. A. Hess, *Phys. Rev. A* **32**, 756 (1985).

[7] B. A. Hess, *Phys. Rev. A* **33**, 3742 (1986).

[8] T. Nakajima, K. Hirao, *J. Chem. Phys.* **113**, 7786 (2000).

[9] C. van Wüllen, *J. Chem. Phys.* **120**, 7307 (2004).

[10] A. Wolf, M. Reiher, B. A. Hess, *J. Chem. Phys.* **117**, 9215 (2002).

[11] M. Reiher, A. Wolf, *J. Chem. Phys.* **121**, 10945 (2004).

[12] D. Peng, K. Hirao, *J. Chem. Phys.* **130**, 044102 (2009).

[13] C. Chang, M. Pelissier, P. Durand, *Phys. Scr.* **34**, 394 (1986).

[14] E. van Lenthe, E. J. Baerends, J. G. Snijders, *J. Chem. Phys.* **99**, 4597 (1993).

[15] E. van Lenthe, E. J. Baerends, J. G. Snijders, *J. Chem. Phys.* **101**, 9783 (1994).

[16] K. G. Dyall, E. van Lenthe, *J. Chem. Phys.* **111**, 1366 (1999).

[17] T. Nakajima, K. Hirao, *Chem. Phys. Lett.* **302**, 383 (1999).

[18] K. G. Dyall, *J. Chem. Phys.* **106**, 9618 (1997).

[19] K. G. Dyall, *J. Chem. Phys.* **115**, 9136 (2001).

[20] K. G. Dyall, *J. Comput. Chem.* **23**, 786 (2002).

[21] D. Peng, W. Liu, Y. Xiao, L. Cheng, *J. Chem. Phys.* **127**, 104106 (2007).

[22] M. Barysz, A. J. Sadlej, J. G. Snijders, *Int. J. Quantum Chem.* **65**, 225 (1997).

[23] M. Barysz, *J. Chem. Phys.* **114**, 9315 (2001).

[24] M. Barysz, A. J. Sadlej, *J. Chem. Phys.* **116**, 2696 (2002).

[25] D. Kędziera, M. Barysz, *J. Chem. Phys.* **121**, 6719 (2004).

[26] W. Kutzelnigg, W. Liu, *J. Chem. Phys.* **123**, 241102 (2005).

[27] W. Liu, W. Kutzelnigg, *J. Chem. Phys.* **126**, 114107 (2007).

[28] W. Kutzelnigg, W. Liu, *Mol. Phys.* **104**, 2225 (2006).

[29] M. Iliaš, H. J. Aa. Jensen, V. Kellö, B. O. Roos, M. Urban, *Chem. Phys. Lett.* **408**, 210 (2005).

[30] J. Seino, M. Hada, *Chem. Phys. Lett.* **461**, 327 (2008).

[31] J. Seino, H. Nakai, *J. Chem. Phys.* **136**, 244102 (2012).

[32] J. Seino, H. Nakai, *J. Chem. Phys.* **137**, 144101 (2012).

[33] R. Seeger, J. A. Pople, *J. Chem. Phys.* **66**, 3045 (1977).

[34] H. Fukutome, *Int. J. Quantum Chem.* **20**, 955 (1981).

[35] J.-L. Calais, *Adv. Quantum Chem.* **17**, 225 (1985).

[36] R. McWeeny, Methods of Molecular Quantum Mechanics, Academic Press, London, 1989.

[37] P.-O. Löwdin, I. Mayer, *Adv. Quantum Chem.* **24**, 79 (1992).

[38] S. Hammes-Schiffer, H. C. Andersen, *J. Chem. Phys.* **99**, 1901 (1993).

[39] S. K. Wolff, D. Jayatilaka, G. S. Chandler, *J. Chem. Phys.* **103**, 4562 (1995).

[40] D. Jayatilaka, *J. Chem. Phys.* **108**, 7587 (1998).

[41] J. L. Stuber, J. Paldus, in: E. J. Brändas, E. S. Kryachko (Eds.), Fundamental World of Quantum Chemistry, Kluwer Academic Publishers, Dordrecht, 2003, p. 67.

[42] M. K. Armbruster, F. Weigend, C. van Wüllen, W. Klopper, *Phys. Chem. Chem. Phys.* **10**, 1748 (2008).

[43] P. Hafner, W. H. E. Schwarz, *Chem. Phys. Lett.* **65**, 537 (1979).

[44] P. Hafner, *J. Phys. B: At., Mol. Opt. Phys.* **13**, 3297 (1980).

[45] N. Rösch, *Chem. Phys.* **80**, 1 (1983).

[46] S. Y. Lee, Y. S. Lee, *J. Comput. Chem.* **13**, 595 (1992).

[47] W. Yang, *Phys. Rev. Lett.* **66**, 1438 (1991).

[48] M. Kobayashi, H. Nakai, in: R. Zaleśny, M. G. Papadopoulos, P. G. Mezey, J. Leszczynski (Eds.), Linear-Scaling Techniques in Computational Chemistry and Physics, Springer, Dordrecht, 2011, p. 97.

[49] M. Kobayashi, H. Nakai, *Phys. Chem. Chem. Phys.* **14**, 7629 (2012).

[50] P. A. M. Dirac, *Proc. R. Soc. London, Ser. A* **126**, 360 (1930).

[51] J. A. Gaunt, *Proc. R. Soc. London, Ser. A* **122**, 513 (1929).

[52] G. Breit, *Phys. Rev.* **34**, 553 (1929).

[53] K. G. Dyall, K. Faegri, Introduction to Relativistic Quantum Chemistry, Oxford University Press, New York, 2007.

[54] W. Pauli, *Z. Phys.* **43**, 601.

[55] T. Saue, H. J. A. Jensen, *J. Chem. Phys.* **111**, 6211 (1999).

[56] W. H. Press, S. A. Teukolsky, W. T. Vetterling, B. P. Flannery, Numerical Recipes in FORTRAN, Cambridge University Press, Cambridge, 1992.

[57] K. Raghavachari, G. W. Trucks, J. A. Pople, M. Head-Gordon, *Chem. Phys. Lett.* **157**, 479 (1989).

[58] T. J. Lee, G. E. Scuseria, Quantum Mechanical Electronic Structure Calculations with Chemical Accuracy, Kluwer Academic Publishers, Dordrecht, 1995.

[59] M. Urban, J. Noga, S. J. Cole, R. J. Bartlett, *J. Chem. Phys.* **83**, 4041 (1985).

[60] K. Kowalski, P. Piecuch, *J. Chem. Phys.* **113**, 18 (2000).

[61] K. Kowalski, P. Piecuch, *J. Mol. Struct. (THEOCHEM)* **547**, 191 (2001).

[62] N. Oliphant, L. Adamowicz, *J. Chem. Phys.* **96**, 3739 (1992).

[63] N. Oliphant, L. Adamowicz, *Int. Rev. Phys. Chem.* **12**, 339 (1993).

[64] L. Adamowicz, P. Piecuch, K. B. Ghose, *Mol. Phys.* **94**, 225 (1998).

[65] N. Oliphant, L. Adamowicz, *J. Chem. Phys.* **95** (1991).

[66] P. Piecuch, L. Adamowicz, *J. Chem. Phys.* **100**, 5792 (1994).

[67] S. R. Gwaltney, M. Head-Gordon, *J. Chem. Phys.* **115**, 2014 (2001).

[68] K. Kowalski, P. Piecuch, *J. Chem. Phys.* **113**, 5644 (2000).

[69] K. Kowalski, P. Piecuch, *Chem. Phys. Lett.* **344**, 165 (2001).

[70] P. Piecuch, S. A. Kucharski, K. Kowalski, *Chem. Phys. Lett.* **344** (2001).

[71] P. Piecuch, M. Włoch, *J. Chem. Phys.* **123**, 224105 (2005).

[72] P. Piecuch, M. Włoch, J. R. Gour, A. Kinal, *Chem. Phys. Lett.* **418**, 463 (2005).

[73] M. Włoch, M. D. Lodriguito, P. Piecuch, J. R. Gour, *Mol. Phys.* **104**, 2149 (2006).

[74] I. Shavitt, R. J. Bartlett, Many-Body Methods in Chemistry and Physics: MBPT and Coupled-Cluster Theory, Cambridge University Press, New York, 2009.

[75] M. Kállay, P. R. Surján, *J. Chem. Phys.* **113**, 1359 (2000).

[76] S. Hirata, *Theor. Chem. Acc.* **116**, 2 (2006).

[77] S. Hirata, *J. Phys. Chem. A* **107**, 9887 (2003).

[78] S. Hirata, *J. Chem. Phys.* **121**, 51 (2004).

[79] S. Hirata, P. D. Fan, A. A. Auer, M. Nooijen, P. Piecuch, *J. Chem. Phys.* **121**, 12197 (2004).

[80] S. Hirata, *J. Chem. Phys.* **122**, 094105 (2005).

[81] P. D. Fan, S. Hirata, *J. Chem. Phys.* **124**, 104108 (2006).

[82] M. Kamiya, S. Hirata, *J. Chem. Phys.* **125**, 074111 (2006).

[83] S. Li, J. Ma, Y. Jiang, *J. Comput. Chem.* **23**, 237 (2002).

[84] W. Li, P. Piecuch, J. R. Gour, S. Li, *J. Chem. Phys.* **131**, 114109 (2009).

[85] W. Li, P. Piecuch, *J. Phys. Chem. A* **114**, 8644 (2010).

[86] D. G. Fedorov, K. Kitaura, *J. Chem. Phys.* **123**, 134103 (2005).

[87] H. Stoll, *Chem. Phys. Lett.* **191**, 548 (1992).

[88] J. Friedrich, M. Hanrath, M. Dolg, *J. Chem. Phys.* **126**, 154110 (2007).

[89] J. Friedrich, M. Hanrath, M. Dolg, *Z. Phys. Chem.* **224**, 513 (2010).

[90] M. Ziółkowski, B. Jansík, T. Kjærgaard, P. Jørgensen, *J. Chem. Phys.* **133**, 014107 (2010).

[91] W. T. Yang, T. S. Lee, *J. Chem. Phys.* **103**, 5674 (1995).

[92] T. Akama, M. Kobayashi, H. Nakai, *J. Comput. Chem.* **28**, 2003 (2007).

[93] T. Akama, M. Kobayashi, H. Nakai, *Int. J. Quantum Chem.* **109**, 2706 (2009).

[94] T. Akama, A. Fujii, M. Kobayashi, H. Nakai, *Mol. Phys.* **105**, 2799 (2010).

[95] M. Kobayashi, Y. Imamura, H. Nakai, *J. Chem. Phys.* **127**, 074103 (2007).

[96] T. Yoshikawa, M. Kobayashi, H. Nakai, *Theor. Chem. Acc.* **130**, 411 (2011).

[97] M. Kobayashi, H. Nakai, *J. Chem. Phys.* **129**, 044103 (2008).

[98] M. Kobayashi, H. Nakai, *J. Chem. Phys.* **131**, 114108 (2009).

[99] T. Yoshikawa, M. Kobayashi, H. Nakai, *Int. J. Quantum Chem.* **113**, 218 (2013).

[100] J. Seino, H. Nakai, *J. Chem. Phys.* **139**, 034109 (2013).

[101] H. Nakai, *Chem. Phys. Lett.* **363**, 73 (2002).

[102] R. K. Nesbet, *Adv. Chem. Phys.* **14**, 1 (1969).

[103] S. Hirata, M. Nooijen, I. Grabowski, R. J. Bartlett, *J. Chem. Phys.* **114**, 3919 (2001).

[104] S. Hirata, M. Nooijen, I. Grabowski, R. J. Bartlett, *J. Chem. Phys.* **115**, 3967 (2001).

[105] S. Hirata, Electron-correlation theory algebraic equation database, 2010.

[106] K. P. Huber, G. Herzberg, Molecular Spectra and Molecular Structure, IV. Constants

of Diatomic Molecules, Van Nostrand Reinhold, New York, 1950.

[107] L. Visscher, J. Styszyñski, W. C. Nieuwpoort, *J. Chem. Phys.* **105**, 1987 (1996).

[108] J. D. Chai, M. Head-Gordon, *Phys. Chem. Chem. Phys.* **10**, 6615 (2008).

[109] J. D. Chai, M. Head-Gordon, *J. Chem. Phys.* **128**, 084106 (2008).

[110] M. Dolg, U. Wedig, H. Stoll, H. Preuss, *J. Chem. Phys.* **86**, 866 (1987).

[111] D. Andrae, U. Häußermann, M. Dolg, H. Stoll, H. Preuß, *Theor. Chim. Acta* **77**, 123 (1990).

[112] H. Stoll, B. Metz, M. Dolg, *J. Comput. Chem.* **23**, 767 (2002).

[113] A. Canal Neto, E. P. Muniz, R. Centoducatte, F. E. Jorge, *J. Mol. Struct. (THEOCHEM)* **718**, 219 (2005).

[114] G. G. Camiletti, S. F. Machado, F. E. Jorge, *J. Comput. Chem.* **29**, 2434 (2008).

[115] F. E. Jorge, A. Canal Neto, G. G. Camiletti, S. F. Machado, *J. Chem. Phys.* **130**, 064108 (2009).

[116] A. Canal Neto, F. E. Jorge, *Chem. Phys. Lett.* **582**, 158 (2013).

[117] M. Filatov, D. Cremer, *Phys. Chem. Chem. Phys.* **5**, 1103 (2003).

[118] T. Helgaker, W. Klopper, H. Koch, J. Noga, *J. Chem. Phys.* **106**, 9639 (1997).

[119] A. Dutta, C. D. Sherrill, *J. Chem. Phys.* **118**, 1610 (2003).

[120] A. G. Taube, R. J. Bartlett, *J. Chem. Phys.* **128**, 044110 (2008).

[121] T. Noro, M. Sekiya, T. Koga, *Theor. Chem. Acc.* **131**, 1124 (2012).

[122] T. Noro, M. Sekiya, T. Koga, *Theor. Chem. Acc.* **132**, 1363 (2013).

Chapter 3

Assessment of self-consistent field convergence in spin-dependent relativistic calculations

3.1 Introduction

In chemistry and physics, relativistic effects are vital to accurately describe the heavier elements. These effects are classified into two primary types: SF or scalar relativistic effects, which are mainly responsible for orbital contraction and expansion; and SD effects, which induce energy level splitting through the coupling of orbital and spin angular momenta. In quantum chemical calculations, SF effects are included by perturbative treatments or by using the same ansatz as an NR treatment. SD effects can be considered by using either the SOCI method or perturbative treatments [1,2]. These schemes for the SD effects are effective for light elements, whose relativistic effects are comparatively small, and the SD effects of these systems can be treated as an additional correction to the NR or SF relativistic calculations. Alternative approaches to include SD effects are the two- and four-component relativistic methods [3-17]. These treatments give accurate results across the whole periodic table because the relativistic effects are explicitly considered in the SCF calculations.

In SD calculations, generally, the spin symmetries of the two- and four-component relativistic wavefunctions are broken because spin is not a good quantum number. To describe the correct spin behavior, the GHF method [18-27], where any symmetry constraints are removed, can be used instead of either the RHF or UHF. Because the additional spin degrees of freedom rotate the spin-quantized axes independently, GHF is

also termed a non-collinear method.

However, it is well-known that the convergence in GHF calculations is difficult due to the additional spin degrees of freedom. This sometimes causes the calculations to fall into a higher energy saddle point. One solution for the local minima problem is an extension of the second-order orbital optimization scheme to GHF, which has been proposed by Goings et al. [28]. In this chapter, the author tackles the convergence problem in the GHF calculations from the viewpoint of the SCF acceleration techniques. Here, four acceleration techniques, which are typical for NR calculations, are implemented to GHF. The first method is the use of a damping algorithm, the simplest form of acceleration algorithm. The second, and most popular, method is Pulay's DIIS method [29,30]. A number of variants of the DIIS algorithm have been developed, and these also accelerate SCF convergence [31-35]. One DIIS variant, the EDIIS method developed by Kudin et al. [31], is also assessed in this chapter. The fourth scheme assessed here is a combination algorithm comprising the DIIS and EDIIS algorithms, denoted as EDIIS+DIIS. This algorithm was assessed by Garza and Scuseria [36], and Sulzer et al. [35], and they concluded that this combination algorithm is the best choice for NR molecular calculations.

This chapter is organized as follows: Section 3.2 briefly presents theoretical aspects of the SCF acceleration techniques. Then, the numerical assessments are shown and discussed in Sec. 3.3, and concluding remarks are given in Sec. 3.4.

3.2 Theoretical aspects

This section provides brief explanations of the SCF acceleration algorithms in the GHF framework. Here, five techniques to solve the GHF-based RH equation [Eq. (2.54)]

are used. The first is the FP algorithm, which uses no acceleration techniques. The second is the static damping algorithm, whose equation is written as

$$\mathbf{D}^{\text{new}} = \kappa \mathbf{D}_{i-1} + (1-\kappa)\mathbf{D}_i, \tag{3.1}$$

where $\mathbf{D}_i$ denotes the density matrix in the *i*-th iteration and κ is the weighting factor. In the NR calculations, the damping algorithm is stable, but its rate of convergence is slow.

The other techniques used here are related to the DIIS algorithm. In these algorithms, a new density matrix is estimated by the linear combination of the density matrices from the previous SCF iterations,

$$\mathbf{D} = \sum_{i=1}^{n} c_i \mathbf{D}_i , \tag{3.2}$$

where n is the number of the dimension of the DIIS subspace. This treatment is also available for the Fock matrix instead of the density matrix because of the linear relationship between the density and Fock matrices. The third techniques used here is the conventional DIIS method, which optimizes the coefficients $\{c_i\}$ by minimizing the so-called DIIS error vector $\mathbf{e}$. The error vector is commonly given by $\mathbf{e} = [\mathbf{F}, \mathbf{D}] = \mathbf{FD} - \mathbf{DF}$ in an orthonormal basis. This is because $[\mathbf{F}, \mathbf{D}] = 0$ is the necessary condition for a converged SCF. The optimal DIIS coefficients are mathematically given by

$$\{c_i\} = \arg\inf \left\{ \left\langle \sum_{j=1}^{n} c_j \mathbf{e}_j \middle| \sum_{k=1}^{n} c_k \mathbf{e}_k \right\rangle, \quad \sum_{i=1}^{n} c_i = 1 \right\}. \tag{3.3}$$

Here, the working equation to obtain the coefficients is written as

$$\begin{pmatrix} \mathbf{B} & \mathbf{1}^{\mathrm{t}} \\ \mathbf{1} & 0 \end{pmatrix} \begin{pmatrix} \mathbf{c} \\ \lambda \end{pmatrix} = \begin{pmatrix} \mathbf{0} \\ 1 \end{pmatrix}, \tag{3.4}$$

where

$$B_{ij} = \left\langle \mathbf{e}_i \middle| \mathbf{e}_j \right\rangle, \tag{3.5}$$

$$\mathbf{c}_i = \left(c_1, \quad c_2, \quad \cdots, \quad c_n\right)^{\mathrm{t}}, \tag{3.6}$$

$$\mathbf{1} = \left(1, \quad 1, \quad \cdots, \quad 1\right)^{\mathrm{t}}. \tag{3.7}$$

Here, λ is a Lagrange multiplier. Equation (3.4) is a linear equation and is solved by matrix inversion. In the NR calculations, DIIS performance is known to depend on the initial guess, although the rate of convergence is fast. In the RHF/UHF calculations for the relativistic Hamiltonian including only SF terms, denoted as SF-RHF/UHF, Eq. (3.4) can be straightforwardly applied. On the other hand, in the GHF calculations for the relativistic Hamiltonian involving not only SF terms but also SD ones, denoted as SD-GHF, the Fock and density matrices become complex and have dimensions twice the size of those of NR and SF relativistic calculations. Thus, Eq. (3.4) is solved in complex space.

The fourth technique is the EDIIS method. The coefficients for the linear combination of the previously iterated density matrices is given by

$$\left\{c_i\right\} = \arg\inf\left\{ E^{\mathrm{HF}}\left(\sum_{i=1}^{n} c_i \mathbf{D}_i\right), \quad \sum_{i=1}^{n} c_i = 1, \quad c_i \in \left[0,1\right] \right\}, \tag{3.8}$$

where E^{HF} is the HF energy functional, which is defined as,

$$E^{\mathrm{HF}}\left(\sum_{i=1}^{n} c_i \mathbf{D}_i\right) = \sum_{i=1}^{n} c_i E^{\mathrm{HF}}\left(\mathbf{D}_i\right) - \frac{1}{4}\sum_{i=1}^{n}\sum_{j=1}^{n} c_i c_j \left\langle \mathbf{D}_i - \mathbf{D}_j \middle| \mathbf{F}_i - \mathbf{F}_j \right\rangle. \tag{3.9}$$

This means that the EDIIS coefficients are chosen to minimize the HF energy functional. The minimization problem under the restriction of $c_i \in \left[0,1\right]$ is solved by constrained optimization methods such as the reduced gradient algorithm [37]. EDIIS is known to work efficiently even if the SCF calculation starts from poor initial guess orbitals.

However, the rate of convergence is slower near the minimum than that of DIIS. The imaginary part of the second term of Eq. (3.9) is normally approximated to be zero even in complex SD-GHF calculations. Thus, for minimization, real coefficients have been used.

The final and fifth technique is a combination algorithm comprising DIIS and EDIIS, known as EDIIS+DIIS. As described before, EDIIS is efficient even when starting with a poor initial guess and DIIS is efficient near the minimum. Thus, a combination algorithm is more efficient than either of the algorithms separately. Here, a similar EDIIS+DIIS algorithm to that used in a previous study of NR calculations [36] are adopted. In the early steps, EDIIS is used alone, until the largest absolute element of the DIIS error vector is less than 10^{-1} a.u. In the region where the largest absolute element is between 10^{-1} and 10^{-4} a.u., the coefficients for the linear combination of the density matrices can be given by

$$\mathbf{c} = 10\max\{e_p^n\}\mathbf{c}^{\mathrm{EDIIS}} + \left(1 - 10\max\{e_p^n\}\right)\mathbf{c}^{\mathrm{DIIS}}, \tag{3.10}$$

where $\mathbf{c}^{\mathrm{EDIIS}}$ and $\mathbf{e}^{\mathrm{DIIS}}$ are the EDIIS and DIIS coefficients, respectively. Here $\max\{e_p^n\}$ denotes the largest element of the DIIS error vector in the present (n-th) iteration. Finally, in the region where $\max\{e_p^n\}$ is less than 10^{-4} a.u., DIIS is used alone until SCF convergence is achieved.

3.3 Numerical assessments

3.3.1 Computational details

This subsection describes the computational details used to assess the acceleration techniques in GHF. The three DIIS-related algorithms (DIIS, EDIIS, and EDIIS+DIIS)

were implemented in the in-house program. For comparison, the simple FP and damping algorithms were also used. In the damping algorithm, the weighting factor for the previous density matrix was fixed to $\kappa = 0.25$. The maximum number of the dimension of the DIIS and EDIIS subspaces, i.e., the number of the density and Fock matrices involved in the linear combination, was fixed to 20. The efficiencies of the five algorithms were numerically assessed through SD-GHF level calculations. For comparison of the SCF convergence behavior, SF-RHF/UHF calculations, generally giving better convergence behavior than SD-GHF, were also performed. It should be noted that SF-RHF/UHF methods generally cannot describe SO interactions, stable spin states of non-collinear spin systems, and so forth. For the relativistic Hamiltonian, IODKH/NR [13] was adopted. The SD-GHF calculations with the IODKH/NR Hamiltonian include SO interactions, while the SF-RHF/UHF ones do not. The basis sets used were DKH3-Gen-TK/NOSec-V-TZP [38,39], whose contraction coefficients were optimized with the DKH3 Hamiltonian. The SCF calculations started from the diagonalization of the bare nucleus Hamiltonian and the superposition of the atomic densities guess [40] for atomic and molecular systems, respectively. SCF convergence criteria are the total energy difference of less than 10^{-9} a.u. and a maximum absolute difference of the density matrix elements of 10^{-5} a.u. from the previous iteration.

Numerical tests were performed for four types of benchmark systems, i.e., neutral atomic systems from He to Lr, $W(CO)_6$, Cr_3, and UF_4, to investigate the convergence behaviors of the different acceleration techniques. The geometry of the octahedral $W(CO)_6$ complex was taken from Ref. [41], where $R_{W-C} = 2.06$ Å and $R_{C-O} = 1.17$ Å. The bond lengths of the equilateral triangle Cr_3 and tetrahedral UF_4 were 2.89 and 2.00 Å, respectively [28,31]. The neutral atomic systems were selected as a test set with various

electron configurations from singlet to nonet and with several magnitudes of relativistic effects. The $W(CO)_6$ complex was chosen as a simple example of a heavy-element system whose SCF convergence is well-behaved. The Cr_3 molecule was selected as an example of a non-collinear spin system. Finally, UF_4 was chosen as an example of a system for which SCF convergence is difficult to achieve both in the NR and relativistic frameworks.

3.3.2 Atomic systems from He to Lr

This subsection discusses the SCF convergence behaviors for the atomic systems from He to Lr. The number of cycles required to converge the SCF procedures are summarized for s- and p-block elements in Table 3.1, d-block elements in Table 3.2, and f-block elements in Table 3.3. If the calculations did not converge within 1000 cycles, N.C. is given instead of the number of cycles in the tables. Atomic numbers (Z) and spin multiplicities for the SF calculations ($2S+1$) are also shown. The five algorithms, i.e., FP, damping, DIIS, EDIIS, and EDIIS+DIIS, were used for the SD-GHF calculations as well as SF-RHF/UHF ones.

For the s- and p-block elements listed in Table 3.1, most SF calculations converged; however, convergence with the FP algorithm was not achieved for Ga, Ge, and As. For systems that did converge with the FP algorithm, the number of SCF cycles required ranged from 7 to 32. In contrast, the damping algorithm required more SCF cycles than FP, but all the calculations using damping converged. In most cases, in terms of the number of cycles, EDIIS was the algorithm most similar to FP. This is because the local search ability of EDIIS is similar to that of FP, although the global search ability is higher in EDIIS. DIIS and EDIIS+DIIS both achieved convergence in the least number of cycles. These results indicate that the local search ability is important for efficient SF calculations

in these systems. In the case of the SD calculations, the situation is slightly different from the SF calculations. In FP, several elements required more cycles to achieve convergence: five elements did not converge and 11 elements required more than 100 cycles. In the damping algorithm, the trend is similar to the above one in FP, although the algorithm required more cycles than FP for most elements. In the DIIS-based algorithms (DIIS, EDIIS, and EDIIS+DIIS), closed-shell elements with singlet spin, alkaline metals with doublet spin, and carbon group elements with triplet spin except Si required the similar number of iterations to those of the SF calculations. In contrast, elements with doublet spin states, such as halogens, some triplet spin elements, and quartet spin elements required more cycles compared with the SF calculations.

For the d-block elements listed in Table 3.2, more cycles were required in comparison with the s- and p-block elements. Furthermore, most SF and SD calculations using FP did not converge. At the SF level, DIIS and EDIIS+DIIS required the least number of cycles, as was the case with the s- and p-block elements. At the SD level, EDIIS+DIIS achieved convergence in all cases except Ru. Let us compare the unfavorable convergence behavior of Ru in comparison with Fe and Os in the group 8. The electronic configurations of Ru, Fe, and Os in the ground states are $[Kr](4d)^7(5s)^1$, $[Ar](3d)^6(4s)^2$, and $[Xe](4f)^{14}(5d)^6(6s)^2$, respectively. Thus, in the SCF iterations of the SD-GHF calculations for Ru, electronic fluctuation between 4d- and 5s-orbitals might happen, whereas those for Fe and Os might not.

DIIS required less cycles than EDIIS+DIIS in 10 elements including some triplet and quartet spin systems: Sc, Ti, V, Ni, Zn, Zr, Lu, Hf, Ta, and Pt. This behavior may be caused by the feature of DIIS, which is efficient when starting with a good initial guess.

In general, the singlet elements demonstrated a good convergence behavior. In

addition, Cr, Mn, Mo, Tc, and Re, which have completely singly-occupied d-orbitals, i.e., d^5s^1 or d^5s^2, and correspond to sextet or septet systems, showed a reasonable convergence behavior. For these elements, the electronic fluctuation among the d-orbitals is expected to be small, which is the origin of less SCF cycles. The rest elements possess both singly- and doubly-occupied (unoccupied) d-orbitals, corresponding to the doublet, triplet, quintet, and quartet states. Since the d-electron fluctuation might occur, the SCF convergence became comparatively slow for these elements.

For the f-block elements listed in Table 3.3, the convergence behaviors were worse in comparison with elements from other blocks. At the SF level, SCF convergence was not achieved using FP, except for Th. In the SF calculations, the SCF calculations for 16 elements failed to converge when using damping, eight for DIIS, five for EDIIS, and one for EDIIS+DIIS. In the SD calculations, the numbers of systems that did not converge were 18 for damping, 11 for DIIS, six for EDIIS, and seven for EDIIS+DIIS. In these systems, global search is important. A general trend was not found in terms of the SCF convergence for the f-block elements; the poor convergence behavior of the f-block elements is due to the large SD effects that arise from open-shell electrons in the d- and f-orbitals, which have large angular momenta, from the viewpoint of the *jj*-coupling scheme.

Table 3.4 summarizes the statistical results. #Failure is the sum of the number of elements that failed to converge for each algorithm. The average, minimum, and maximum numbers of iterations for the elements that achieved convergence by each method are shown relative to the EDIIS+DIIS values. They are represented as %Average, %Best, and %Worst, respectively. For example, the %Average for FP is calculated as

$$\%\mathrm{Average}(\mathrm{FP}) = \frac{\#\mathrm{Average}(\mathrm{FP}) - \#\mathrm{Average}(\mathrm{EDIIS{+}DIIS})}{\#\mathrm{Average}(\mathrm{EDIIS{+}DIIS})} \times 100\,, \tag{3.11}$$

where $\mathrm{Average}(\mathrm{X})$ denotes the average number of iterations using algorithm X.

For every algorithm, #Failure was lowest for s/p- and highest for f-block elements. Furthermore, the SD calculations had a higher rate of failure (higher #Failure) than the corresponding SF calculations. In most cases, #Failure decreased in the order of FP, damping, DIIS, EDIIS, and EDIIS+DIIS, as listed in the table. Taking into account the calculated values of %Average, %Best, and %Worst, in most cases, FP and damping required more cycles than the DIIS-related algorithms. For the DIIS-related algorithms, EDIIS required the most cycles. The performance of DIIS was comparatively similar to that of EDIIS+DIIS. In conclusion, EDIIS+DIIS stably achieves SCF convergence with fewer cycles for both SD and SF relativistic calculations.

Table 3.1. Number of cycles required for SCF convergence in s- and p-block neutral atomic systems at the SF- and SD-IODKH/NR levels using the FP, damping, DIIS, EDIIS, and EDIIS+DIIS algorithms.

Element	Z	$2S$+1	SF-IODKH/NR					SD-IODKH/NR				
			FP	Damping	DIIS	EDIIS	EDIIS+DIIS	FP	Damping	DIIS	EDIIS	EDIIS+DIIS
Period 1												
He	2	1	7	63	6	7	6	7	63	6	7	6
Period 2												
Li	3	2	17	69	9	17	9	17	69	10	17	10
Be	4	1	10	70	7	10	7	9	70	7	9	7
B	5	2	17	72	10	17	10	244	848	28	244	58
C	6	3	14	76	10	13	10	333	N.C.	25	300	24
N	7	4	14	77	10	14	10	77	284	25	93	174
O	8	3	14	80	10	14	11	266	888	22	266	27
F	9	2	17	80	11	16	12	17	80	11	16	12
Ne	10	1	22	79	10	19	12	22	79	13	19	13
Period 3												
Na	11	2	20	80	13	19	13	19	80	17	18	13
Mg	12	1	15	81	11	14	11	15	81	15	14	12
Al	13	2	19	83	11	18	11	142	494	25	142	23
Si	14	3	14	79	11	14	11	11	78	10	11	10
P	15	4	15	79	10	14	10	109	397	141	133	127
S	16	3	16	81	11	16	11	267	892	33	269	32
Cl	17	2	15	81	11	15	12	338	N.C.	181	307	205
Ar	18	1	14	81	9	13	10	13	81	11	13	11
Period 4												
K	19	2	19	83	14	21	13	19	82	75	20	14
Ca	20	1	18	82	12	19	12	18	82	108	17	15
Ga	31	2	N.C.	83	14	20	12	N.C.	480	23	139	20
Ge	32	3	N.C.	81	12	19	13	N.C.	81	19	19	14
As	33	4	N.C.	82	12	18	12	N.C.	314	52	94	101
Se	34	3	25	83	13	18	13	N.C.	N.C.	221	N.C.	159
Br	35	2	22	84	12	18	13	285	N.C.	86	538	34

* N.C. means no convergence in 1000 cycles.

Table 3.1. *(Continued.)*

Element	Z	$2S+1$	SF-IODKH/NR					SD-IODKH/NR				
			FP	Damping	DIIS	EDIIS	EDIIS+DIIS	FP	Damping	DIIS	EDIIS	EDIIS+DIIS
Period 4												
Kr	36	1	21	84	11	18	12	20	84	16	17	14
Period 5												
Rb	37	2	25	95	14	22	15	24	96	52	22	17
Sr	38	1	18	90	12	18	14	18	101	58	23	19
In	49	2	21	84	13	20	13	89	321	19	93	18
Sn	50	3	19	83	12	18	13	18	82	14	16	12
Sb	51	4	19	83	12	17	12	79	304	25	80	25
Te	52	3	19	83	12	18	13	N.C.	N.C.	26	606	29
I	53	2	18	84	12	17	13	386	N.C.	45	254	41
Xe	54	1	19	84	10	17	11	18	84	11	17	13
Period 6												
Cs	55	2	23	87	14	22	14	25	84	15	20	14
Ba	56	1	19	85	16	24	15	18	85	430	33	22
Tl	81	2	32	87	13	22	15	58	157	19	54	18
Pb	82	3	26	88	13	20	14	36	88	18	33	17
Bi	83	4	24	88	13	20	14	78	312	36	93	217
Po	84	3	23	88	13	20	14	927	N.C.	31	N.C.	43
At	85	2	23	89	12	20	14	305	921	113	314	43
Rn	86	1	23	89	11	20	14	22	89	13	19	15
Period 7												
Fr	87	2	28	104	15	24	16	26	152	96	23	17
Ra	88	1	20	97	14	19	15	20	117	19	18	16

* N.C. means no convergence in 1000 cycles.

Table 3.2. Number of cycles required for SCF convergence in d-block neutral atomic systems at the SF- and SD-IODKH/NR levels using the FP, damping, DIIS, EDIIS, and EDIIS+DIIS algorithms.

Element	Z	$2S$+1	SF-IODKH/NR					SD-IODKH/NR				
			FP	Damping	DIIS	EDIIS	EDIIS+DIIS	FP	Damping	DIIS	EDIIS	EDIIS+DIIS
Period 4												
Sc	21	2	N.C.	N.C.	24	283	25	N.C.	N.C.	195	N.C.	605
Ti	22	3	N.C.	N.C.	26	125	26	N.C.	N.C.	14	786	192
V	23	4	N.C.	281	21	121	27	N.C.	N.C.	44	838	476
Cr	24	7	N.C.	81	13	22	13	N.C.	584	304	N.C.	38
Mn	25	6	N.C.	82	15	22	13	N.C.	268	N.C.	55	22
Fe	26	5	N.C.	88	42	22	14	N.C.	N.C.	639	27	114
Co	27	4	N.C.	218	23	111	24	N.C.	N.C.	N.C.	856	447
Ni	28	3	N.C.	92	15	35	16	N.C.	N.C.	28	N.C.	464
Cu	29	2	N.C.	87	15	51	17	N.C.	87	19	27	16
Zn	30	1	N.C.	84	12	20	12	N.C.	84	16	19	25
Period 5												
Y	39	2	219	710	24	221	30	518	N.C.	885	470	195
Zr	40	3	198	478	29	155	24	N.C.	N.C.	32	N.C.	49
Nb	41	6	61	79	17	22	14	878	N.C.	N.C.	N.C.	247
Mo	42	7	24	80	11	19	12	166	729	N.C.	185	34
Tc	43	6	809	148	26	39	14	N.C.	223	N.C.	66	50
Ru	44	5	99	163	19	189	60	N.C.	N.C.	585	389	N.C.
Rh	45	4	N.C.	358	25	108	26	N.C.	N.C.	470	N.C.	142
Pd	46	1	N.C.	159	13	41	13	N.C.	284	17	39	16
Ag	47	2	N.C.	112	14	25	14	N.C.	242	16	24	15
Cd	48	1	N.C.	84	12	22	13	N.C.	84	15	21	14
Period 6												
Lu	71	2	N.C.	469	21	42	19	N.C.	959	40	347	555
Hf	72	3	N.C.	587	27	168	29	N.C.	N.C.	82	608	447
Ta	73	4	N.C.	288	33	151	38	N.C.	N.C.	78	296	841
W	74	5	N.C.	446	20	80	28	N.C.	110	31	226	21
Re	75	6	N.C.	213	30	22	15	N.C.	261	27	57	26
Os	76	5	N.C.	226	24	43	16	N.C.	884	560	179	290

* N.C. means no convergence in 1000 cycles.

Table 3.2. *(Continued.)*

Element	*Z*	2*S*+1	SF-IODKH/NR					SD-IODKH/NR				
			FP	Damping	DIIS	EDIIS	EDIIS+DIIS	FP	Damping	DIIS	EDIIS	EDIIS+DIIS
Period 6												
Ir	77	4	N.C.	367	43	144	24	N.C.	N.C.	N.C.	689	239
Pt	78	3	N.C.	409	28	124	22	N.C.	N.C.	25	984	628
Au	79	2	N.C.	94	14	46	18	N.C.	89	19	33	18
Hg	80	1	N.C.	88	12	21	13	N.C.	87	16	20	14
Period 7												
Lr	103	2	N.C.	516	56	175	26	N.C.	266	201	111	37

* N.C. means no convergence in 1000 cycles.

Table 3.3. Number of cycles required for SCF convergence in f-block neutral atomic systems at the SF- and SD-IODKH/NR levels using the FP, damping, DIIS, EDIIS, and EDIIS+DIIS algorithms.

Element	Z	$2S$+1	SF-IODKH/NR					SD-IODKH/NR				
			FP	Damping	DIIS	EDIIS	EDIIS+DIIS	FP	Damping	DIIS	EDIIS	EDIIS+DIIS
Period 6												
La	57	2	N.C.	733	N.C.	177	33	N.C.	N.C.	275	437	N.C.
Ce	58	1	N.C.	262	30	N.C.	26	N.C.	N.C.	N.C.	N.C.	338
Pr	59	4	N.C.	N.C.	157	430	61	N.C.	N.C.	801	N.C.	221
Nd	60	5	N.C.	N.C.	110	438	161	N.C.	N.C.	N.C.	N.C.	N.C.
Pm	61	6	N.C.	N.C.	47	679	64	N.C.	515	286	N.C.	227
Sm	62	7	N.C.	N.C.	71	685	31	N.C.	951	486	258	33
Eu	63	8	N.C.	223	132	74	29	N.C.	257	N.C.	95	48
Gd	64	9	N.C.	819	29	203	31	N.C.	N.C.	711	890	N.C.
Tb	65	6	N.C.	688	33	N.C.	N.C.	N.C.	878	366	334	58
Dy	66	5	N.C.	N.C.	N.C.	304	464	N.C.	N.C.	488	N.C.	123
Ho	67	4	N.C.	N.C.	69	387	104	N.C.	204	554	94	28
Er	68	3	N.C.	N.C.	N.C.	291	34	N.C.	N.C.	N.C.	813	N.C.
Tm	69	2	N.C.	N.C.	N.C.	467	35	N.C.	N.C.	699	948	478
Yb	70	1	N.C.	94	20	30	17	N.C.	108	N.C.	32	28
Period 7												
Ac	89	2	N.C.	907	23	72	25	N.C.	N.C.	149	155	43
Th	90	3	348	191	32	240	42	N.C.	N.C.	32	N.C.	35
Pa	91	4	N.C.	N.C.	N.C.	892	124	N.C.	N.C.	N.C.	937	N.C.
U	92	5	N.C.	N.C.	N.C.	N.C.	470	N.C.	N.C.	N.C.	423	70
Np	93	6	N.C.	N.C.	82	N.C.	407	N.C.	N.C.	54	380	N.C.
Pu	94	7	N.C.	N.C.	30	465	36	N.C.	N.C.	35	292	N.C.
Am	95	8	N.C.	269	27	805	579	N.C.	305	368	93	55
Cm	96	9	N.C.	726	24	150	41	N.C.	816	458	204	429
Bk	97	6	N.C.	N.C.	51	N.C.	75	N.C.	580	N.C.	268	180
Cf	98	5	N.C.	N.C.	N.C.	245	557	N.C.	N.C.	N.C.	884	468
Es	99	4	N.C.	N.C.	N.C.	107	24	N.C.	N.C.	309	888	595
Fm	100	3	N.C.	N.C.	22	50	20	N.C.	N.C.	434	642	498
Md	101	2	N.C.	153	23	548	34	N.C.	N.C.	N.C.	101	39
No	102	1	N.C.	94	18	35	16	N.C.	165	N.C.	94	61

* N.C. means no convergence in 1000 cycles.

Table 3.4. Summary of the SCF convergence behaviors in s/p-, d-, and f-block neutral atomic systems at the SF- and SD-IODKH/NR levels using the FP, damping, DIIS, EDIIS, and EDIIS+DIIS algorithms.

System	Characteristic	SF-IODKH/NR					SD-IODKH/NR				
		FP	Damping	DIIS	EDIIS	EDIIS+DIIS	FP	Damping	DIIS	EDIIS	EDIIS+DIIS
s/p-block	#Failure	3	0	0	0	0	5	7	0	2	0
elements	%Average	56.4	578.3	4.6	44.6	—	187.3	493.4	28.2	169.0	—
	%Best	16.7	950.0	0.0	16.7	—	16.7	950.0	0.0	16.7	—
	%Worst	100.0	550.0	0.0	50.0	—	327.2	324.4	98.2	179.3	—
d-block	#Failure	25	2	0	0	0	28	15	6	6	1
elements	%Average	1012.2	1056.6	7.5	307.5	—	148.8	56.6	−16.7	40.6	—
	%Best	100.0	558.3	−8.3	58.3	—	1085.7	500.0	0.0	35.7	—
	%Worst	1248.3	1083.3	−6.7	371.7	—	4.4	14.0	5.2	17.0	—
f-block	#Failure	27	16	8	5	1	28	18	11	6	7
elements	%Average	165.4	227.9	−60.7	157.8	—	—	147.5	98.2	118.0	—
	%Best	2075.0	487.5	12.5	87.5	—	—	285.7	14.3	14.3	—
	%Worst	−39.9	56.6	−72.9	54.1	—	—	59.8	34.6	59.3	—

* #Failure represents the number of elements which failed the SCF convergence within 1000 cycles.

** %X means the ratio of X to EDIIS+DIIS, i.e., %X = (X − X(EDIIS+DIIS)) / X(EDIIS+DIIS) × 100%.

3.3.3 A well-behaved system: $W(CO)_6$

This subsection discusses the SCF convergence behavior of the $W(CO)_6$ complex. The complex was selected as an example of a simple heavy-element system whose convergence is well-behaved. This is true because $W(CO)_6$ has a completely closed-shell configuration, even in SD calculations. Figure 3.1 shows the SCF convergence behaviors in GHF for the $W(CO)_6$ complex using FP and the four acceleration techniques: damping, DIIS, EDIIS, and EDIIS+DIIS. The SF result using EDIIS+DIIS is also shown for comparison. The vertical and horizontal axes show the absolute energy difference between the successive iterations on a logarithmic scale and the iteration number, respectively. With all algorithms except FP, SCF convergence was achieved. These methods converged to the same total energy (E = −16809.23228 a.u.). DIIS and EDIIS+DIIS were the fastest algorithms, converging in the same number of iterations, i.e., 19 cycles. In contrast, EDIIS and damping required more cycles; 39 cycles for EDIIS and 79 cycles for damping. These indicate that the initial guess was a good approximate solution for the simple and typical electronic structure of $W(CO)_6$. Thus, the local search performance mainly determines the rate of convergence here. The difference in the number of iterations between the SF and SD calculations was small: 14 cycles for EDIIS+DIIS at the SF level. The well-behaved nature of the SCF convergence of $W(CO)_6$ is due to its typical closed-shell character and small contributions of SD effects to SCF convergence.

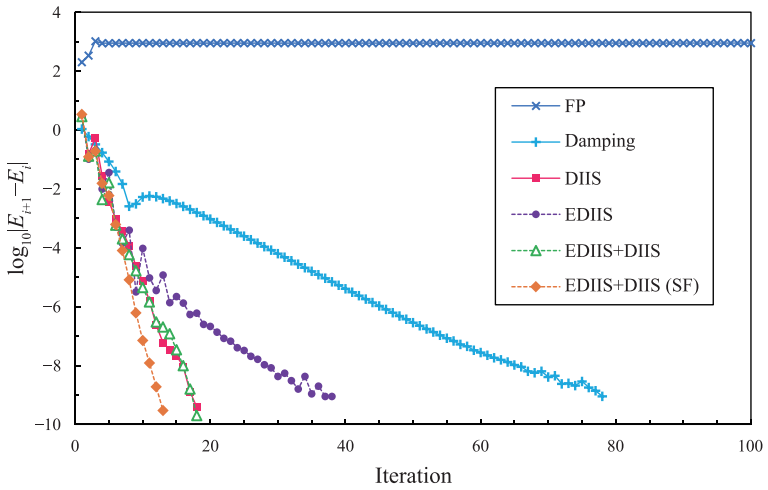

Figure 3.1. SCF convergence behavior in GHF calculations for $W(CO)_6$ with FP, damping, DIIS, EDIIS, and EDIIS+DIIS. The SF result using EDIIS+DIIS is also shown. The converged energy determined in the SD calculation was −16809.23228 a.u.

3.3.1 A non-collinear system: Cr_3

This subsection discusses the SCF convergence behavior of the Cr_3 molecule. Cr_3 is an example of a non-collinear spin system. In non-collinear systems such as the open-shell triangular Cr_3 complex, the stable spin structure is isotropic with respect to the molecular plane due to geometrical frustration. To describe the stable spin structure of the non-collinear system, GHF, which freely rotates each spin-quantized axis, is required. An SF-UHF calculation was also performed for comparison of the SCF convergence behavior. Figure 3.2 shows the SCF convergence results obtained from the GHF calculations for the non-collinear Cr_3 system using the four acceleration techniques and the FP algorithm as well as the result of an SF calculation. Only the EDIIS+DIIS algorithm achieved SCF convergence within 1000 cycles. The converged total energy obtained using EDIIS+DIIS in GHF was −3148.60769 a.u. Using FP led to large energy differences, which are due to the oscillation between two states. In damping and DIIS, the energy differences decreased slowly, although they failed to converge within 1000 cycles. In EDIIS, the energy

differences also decreased slowly in both early and late iterations, as shown in Figure 3.2. However, in the middle iteration region, the differences increased. This result indicates that local searching is important in achieving convergence for this system. The difference between SF and SD calculations was larger than that of $W(CO)_6$ because the electronic structure obtained by GHF is more complicated, arising from the geometrical non-collinearity in Cr_3. In conclusion, the EDIIS+DIIS approach is effective for non-collinear spin systems.

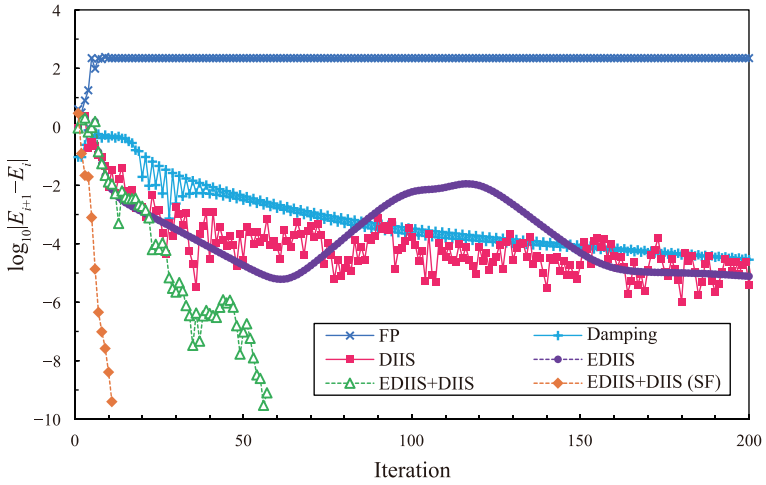

Figure 3.2. SCF convergence behavior in GHF calculations for Cr_3 with FP, damping, DIIS, EDIIS, and EDIIS+DIIS. The SF result using EDIIS+DIIS is also shown. The converged energy determined in the SD calculation was −3148.60769 a.u.

3.3.4 A challenging system: UF_4

This subsection describes the SCF convergence behavior in UF_4, which is a representative challenging case. This system has been used as a challenging example in previous studies investigating convergence acceleration techniques [31,35,36]. Figure 3.3 shows the convergence behaviors in the GHF calculations for the UF_4 molecule using the FP algorithm and the four acceleration techniques as well as the SF result. In this system,

when DIIS and EDIIS+DIIS were used, the SCF calculations converged within 1000 cycles. EDIIS+DIIS converged twice as fast as DIIS, although EDIIS+DIIS required 334 iterations to achieve convergence. This result indicates that SCF convergence is challenging in SD calculations of UF_4. The converged total energy was −28380.18867 a.u. for EDIIS+DIIS and −28380.18851 a.u. for DIIS. This means that these two calculations converged to different SCF solutions with each other. From the analysis of the converged density matrices, the major differences were observed for 5f-orbitals of the uranium atom, reflecting their various microstates. Damping and EDIIS slowly but monotonically decreased the energy errors, which steadily approached the values obtained by EDIIS+DIIS/DIIS. The difference between the number of iterations required by SF and SD calculations was approximately 200. This result indicates that SO interactions contribute significantly to the electronic structure of UF_4. Thus, the SCF convergence for UF_4 is more difficult at SD than SF level. However, EDIIS+DIIS was an effective algorithm for this challenging system.

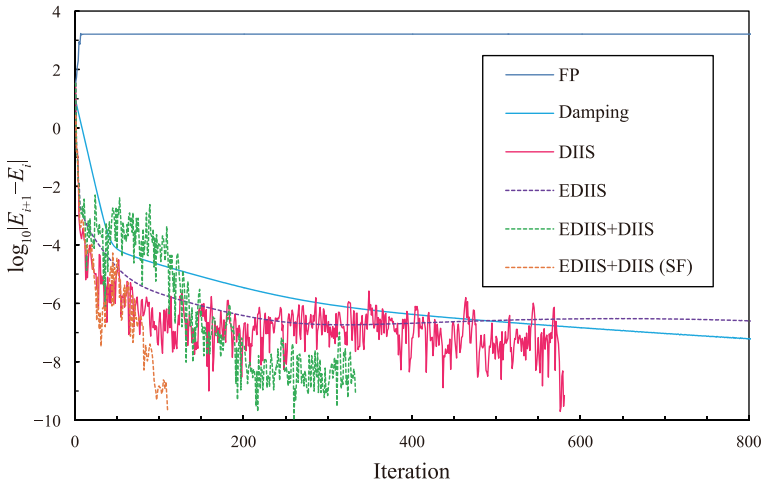

Figure 3.3. SCF convergence behavior in GHF calculations for UF_4 with FP, damping, DIIS, EDIIS, and EDIIS+DIIS. The SF result using EDIIS+DIIS is also shown. The converged energy determined in the SD calculation was −28380.18867 a.u.

In summary, the EDIIS+DIIS algorithm is applicable for many cases: typical and simple systems, non-collinear systems, which require GHF treatment to describe the geometrically frustrated spin structure, and challenging systems, which require GHF treatment with SD effects.

3.4 Conclusion

In this chapter, the author has assessed the FP algorithm and four SCF acceleration algorithms including the damping, DIIS, EDIIS, and EDIIS+DIIS algorithms in the complex GHF framework both with SF and SD relativistic effects. Here, IODKH/NR was used as a many-electron Hamiltonian. The benchmark systems adopted were atoms from He to Lr, the $W(CO)_6$ complex as an example of a well-behaved system, Cr_3 as a non-collinear spin system, and UF_4 as a challenging system. The numerical assessments revealed that the EDIIS+DIIS algorithm provides fast and stable SCF convergence in the GHF framework in comparison with the other algorithms.

References

[1] K. G. Dyall, K. Faegri, Introduction to Relativistic Quantum Chemistry, Oxford University Press, New York, 2007.

[2] P. Schwerdtfeger, Relativistic Electronic Structure Theory, Part 2. Applications, Elsevier Science, Amsterdam, 2004.

[3] R. E. Moss, Advanced Molecular Quantum Mechanics: An Introduction to Relativistic Quantum Mechanics and the Quantum Theory of Radiation, Chapman and Hall, London, 1973.

[4] L. L. Foldy, S. A. Wouthuysen, *Phys. Rev.* **78**, 29 (1950).

[5] M. Douglas, N. M. Kroll, *Ann. Phys. (Leipzig)* **82**, 89 (1974).

[6] B. A. Hess, *Phys. Rev. A* **32**, 756 (1985).

[7] E. van Lenthe, E. J. Baerends, J. G. Snijders, *J. Chem. Phys.* **99**, 4597 (1993).

[8] S. Faas, J. G. Snijders, J. H. van Lenthe, E. van Lenthe, E. J. Baerends, *Chem. Phys. Lett.* **246**, 632 (1995).

[9] R. Samzow, B. A. Hess, G. Jansen, *J. Chem. Phys.* **96**, 1227 (1992).

[10] K. G. Dyall, *J. Chem. Phys.* **106**, 9618 (1997).

[11] T. Nakajima, K. Hirao, *J. Chem. Phys.* **113**, 7786 (2000).

[12] A. Wolf, M. Reiher, B. A. Hess, *J. Chem. Phys.* **117**, 9215 (2002).

[13] M. Barysz, A. J. Sadlej, *J. Chem. Phys.* **116**, 2696 (2002).

[14] C. van Wüllen, C. Michauk, *J. Chem. Phys.* **123**, 204113 (2005).

[15] D. Peng, W. Liu, Y. Xiao, L. Cheng, *J. Chem. Phys.* **127**, 104106 (2007).

[16] J. Sikkema, L. Visscher, T. Saue, M. Iliaš, *J. Chem. Phys.* **131**, 124116 (2009).

[17] W. Liu, *Mol. Phys.* **108**, 1679 (2010).

[18] R. Seeger, J. A. Pople, *J. Chem. Phys.* **66**, 3045 (1977).

[19] H. Fukutome, *Int. J. Quantum Chem.* **20**, 955 (1981).

[20] J.-L. Calais, *Adv. Quantum Chem.* **17**, 225 (1985).

[21] R. McWeeny, Methods of Molecular Quantum Mechanics, Academic Press, London, 1989.

[22] P.-O. Löwdin, I. Mayer, *Adv. Quantum Chem.* **24**, 79 (1992).

[23] S. Hammes-Schiffer, H. C. Andersen, *J. Chem. Phys.* **99**, 1901 (1993).

[24] S. K. Wolff, D. Jayatilaka, G. S. Chandler, *J. Chem. Phys.* **103**, 4562 (1995).

[25] D. Jayatilaka, *J. Chem. Phys.* **108**, 7587 (1998).

[26] J. L. Stuber, J. Paldus, in: E. J. Brändas, E. S. Kryachko (Eds.), Fundamental World of Quantum Chemistry, Kluwer Academic Publishers, Dordrecht, 2003, p. 67.

[27] M. K. Armbruster, F. Weigend, C. van Wüllen, W. Klopper, *Phys. Chem. Chem. Phys.* **10**, 1748 (2008).

[28] J. J. Goings, F. Ding, M. J. Frisch, X. Li, *J. Chem. Phys.* **142**, 154109 (2015).

[29] P. Pulay, *Chem. Phys. Lett.* **73**, 393 (1980).

[30] P. Pulay, *J. Comput. Chem.* **3**, 556 (1982).

[31] K. N. Kudin, G. E. Scuseria, E. Cancès, *J. Chem. Phys.* **116**, 8255 (2002).

[32] X. Hu, W. Yang, *J. Chem. Phys.* **132**, 054109 (2010).

[33] Y. A. Wang, C. Y. Yam, Y. K. Chen, G. Chen, *J. Chem. Phys.* **134**, 241103 (2011).

[34] Y. K. Chen, Y. A. Wang, *J. Chem. Theory Comput.* **7**, 3045 (2011).

[35] D. Sulzer, S. Iuchi, K. Yasuda, *Chem. Phys. Lett.* **635**, 201 (2015).

[36] A. J. Garza, G. E. Scuseria, *J. Chem. Phys.* **137**, 054110 (2012).

[37] D. G. Luenberger, Y. Ye, Linear and Nonlinear Programming, Springer, New York, 2008.

[38] T. Koga, H. Tatewaki, T. Shimazaki, *Chem. Phys. Lett.* **328**, 473 (2000).

[39] Y. Osanai, T. Noro, E. Miyoshi, M. Sekiya, T. Koga, *J. Chem. Phys.* **120**, 6408 (2004).

[40] J. H. van Lenthe, R. Zwaans, H. J. J. van Dam, M. F. Guest, *J. Comput. Chem.* **27**, 926 (2006).

[41] K. Liu, C. G. Ning, Z. H. Luo, L. L. Shi, J. K. Deng, *Chem. Phys. Lett.* **497**, 229 (2010).

Chapter 4

Spin-dependent relativistic open-shell Hartree–Fock theory using time-reversal symmetry: The unrestricted approach

4.1 Introduction

Relativistic effects play an important role in the chemical and physical properties of heavy-element compounds. These effects are classified into SF and SD effects. The SF effects, which include the mass-velocity and Darwin interactions, mainly contribute to orbital contraction and expansion. The SD effects, including the SO and other magnetic interactions, induce energy level splitting. For an accurate description of these effects, two- and four-component relativistic theories [1-15] are required instead of NR theory, and these theories give accurate results for arbitrary elements in the periodic table because the relativistic effects are considered in an SCF manner.

At the HF level of theory, solutions are classified by the preserved symmetries: square and *z*-component of spin symmetry (S^2 and S_z), time-reversal symmetry K , and complex conjugation symmetry K_0 [16,17]. For example, RHF and ROHF solutions possess S^2 , S_z , K , and K_0 symmetries, while a UHF solution has S_z and K_0 symmetries. Because an SF Hamiltonian is commutable with the spin operators and spin is a good quantum number, these methods are applicable to SF calculations. In SD calculations, on the other hand, the Hamiltonian explicitly includes the spin operators and complex terms, and it is not invariant for the above symmetry operations. Thus, these

symmetries must be relaxed.

One scheme for SD calculations is the GHF method [16-25], which does not include any symmetry constraints. In GHF, the additional spin degrees of freedom allow the coupling of alpha and beta spins and free rotation about each spin-quantized axis. Furthermore, GHF can be used both in closed- and open-shell systems. However, the additional degrees of freedom result in local minima and non-convergence problems in the SCF part of the calculation. One solution to the local minima problem is the use of the second-order orbital optimization scheme, which has been extended to GHF by Goings et al. [26]. A solution for the non-convergence problem is the use of SCF acceleration techniques. Recently, the author has shown that a combination of Pulay's DIIS [27,28] and EDIIS [29] succeeds in improving the GHF convergence behavior for heavy-element systems, although systems with high spin multiplicities, e.g., d- and f-block elements, still require a large number of iterations [30].

The other representative scheme for the SD calculations is the KRHF method [31-34], which preserves only time-reversal symmetry. The time-reversal invariance works as a generalization of spin restriction and induces two-fold degeneracy for spinors. Therefore, KRHF is regarded as the relativistic counterpart of RHF. However, KRHF can only be applied to closed-shell systems.

For open-shell systems, a HF method for the SD relativistic calculations, which is termed the moment polarization scheme or KUHF, was discussed in several groups [35-37]. In this chapter, the fundamental characteristics of KUHF are examined. The present KUHF scheme is reformulated on the basis that the computational procedure for KRHF is similar to that of RHF, using quaternion algebra. It should be noted that KUHF here is distinct from GHF, although GHF is sometimes also called KUHF [38,39].

This chapter is organized as follows: Section 4.2 presents theoretical aspects of KUHF. Numerical assessments performed are discussed in Sec. 4.3. Finally, concluding remarks are given in Sec. 4.4.

4.2 Theory

4.2.1 Relationship between RHF and KRHF methods

This subsection compares a relationship between RHF and KRHF in terms of their algorithms. Figure 4.1 illustrates the comparison. Here, mono- and four-layered squares represent the real and quaternion matrices, respectively. In RHF, the Fock matrix $\mathbf{F}$ is first calculated. Then, $\mathbf{F}$ is diagonalized to give the MO coefficients $\mathbf{C}$ as eigenvectors. In addition, the square of $\mathbf{C}$ gives the density matrix $\mathbf{D}$. This procedure is repeated until the values of total energy and/or matrix elements converge. Here, all the matrices including $\mathbf{F}$, $\mathbf{C}$, and $\mathbf{D}$ are defined in real space. The computational procedure of KRHF is similar to that of RHF. The difference is that the matrices in KRHF are defined in quaternionic space rather than real space. From the computational point of view, KRHF is therefore regarded as a quaternionic counterpart to RHF.

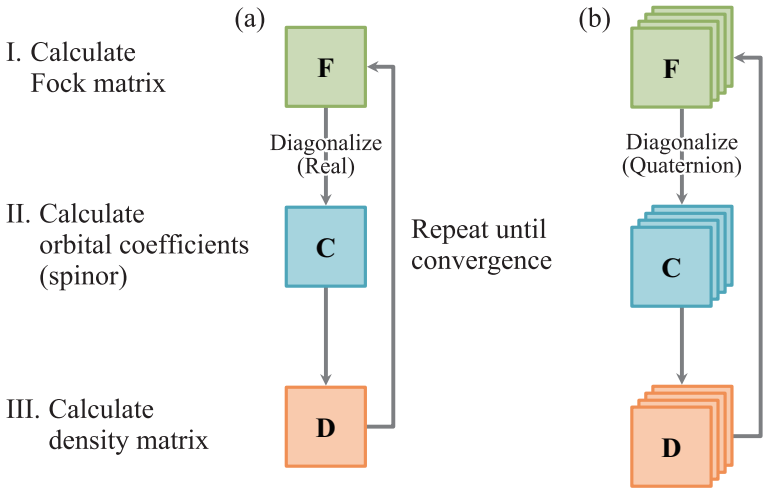

Figure 4.1. Schematic of (a) RHF and (b) KRHF procedures. The mono- and four-layered square represents real and quaternionic matrices, respectively.

4.2.2 KUHF method

This subsection presents the formulation of KUHF with the same strategy as shown in Figure 4.1 for KRHF. Namely, the present KUHF method is defined as a quaternionic counterpart of UHF; this idea is summarized in Figure 4.2. In UHF, similar procedures to those of RHF calculations are performed independently for alpha and beta spins, as shown in Figure 4.2(a). Both spins are coupled in the evaluation of the Fock matrices. In KUHF, a similar algorithm as that used in UHF is applied using quaternion algebra shown in Figure 4.2(b). Because the two-component framework allows the hybridization of alpha and beta spins, one interprets that a linear combination of alpha and beta spin bases give new rotated spin bases, σ and $\bar{\sigma}$, in KUHF. Here, σ and $\bar{\sigma}$ are termed pseudo-alpha and pseudo-beta spins, respectively. The pseudo-spin pair corresponds to the Kramers pair. The grouping of the spinor pair is still valid, although the pseudo-alpha and pseudo-beta spinors of KUHF are not exactly related by the time-reversal operation. In KUHF, in summary, a UHF-like calculation is performed for pseudo-alpha and pseudo-

beta spin bases in a quaternionic manner.

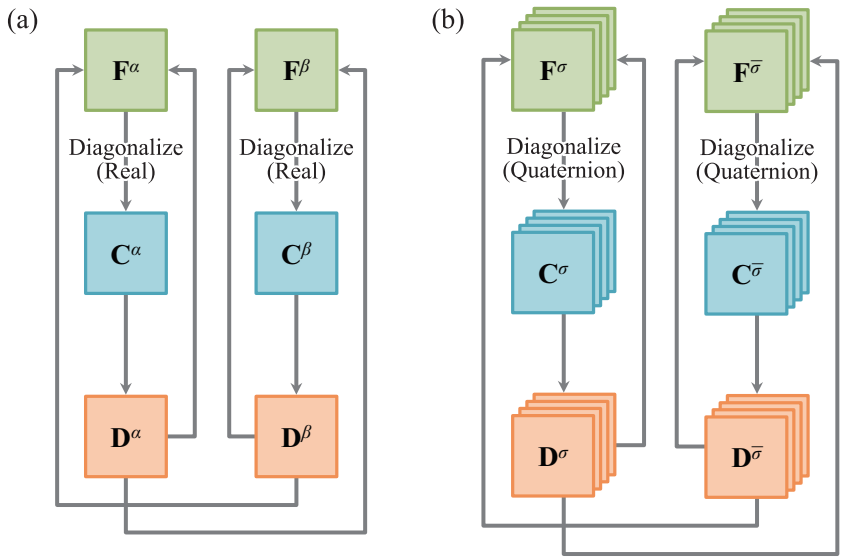

Figure 4.2. Schematic of (a) UHF and (b) KUHF procedures. The mono- and four-layered square represents real and quaternionic matrices, respectively.

According to the algorithm given in Figure 4.2(b), the RH equation of KUHF can be formulated as

$$\begin{cases} {}^{\mathrm{Q}}\mathbf{F}^{\sigma}\,{}^{\mathrm{Q}}\mathbf{C}^{\sigma} = {}^{\mathrm{Q}}\mathbf{S}^{\sigma}\,{}^{\mathrm{Q}}\mathbf{C}^{\sigma}\boldsymbol{\varepsilon}^{\sigma} \\ {}^{\mathrm{Q}}\mathbf{F}^{\bar{\sigma}}\,{}^{\mathrm{Q}}\mathbf{C}^{\bar{\sigma}} = {}^{\mathrm{Q}}\mathbf{S}^{\bar{\sigma}}\,{}^{\mathrm{Q}}\mathbf{C}^{\bar{\sigma}}\boldsymbol{\varepsilon}^{\bar{\sigma}} \end{cases}$$
$$\Leftrightarrow \begin{cases} \left(\mathbf{F}^{\alpha\alpha} + \breve{j}\mathbf{F}^{\alpha\beta}\right)\left(\mathbf{C}^{\alpha} - \breve{j}\mathbf{C}^{\beta *}\right) = \mathbf{S}^{\alpha\alpha}\left(\mathbf{C}^{\alpha} - \breve{j}\mathbf{C}^{\beta *}\right)\boldsymbol{\varepsilon}^{\sigma} \\ \left(\mathbf{F}^{\beta\beta} + \breve{j}\mathbf{F}^{\beta\alpha}\right)\left(\mathbf{C}^{\beta} - \breve{j}\mathbf{C}^{\alpha *}\right) = \mathbf{S}^{\beta\beta}\left(\mathbf{C}^{\beta} - \breve{j}\mathbf{C}^{\alpha *}\right)\boldsymbol{\varepsilon}^{\bar{\sigma}} \end{cases}, \tag{4.1}$$

where

$${}^{\mathrm{Q}}\mathbf{S}^{\sigma} = {}^{\mathrm{Q}}\mathbf{S}^{\bar{\sigma}} = \mathbf{S}^{\alpha\alpha} = \mathbf{S}^{\beta\beta}. \tag{4.2}$$

If the two-electron part of a Hamiltonian g_{ij} consists of only SF terms, the Fock matrix elements are given by

$${}^{\mathrm{Q}}F^{\sigma}_{\mu\nu} = {}^{\mathrm{Q}}h_{\mu\nu} + \sum_{\rho\lambda}^{\{\mathrm{AO}\}}\left[\left({}^{\mathrm{Q}}D^{\sigma}_{\rho\lambda} + {}^{\mathrm{Q}}D^{\bar{\sigma}}_{\rho\lambda}\right)\left(\mu\nu\middle|g_{ij}\middle|\rho\lambda\right) - {}^{\mathrm{Q}}D^{\sigma}_{\rho\lambda}\left(\mu\lambda\middle|g_{ij}\middle|\rho\nu\right)\right] \tag{4.3}$$

$$ {}^{\mathrm{Q}}F^{\bar{\sigma}}_{\mu\nu} = {}^{\mathrm{Q}}h_{\mu\nu} + \sum_{\rho\lambda}^{\{\mathrm{AO}\}} \left[\left({}^{\mathrm{Q}}D^{\bar{\sigma}}_{\rho\lambda} + {}^{\mathrm{Q}}D^{\sigma}_{\rho\lambda} \right) \left(\mu\nu \middle| g_{ij} \middle| \rho\lambda \right) - {}^{\mathrm{Q}}D^{\bar{\sigma}}_{\rho\lambda} \left(\mu\lambda \middle| g_{ij} \middle| \rho\nu \right) \right], \tag{4.4} $$

where h, D, and $\left(\mu\nu \middle| g_{ij} \middle| \rho\lambda \right)$ are the one-electron part of the Fock matrix element, a density matrix element, and a two-electron integral, respectively.

From analogy with KRHF, the MSs of KUHF are given by

$$ {}^{\mathrm{Q}}\varphi^{\sigma}_{i} = \varphi^{\alpha}_{i} - \breve{j}\varphi^{\beta *}_{i} \tag{4.5} $$

$$ {}^{\mathrm{Q}}\varphi^{\bar{\sigma}}_{i} = \varphi^{\beta}_{i} - \breve{j}\varphi^{\alpha *}_{i} . \tag{4.6} $$

The total electronic wavefunction and energy are defined as

$$ \Psi^{\mathrm{KUHF}} = \left\| {}^{\mathrm{Q}}\varphi^{\sigma}_{1} \, {}^{\mathrm{Q}}\varphi^{\sigma}_{2} \cdots {}^{\mathrm{Q}}\varphi^{\sigma}_{N^{\sigma}} \, {}^{\mathrm{Q}}\varphi^{\bar{\sigma}}_{1} \, {}^{\mathrm{Q}}\varphi^{\bar{\sigma}}_{2} \cdots {}^{\mathrm{Q}}\varphi^{\bar{\sigma}}_{N^{\bar{\sigma}}} \right\| \tag{4.7} $$

and

$$ E^{\mathrm{KUHF}} = \frac{1}{2} \mathrm{tr} \left[{}^{\mathrm{Q}}\mathbf{D}^{\sigma} \left({}^{\mathrm{Q}}\mathbf{h} + {}^{\mathrm{Q}}\mathbf{F}^{\sigma} \right) + {}^{\mathrm{Q}}\mathbf{D}^{\bar{\sigma}} \left({}^{\mathrm{Q}}\mathbf{h} + {}^{\mathrm{Q}}\mathbf{F}^{\bar{\sigma}} \right) \right], \tag{4.8} $$

respectively. Here, the number of electrons is given by

$$ N = N^{\sigma} + N^{\bar{\sigma}} , \tag{4.9} $$

where each term is the sum of occupation numbers f for the corresponding pseudo-spin,

$$ N^{\sigma} = \sum_{i} f^{\sigma}_{i} \tag{4.10} $$

$$ N^{\bar{\sigma}} = \sum_{i} f^{\bar{\sigma}}_{i} . \tag{4.11} $$

There is no general scheme to separate the pseudo-alpha and pseudo-beta spinors. Here, to define UHF-like configurations, the occupation numbers for alpha and beta orbitals are adopted as those for pseudo-alpha and pseudo-beta spinors. Thus, the density matrices in KUHF are defined by Eqs. (4.12) and (4.13).

$$ {}^{\mathrm{Q}}\mathbf{D}^{\sigma} = {}^{\mathrm{Q}}\mathbf{C}^{\sigma} \mathbf{f}^{\sigma} \left({}^{\mathrm{Q}}\mathbf{C}^{\sigma} \right)^{\dagger} \approx {}^{\mathrm{Q}}\mathbf{C}^{\sigma} \mathbf{f}^{\alpha} \left({}^{\mathrm{Q}}\mathbf{C}^{\sigma} \right)^{\dagger} \tag{4.12} $$

$$ {}^{Q}\mathbf{D}^{\bar{\sigma}} = {}^{Q}\mathbf{C}^{\bar{\sigma}}\mathbf{f}^{\bar{\sigma}}\left({}^{Q}\mathbf{C}^{\bar{\sigma}}\right)^{\dagger} \approx {}^{Q}\mathbf{C}^{\bar{\sigma}}\mathbf{f}^{\beta}\left({}^{Q}\mathbf{C}^{\bar{\sigma}}\right)^{\dagger} \tag{4.13} $$

When one adopts the UHF occupation numbers corresponding to the singlet configuration in Eqs. (4.12) and (4.13), the configuration is termed pseudo-singlet, and this is the case with other multiplicities. Furthermore, pseudo-singlet, pseudo-doublet, and so forth are collectively termed as pseudo-spin multiplicities.

In the family of broken-symmetry HF methods in the independent particle model, KUHF is classified in the group of TSW and complex GHF (following Fukutome's [16], and Stuber and Paldus' notations [17], respectively) because no symmetry is preserved and because of the matrix structure shown above. Unlike the ordinary GHF framework, however, not all of the spinors are considered independently, and the pseudo-alpha and pseudo-beta spinors correspond to each other, which is similar to the concept of Kramers pairs. From this point of view, KUHF is regarded as TSCW-like TSW or paired-GHF-like complex GHF following the above mentioned notation.

4.3 Numerical assessments

4.3.1 Computational details

This subsection describes the computational details for the numerical assessments. KUHF was implemented into the in-house program. For comparison, several calculations were performed at the RHF, UHF, KRHF, and GHF levels as well. To obtain the symmetry-adapted eigenvectors through diagonalization in KRHF and KUHF, a quaternionic diagonalization algorithm based on the Householder transformation and subsequent QR decomposition was implemented in the program [33,40,41].

For a relativistic Hamiltonian, IODKH/NR [11] was adopted. The SD terms of the IODKH/NR Hamiltonian were considered in the KRHF, KUHF, and GHF calculations

(unless otherwise indicated). The basis sets adopted here were DKH3-Gen-TK/NOSec-V-TZP [42,43].

To assess SCF convergence, several computational options were fixed as follows. The initial guess orbitals were obtained by the diagonalization of the bare nucleus Hamiltonian. A combination algorithm comprising DIIS and EDIIS was extended in a quaternionic manner for use as an SCF acceleration algorithm. The number of dimension of the DIIS subspace was set to 10. SCF convergence was considered to be achieved when the total energy difference and the maximum difference of density matrix elements were less than 10^{-9} hartrees and 10^{-5} a.u., respectively, between successive iterations.

4.3.2 Total and spinor energies

This subsection investigates the characteristics of KUHF from the viewpoint of total and spinor energies in comparison with UHF and GHF. Table 4.1 shows the total energies of coinage metal atoms (Cu, Ag, and Au) in their ground states using the SF- and SD-IODKH/NR Hamiltonians. The energy differences between KUHF and GHF in the SD calculations are also shown as Δ in the table. Here, the doublet and pseudo-doublet configurations are specified in UHF and KUHF, respectively.

In the SF calculations, all the methods, including KUHF, give the same total energy values for each system, indicating that the formulations of UHF, KUHF, and GHF are equivalent in the common SF cases. This is because alpha (or beta) spin does not commonly couple with beta (or alpha) spin without SD effects, and pseudo-alpha (pseudo-beta) spin is thus equivalent to alpha (beta) spin.

In the SD calculations, KUHF yields very close energies to those of GHF. The energy deviations Δ are less than 14 microhartrees, although Δ increases as the element gets

heavier. KUHF commonly gives higher total energy than GHF. This trend is closely related with the so-called Löwdin's dilemma [44] in broken-symmetry studies, i.e., higher symmetry leads to higher energy. Namely, the higher energies in KUHF are due to the partial use of time-reversal symmetry.

Table 4.1. Total energies (in hartrees) of the Cu, Ag, and Au atoms computed by UHF, KUHF, and GHF using the SF- and SD-IODKH/NR Hamiltonians. Δ shows the energy deviations of KUHF from GHF in the SD-IODKH/NR calculations.

System	SF-IODKH/NR			SD-IODKH/NR		
	UHF	KUHF	GHF	KUHF	GHF	Δ
Cu	−1653.186332	−1653.186332	−1653.186332	−1653.169972	−1653.169972	0.000000
Ag	−5312.905841	−5312.905841	−5312.905841	−5312.467469	−5312.467470	0.000001
Au	−19011.187190	−19011.187190	−19011.187190	−18999.596626	−18999.596640	0.000014

Table 4.2 shows the spinor energies of an Au atom in the ground state at the SF- and SD-IODKH/NR levels. In the SF calculations, KUHF give the same spinor energies as UHF and GHF for each spin. In the SD calculations, KUHF yields very similar spinor energies to GHF. The maximum absolute deviations are 0.000032, 0.001354, 0.003975, and 0.000132 hartrees, for s, p, d, and f spinors, respectively. The magnitudes of the deviations for valence spinors are higher than those for core spinors because the configuration in the core region is close to the closed-shell configuration and the occupation numbers are almost unique.

The spinors given by KUHF have exactly $(2j+1)$-fold degeneracies in the SD calculations. The p, d, and f spinor levels split in ratios of two to four, four to six, and six to eight, respectively, indicating that KUHF properly describes the SO interactions. In contrast, slight energy differences are seen among the spinors in the same group in the GHF results, although they possess approximately $(2j+1)$-fold degeneracies. KUHF is similar to a *jj*-coupling scheme, while GHF is based on the mixed-coupling procedure

and yields a broken-symmetry solution with a mixture of *LS*- and *jj*-coupling schemes as pointed out in Ref. [39].

4.3.3 Potential energy curves

This subsection discusses the dissociation curves for HAt molecule at the SF- and SD-IODKH/NR levels. In the ground state, HAt dissociates into ^2S hydrogen and ^2P astatine atoms via the $^1\Sigma_g$ surface. If spin is a good quantum number, $m_s = 0$ is required to describe the HAt molecule in the singlet state. On the other hand, each of the dissociated atoms requires $m_s = \pm 1/2$, and, consequently, the overall system has $m_s = 0, \pm 1$. In consequence, pseudo-singlet and pseudo-triplet states were specified in KUHF, while singlet and triplet ones were used in the UHF case. Hereafter, a UHF solution obtained from the singlet (triplet) configuration is simply expressed as a singlet (triplet) solution, although it does not correspond to the exact singlet (triplet) state due to the S^2 symmetry breaking.

Figure 4.3(a) shows the dissociation curves for HAt using the SF-IODKH/NR Hamiltonian. The RHF curve is identical to the UHF curve in the singlet state near the equilibrium bond length. As dissociation proceeds, the RHF solution yields a higher energy than the UHF solution in the singlet state. At the dissociation limit, the RHF energy exceeds the sum of the atomic total energies. This is a well-known problem of RHF, and RHF cannot describe the dissociation limit because the spin pair occupies the same spatial orbital. In contrast, the UHF solution in the singlet state describes well the open-singlet spin state of the overall system at the dissociation limit. The UHF calculation in the triplet state gives a repulsive curve and converges to the correct dissociation limit.

Figure 4.3(b) shows the dissociation curves given by KUHF as well as KRHF and

GHF using the SD-IODKH/NR Hamiltonian. The KRHF calculation gives the similar curve to those of the KUHF calculation in the pseudo-singlet state and the GHF calculation near the equilibrium bond length. The KUHF solutions in the pseudo-singlet and pseudo-triplet states and the GHF solution describe the correct dissociation limit, while the KRHF solution cannot; the KUHF calculation in the pseudo-triplet state gives a repulsive curve. These potential energy curves in the SD calculations are similar to those in the SF curves: the solutions of KUHF considering SD relativistic effects correspond to those of UHF.

It should be noted that the shapes of the SD curves are not completely identical to those of the SF curves although they are similar. The difference of the shapes leads to the difference of dissociation energies: 44.5 kcal/mol and 29.6 kcal/mol at the SF and SD levels, respectively. As the bond distance increases, the SD solutions give relatively lower energies than the SF solutions. This energy lowering is due to the stabilization of the ^2P state of the dissociated astatine atom, induced by the SO interactions. As a result, the dissociation energy in the SD calculation decreased by 14.9 kcal/mol in comparison with the SF calculation.

Table 4.2. Spinor energies (in hartrees) of the Au atom computed by UHF, KUHF, and GHF using the SF- and SD-IODKH/NR Hamiltonians. Δ shows the energy deviations of KUHF from GHF in the SD-IODKH/NR calculations.

Spinor	SF-IODKH/NR		Spinor	SD-IODKH/NR					
	UHF, KUHF, GHF			KUHF		GHF		Δ	
	alpha	beta		pseudo-alpha	pseudo-beta			pseudo-alpha	pseudo-beta
1s	−2983.472572	−2983.470752	$1s_{1/2}$	−2983.664511	−2983.662702	−2983.664524	−2983.662701	0.000013	−0.000002
2s	−531.922682	−531.921901	$2s_{1/2}$	−532.059911	−532.059123	−532.059921	−532.059124	0.000010	0.000000
2p	−461.553351	−461.553801	$2p_{1/2}$	−502.780464	−502.780769	−502.780572	−502.780674	0.000108	−0.000095
	−461.553351	−461.553801	$2p_{3/2}$	−439.732360	−439.732946	−439.732560	−439.732947	0.000200	0.000002
	−461.553351	−461.553801		−439.732360	−439.732946	−439.732369	−439.732753	0.000009	−0.000192
3s	−128.057989	−128.056136	$3s_{1/2}$	−128.142654	−128.140799	−128.142665	−128.140797	0.000011	−0.000003
3p	−107.229837	−107.229487	$3p_{1/2}$	−115.639180	−115.638740	−115.639038	−115.638891	−0.000142	0.000151
	−107.229837	−107.229487	$3p_{3/2}$	−102.135773	−102.135535	−102.135780	−102.135617	0.000007	0.000081
	−107.229837	−107.229487		−102.135773	−102.135535	−102.135698	−102.135536	−0.000075	0.000001
3d	−84.017649	−84.018066	$3d_{3/2}$	−86.274412	−86.274738	−86.274548	−86.274676	0.000137	−0.000062
	−84.017649	−84.018066		−86.274412	−86.274738	−86.274484	−86.274612	0.000072	−0.000126
	−84.017649	−84.018066	$3d_{5/2}$	−82.647564	−82.648064	−82.647767	−82.648066	0.000202	0.000002
	−84.017649	−84.018066		−82.647564	−82.648064	−82.647668	−82.647965	0.000104	−0.000098
	−84.017649	−84.018066		−82.647564	−82.648064	−82.647570	−82.647866	0.000006	−0.000198
4s	−29.137833	−29.135044	$4s_{1/2}$	−29.183216	−29.180427	−29.183230	−29.180418	0.000015	−0.000009
4p	−22.163133	−22.162820	$4p_{1/2}$	−24.066645	−24.066301	−24.066535	−24.066420	−0.000110	0.000118
	−22.163133	−22.162820	$4p_{3/2}$	−20.910842	−20.910559	−20.910849	−20.910653	0.000007	0.000094
	−22.163133	−22.162820		−20.910842	−20.910559	−20.910750	−20.910557	−0.000092	−0.000001
4d	−13.449587	−13.450163	$4d_{3/2}$	−13.949353	−13.949768	−13.949525	−13.949688	0.000173	−0.000081
	−13.449587	−13.450163		−13.949353	−13.949768	−13.949443	−13.949607	0.000090	−0.000161
	−13.449587	−13.450163	$4d_{5/2}$	−13.175584	−13.176270	−13.175858	−13.176271	0.000273	0.000001
	−13.449587	−13.450163		−13.175584	−13.176270	−13.175722	−13.176132	0.000138	−0.000138
	−13.449587	−13.450163		−13.175584	−13.176270	−13.175589	−13.175994	0.000004	−0.000276
5s	−4.683457	−4.679816	$5s_{1/2}$	−4.697489	−4.693773	−4.697507	−4.693759	0.000018	−0.000015

Table 4.2. *(Continued.)*

Spinor	SF-IODKH/NR		Spinor	SD-IODKH/NR					
	UHF, KUHF, GHF			KUHF		GHF		Δ	
	alpha	beta		pseudo-alpha	pseudo-beta			pseudo-alpha	pseudo-beta
4f	−3.789548	−3.789821	$4f_{5/2}$	−3.958448	−3.958660	−3.958543	−3.958632	0.000095	−0.000028
	−3.789548	−3.789821		−3.958448	−3.958660	−3.958513	−3.958602	0.000065	−0.000057
	−3.789548	−3.789821		−3.958448	−3.958660	−3.958483	−3.958573	0.000035	−0.000087
	−3.789548	−3.789821	$4f_{7/2}$	−3.735189	−3.735496	−3.735322	−3.735499	0.000132	0.000002
	−3.789548	−3.789821		−3.735189	−3.735496	−3.735278	−3.735454	0.000089	−0.000043
	−3.789548	−3.789821		−3.735189	−3.735496	−3.735235	−3.735409	0.000046	−0.000087
	−3.789548	−3.789821		−3.735189	−3.735496	−3.735193	−3.735365	0.000003	−0.000131
5p	−2.741429	−2.744912	$5p_{1/2}$	−3.065739	−3.069749	−3.067093	−3.068431	0.001354	−0.001318
	−2.741429	−2.744911	$5p_{3/2}$	−2.532606	−2.535076	−2.533418	−2.535063	0.000812	−0.000013
	−2.741429	−2.744911		−2.532606	−2.535076	−2.532621	−2.534232	0.000015	−0.000844
5d	−0.456969	−0.448494	$5d_{3/2}$	−0.508588	−0.501140	−0.507258	−0.504354	−0.001330	0.003214
	−0.456969	−0.448494		−0.508588	−0.501140	−0.505842	−0.502782	−0.002745	0.001642
	−0.456969	−0.448494	$5d_{5/2}$	−0.434483	−0.425130	−0.434498	−0.428642	0.000015	0.003511
	−0.456969	−0.448494		−0.434483	−0.425130	−0.432456	−0.426847	−0.002027	0.001716
	−0.456969	−0.448494		−0.434483	−0.425130	−0.430508	−0.425115	−0.003975	−0.000016
6s	−0.291814	—	$6s_{1/2}$	−0.293449	—	−0.293481	—	0.000032	—

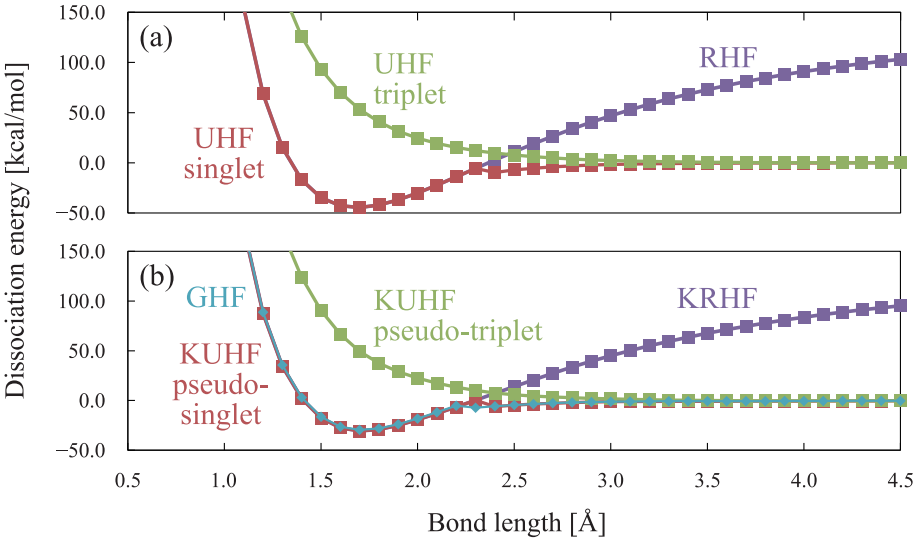

Figure 4.3. Potential energy curves of the HAt molecule computed at the (a) SF- and (b) SD-IODKH/NR levels.

4.3.4 SCF convergence

This subsection discusses the SCF convergence of KUHF. The d- and f-block atoms, which commonly require a large number of SCF cycles (as seen in the previous study by the author and co-workers [30]), were used as test systems. For comparison, GHF calculations were also performed. Table 4.3 shows the number of cycles required to converge the SCF calculation for the d-block atoms. Here, N.C. means that the convergence was not obtained within 1000 cycles. The average number of cycles (Average) and the number of systems that failed to converge (#Failure) are also shown.

Among the 29 d-block elements, 19 elements required fewer cycles in KUHF than in GHF. The average number of cycles decreased from 173.9 in GHF to 108.1 in KUHF. #Failure was one in KUHF, but two in GHF. The partial use of time-reversal symmetry in KUHF thus improves the SCF convergence behavior in the SD relativistic calculations for many d-block systems. However, for several elements (V, Mn, Zn, Y, Zr, Tc, Pd, Cd, and Re), KUHF worsened the convergence behavior compared with GHF. The difficulty

in convergence of the group 7 elements, i.e., Mn, Tc, and Re, seems to arise from their high spin multiplicities. For the closed-shell systems, including Zn, Pd, and Cd, KUHF is equivalent to KRHF from a theoretical point of view. KUHF involves redundant calculations for these systems because the pseudo-alpha and pseudo-beta calculations are identical. Using KRHF instead of KUHF halves the cost of the formation and the diagonalization of the Fock matrix. Thus, KRHF covers a large number of SCF cycles for these closed-shell systems and reduces effective computational time. For V, Y, and Zr, electronic fluctuations between 4d and 5s spinors during the SCF iterations may occur, which results in poor convergence behavior in the KUHF calculations.

Table 4.4 shows the results of the similar assessment for the f-block atoms. Among the 30 f-block elements, 23 elements require fewer cycles in KUHF than in GHF. The average number of cycles decreased from 285.8 in GHF to 78.8 in KUHF. In addition, #Failure was one in KUHF, but five in GHF. For Ce, Ho, Yb, Ac, No, and Lr, KUHF required more cycles than GHF. As seen in the d-block systems, a greater number of iterations were required for closed-shell systems, e.g., Yb and No. For the other elements (Ce, Ho, Ac, and Lr), the poor convergence behavior seems to originate from the electronic fluctuations among the orbitals that possess different orbital angular momenta.

Table 4.3. Number of cycles required for SCF convergence for d-block atoms using KUHF and GHF. N.C. means no convergence within 1000 cycles. #Failure is the number of elements that gave N.C. Average is the average number of cycles, where the N.C. elements are excluded. The difference of KUHF from GHF is also shown as Δ.

Element	KUHF	GHF	Δ
Sc	16	417	−401
Ti	20	215	−195
V	N.C.	120	—
Cr	10	48	−38
Mn	279	23	256
Fe	17	380	−363
Co	70	623	−553
Ni	16	662	−646
Cu	11	16	−5
Zn	33	16	17
Y	707	127	580
Zr	968	79	889
Nb	19	N.C.	—
Mo	13	33	−20
Tc	568	26	542
Ru	27	N.C.	—
Rh	10	137	−127
Pd	26	16	10
Ag	15	15	0
Cd	20	14	6
Hf	10	166	−156
Ta	8	492	−484
W	19	21	−2
Re	56	26	30
Os	25	319	−294
Ir	32	59	−27
Pt	9	613	−604
Au	11	19	−8
Hg	11	14	−3
Average	108.1	173.9	−61.4
#Failure	1	2	−1

Table 4.4. Number of cycles required for SCF convergence for f-block atoms using KUHF and GHF. N.C. means no convergence within 1000 cycles. #Failure is the number of elements that gave N.C. Average is the average number of cycles, where the N.C. elements are excluded. The difference of KUHF from GHF is also shown as Δ.

Element	KUHF	GHF	Δ
La	N.C.	N.C.	—
Ce	854	181	673
Pr	25	147	−122
Nd	11	N.C.	—
Pm	26	N.C.	—
Sm	25	32	−7
Eu	21	43	−22
Gd	23	915	−892
Tb	33	62	−29
Dy	16	138	−122
Ho	30	25	5
Er	28	589	−561
Tm	25	443	−418
Yb	23	20	3
Lu	47	54	−7
Ac	73	37	36
Th	9	36	−27
Pa	26	N.C.	—
U	22	888	−866
Np	37	N.C.	—
Pu	18	847	−829
Am	21	53	−32
Cm	32	962	−930
Bk	32	75	−43
Cf	18	694	−676
Es	18	105	−87
Fm	16	320	−304
Md	275	387	−112
No	121	44	77
Lr	379	49	330
Average	78.8	285.8	−198.5
#Failure	1	5	−4

4.4 Conclusion

In this chapter, an open-shell HF theory for SD two-component relativistic calculations, which is termed KUHF, has been developed. As KRHF is a quaternionic counterpart of RHF, the present KUHF method is defined as a quaternionic counterpart of UHF, partly exploiting time-reversal symmetry. For the numerical assessments, the total energies for the coinage metal atoms, the spinor energies for the Au atom, and the potential energy curves for the HAt molecule were investigated. These numerical results confirmed that KUHF gives very similar energies to those of GHF for ground state calculations. KUHF gives a corresponding solution to UHF, including the SO interactions. Furthermore, KUHF was found to improve the SCF convergence behavior for the d- and f-block elements in the SD relativistic calculations, of which convergences are difficult to be achieved in the standard GHF calculations.

References

[1] R. E. Moss, Advanced Molecular Quantum Mechanics: An Introduction to Relativistic Quantum Mechanics and the Quantum Theory of Radiation, Chapman and Hall, London, 1973.

[2] L. L. Foldy, S. A. Wouthuysen, *Phys. Rev.* **78**, 29 (1950).

[3] M. Douglas, N. M. Kroll, *Ann. Phys. (Leipzig)* **82**, 89 (1974).

[4] B. A. Hess, *Phys. Rev. A* **32**, 756 (1985).

[5] E. van Lenthe, E. J. Baerends, J. G. Snijders, *J. Chem. Phys.* **99**, 4597 (1993).

[6] S. Faas, J. G. Snijders, J. H. van Lenthe, E. van Lenthe, E. J. Baerends, *Chem. Phys. Lett.* **246**, 632 (1995).

[7] R. Samzow, B. A. Hess, G. Jansen, *J. Chem. Phys.* **96**, 1227 (1992).

[8] K. G. Dyall, *J. Chem. Phys.* **106**, 9618 (1997).

[9] T. Nakajima, K. Hirao, *J. Chem. Phys.* **113**, 7786 (2000).

[10] A. Wolf, M. Reiher, B. A. Hess, *J. Chem. Phys.* **117**, 9215 (2002).

[11] M. Barysz, A. J. Sadlej, *J. Chem. Phys.* **116**, 2696 (2002).

[12] C. van Wüllen, C. Michauk, *J. Chem. Phys.* **123**, 204113 (2005).

[13] D. Peng, W. Liu, Y. Xiao, L. Cheng, *J. Chem. Phys.* **127**, 104106 (2007).

[14] J. Sikkema, L. Visscher, T. Saue, M. Iliaš, *J. Chem. Phys.* **131**, 124116 (2009).

[15] W. Liu, *Mol. Phys.* **108**, 1679 (2010).

[16] H. Fukutome, *Int. J. Quantum Chem.* **20**, 955 (1981).

[17] J. L. Stuber, J. Paldus, in: E. J. Brändas, E. S. Kryachko (Eds.), Fundamental World of Quantum Chemistry, Kluwer Academic Publishers, Dordrecht, 2003, p. 67.

[18] R. Seeger, J. A. Pople, *J. Chem. Phys.* **66**, 3045 (1977).

[19] J.-L. Calais, *Adv. Quantum Chem.* **17**, 225 (1985).

[20] R. McWeeny, Methods of Molecular Quantum Mechanics, Academic Press, London, 1989.

[21] P.-O. Löwdin, I. Mayer, *Adv. Quantum Chem.* **24**, 79 (1992).

[22] S. Hammes-Schiffer, H. C. Andersen, *J. Chem. Phys.* **99**, 1901 (1993).

[23] S. K. Wolff, D. Jayatilaka, G. S. Chandler, *J. Chem. Phys.* **103**, 4562 (1995).

[24] D. Jayatilaka, *J. Chem. Phys.* **108**, 7587 (1998).

[25] M. K. Armbruster, F. Weigend, C. van Wüllen, W. Klopper, *Phys. Chem. Chem. Phys.* **10**, 1748 (2008).

[26] J. J. Goings, F. Ding, M. J. Frisch, X. Li, *J. Chem. Phys.* **142**, 154109 (2015).

[27] P. Pulay, *Chem. Phys. Lett.* **73**, 393 (1980).

[28] P. Pulay, *J. Comput. Chem.* **3**, 556 (1982).

[29] K. N. Kudin, G. E. Scuseria, E. Cancès, *J. Chem. Phys.* **116**, 8255 (2002).

[30] M. Nakano, J. Seino, H. Nakai, *Chem. Phys. Lett.* **657**, 65 (2016).

[31] P. Hafner, W. H. E. Schwarz, *Chem. Phys. Lett.* **65**, 537 (1979).

[32] P. Hafner, *J. Phys. B: At., Mol. Opt. Phys.* **13**, 3297 (1980).

[33] N. Rösch, *Chem. Phys.* **80**, 1 (1983).

[34] S. Y. Lee, Y. S. Lee, *J. Comput. Chem.* **13**, 595 (1992).

[35] A. Rosen, D. E. Ellis, *J. Chem. Phys.* **62**, 3039 (1975).

[36] D. E. Ellis, G. L. Goodman, *Int. J. Quantum Chem.* **25**, 185 (1984).

[37] F. Wang, W. Liu, *J. Chin. Chem. Soc.* **50**, 597 (2003).

[38] Y. S. Kim, S. Y. Lee, W. S. Oh, B. H. Park, Y. K. Han, S. J. Park, Y. S. Lee, *Int. J. Quantum Chem.* **66**, 91 (1998).

[39] I. Kim, Y. S. Lee, *Bull. Korean Chem. Soc.* **34**, 179 (2013).

[40] J. J. Dongarra, J. R. Gabriel, D. D. Koelling, J. H. Wilkinson, *J. Comput. Phys.* **54**,

278 (1984).

[41] J. J. Dongarra, J. R. Gabriel, D. D. Koelling, J. H. Wilkinson, *Linear Algebra Appl.* **60**, 27 (1984).

[42] T. Koga, H. Tatewaki, T. Shimazaki, *Chem. Phys. Lett.* **328**, 473 (2000).

[43] Y. Osanai, T. Noro, E. Miyoshi, M. Sekiya, T. Koga, *J. Chem. Phys.* **120**, 6408 (2004).

[44] P. Lykos, G. W. Pratt, *Rev. Mod. Phys.* **35**, 496 (1963).

Chapter 5

Spin-dependent relativistic open-shell Hartree–Fock theory using time-reversal symmetry: The restricted approach

5.1 Introduction

Two types of open-shell HF methods, i.e., UHF [1] and ROHF [2], are fundamental tools in the quantum chemical study of paramagnetic systems. ROHF is in general applicable to arbitrary open-shell configurations [3-6], while UHF can only be applied to half-filled high-spin open-shell systems [7]. The deficiency of ROHF is the partial arbitrariness in the construction of the Fock operator, which results in unphysical MOs and orbital energies. Plakhutin and co-workers [7-10] have proposed sophisticated solutions of this problem: they derived several conditions to explicitly satisfy KT [11] within a simple ROHF framework. Amended UHF procedures [12-18] have also been proposed as alternatives.

Relativistic effects are vital to the study of paramagnetic systems because they often contain heavy elements. In these systems, SD relativistic effects, such as SO interactions, play an important role as well as scalar or SF relativistic effects. The whole relativistic effects can be accurately considered with four-component or corresponding two-component theories [19-33]. In SD two-component relativistic calculations for open-shell systems, the GHF method [34-43], with no symmetry constraints, is usually employed. However, GHF commonly shows poor convergence behavior, and hybridization of different spin states by SD relativistic effects makes it difficult to interpret GHF solutions

[44,45]. In the previous chapter, the author reformulated an alternative of relativistic open-shell HF theory, termed the KUHF method [46-48]. KUHF was redefined as a relativistic analogue of UHF by the partial use of time-reversal symmetry and by quaternion algebra in the same manner that the KRHF method [49-52] can be interpreted as a relativistic analogue of RHF. KUHF inherits most of the properties of UHF theory. Hence, relativistic ROHF theory is required to complement the deficiencies of UHF, as seen in the NR case.

In the relativistic, Kramers-restricted regime, an open-shell system is often treated by the AOC type of ROHF theory [53-55]. The single determinant wavefunction of AOC-ROHF is expressed by the average of several configurations, leading to fractional occupation numbers. In this chapter, a simpler relativistic ROHF method using time-reversal symmetry, termed the KROHF method, is formulated as a relativistic analogue of the well-established ROHF theory. KROHF is based on the KUHF method. In particular, a canonical KROHF expression where spinor energies satisfy KT is derived, based on the procedure proposed by Plakhutin et al. [8] for ROHF theory. In addition, behaviors of other canonicalization schemes are also discussed.

This chapter is organized as follows. In Sec. 5.2, the theoretical aspects of KROHF are presented. This section also discusses the canonical parametrization of KROHF, which relates to KT. Section 5.3 reports numerical assessments of KROHF. Finally, Sec. 5.4 presents concluding remarks.

5.2 Theory

As a first step, the present KROHF theory takes the SODS approach, although Plakhutin and Davidson [7] recently proposed a more general DODS approach. This is because the SODS approach is simpler to implement and more common in the NR framework. KROHF here is designed to give Kramers-degenerate spinors, where each spinor pair is connected with the time-reversal operation, as common ROHF theory gives degenerate alpha and beta orbitals under spin restriction.

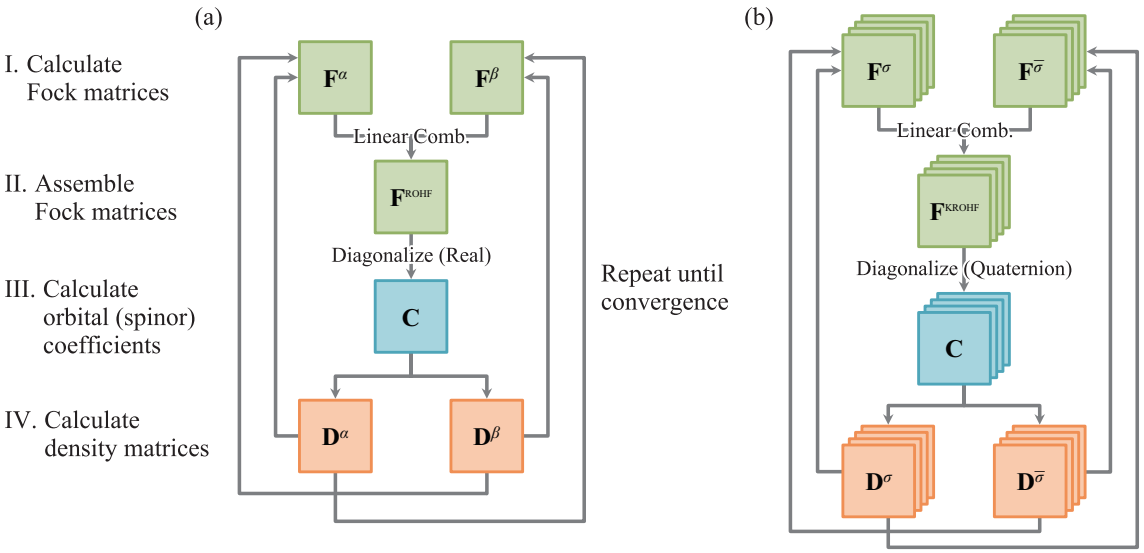

Figure 5.1. Schematic of (a) ROHF and (b) KROHF procedures. The mono- and four-layered squares represent real and quaternion matrices, respectively.

Figure 5.1(a) shows the computational procedure of the ROHF method within the SODS approach. In Figure 5.1, mono- and four-layered squares represent the real and quaternion matrices, respectively. In ROHF, the UHF Fock matrices for alpha and beta spin components ($\mathbf{F}^{\alpha}$ and $\mathbf{F}^{\beta}$) are first calculated. $\mathbf{F}^{\alpha}$ and $\mathbf{F}^{\beta}$ are then assembled to give Roothaan's effective Fock matrix of ROHF $\mathbf{F}^{\mathrm{ROHF}}$. There are various procedures to construct $\mathbf{F}^{\mathrm{ROHF}}$ [2,8,10,56-61]. After assembling, $\mathbf{F}^{\mathrm{ROHF}}$ is diagonalized to obtain the

MO coefficients $\mathbf{C}$. Furthermore, the square of $\mathbf{C}$ together with the occupation numbers for alpha and beta orbitals yields the alpha and beta density matrices ($\mathbf{D}^{\alpha}$ and $\mathbf{D}^{\beta}$), respectively. This procedure is iterated until the values of the total electronic energy and/or matrix elements converge. Here, all the matrices are defined in real space.

Similar to the extension of UHF to KUHF, KROHF is defined as a relativistic analogue of the ROHF method. Hence, the computational procedure of KROHF is obtained by replacing the real matrices of ROHF with quaternion matrices, as shown in Figure 5.1(b). As is the case with KUHF, KROHF is formulated for the pseudo-alpha and pseudo-beta spin bases instead of the alpha and beta spin bases.

First, from the analogy of the familiar energy expression in ROHF, the KROHF total electronic energy in the MS basis is defined as

$$E^{\mathrm{KROHF}} = 2\sum_{i}^{\{\mathrm{occ.}\}} f_i \, {}^{\mathrm{Q}}h_{ii} + \sum_{ij}^{\{\mathrm{occ.}\}} f_i f_j \left(2a_{ij} \, {}^{\mathrm{Q}}J_{ij} - b_{ij} \, {}^{\mathrm{Q}}K_{ij} \right), \tag{5.1}$$

where *h*, *J*, and *K* denote the one-electron, Coulomb, and exchange parts of the KROHF Fock matrix defined below, respectively. Parameters *a* and *b* are constants specific to the states. Here, as a first step, the scalar cases are assumed for *a* and *b*, although they should have matrix structures to describe special cases, i.e., non-Roothaan γ^N states [62-64]. In addition, Eq. (5.1) is equivalent to the total energy expression in KRHF when $a = b = 1$.

According to Figure 5.1(b), the RH equation of KROHF is defined as

$${}^{\mathrm{Q}}\mathbf{F}^{\mathrm{KROHF}} \, {}^{\mathrm{Q}}\mathbf{C} = {}^{\mathrm{Q}}\mathbf{S} \, {}^{\mathrm{Q}}\mathbf{C}\boldsymbol{\varepsilon}, \tag{5.2}$$

where ${}^{\mathrm{Q}}\mathbf{F}^{\mathrm{KROHF}}$ is Roothaan's effective Fock operator extended to quaternions. Analogous to the ROHF theory, ${}^{\mathrm{Q}}\mathbf{F}^{\mathrm{KROHF}}$ is given by

$$
{}^{\mathrm{Q}}\mathbf{F}^{\mathrm{KROHF}} = \begin{pmatrix} {}^{\mathrm{Q}}\mathbf{R}_{\mathrm{CC}} & {}^{\mathrm{Q}}\mathbf{F}_{\mathrm{CO}} & {}^{\mathrm{Q}}\mathbf{F}_{\mathrm{CV}} \\ {}^{\mathrm{Q}}\mathbf{F}_{\mathrm{OC}} & {}^{\mathrm{Q}}\mathbf{R}_{\mathrm{OO}} & {}^{\mathrm{Q}}\mathbf{F}_{\mathrm{OV}} \\ {}^{\mathrm{Q}}\mathbf{F}_{\mathrm{VC}} & {}^{\mathrm{Q}}\mathbf{F}_{\mathrm{VO}} & {}^{\mathrm{Q}}\mathbf{R}_{\mathrm{VV}} \end{pmatrix}. \tag{5.3}
$$

Hereafter, subscripts C, O, and V represent closed-, open-, and virtual-shell MSs, respectively. The Fock matrix elements that connect the different categories of MSs, i.e., off-diagonal blocks of the Fock matrix, must vanish when the energy reaches a stationary point. The off-diagonal blocks of Eq. (5.3) are thus given by considering the variational principle under canonicalization conditions [2,56,65]. Then,

$$
{}^{\mathrm{Q}}\mathbf{F}_{\mathrm{CO}} = {}^{\mathrm{Q}}\mathbf{F}^{\bar{\sigma}}, \tag{5.4}
$$

$$
{}^{\mathrm{Q}}\mathbf{F}_{\mathrm{CV}} = \frac{1}{2}\left({}^{\mathrm{Q}}\mathbf{F}^{\sigma} + {}^{\mathrm{Q}}\mathbf{F}^{\bar{\sigma}} \right), \tag{5.5}
$$

and

$$
{}^{\mathrm{Q}}\mathbf{F}_{\mathrm{OV}} = {}^{\mathrm{Q}}\mathbf{F}^{\sigma} \tag{5.6}
$$

are obtained. Here, ${}^{\mathrm{Q}}\mathbf{F}^{\sigma}$ and ${}^{\mathrm{Q}}\mathbf{F}^{\bar{\sigma}}$ are the pseudo-alpha and pseudo-beta KUHF Fock matrices, whose elements are

$$
{}^{\mathrm{Q}}F^{\sigma}_{\mu\nu} = {}^{\mathrm{Q}}h_{\mu\nu} + {}^{\mathrm{Q}}J^{\sigma}_{\mu\nu} + {}^{\mathrm{Q}}J^{\bar{\sigma}}_{\mu\nu} - {}^{\mathrm{Q}}K^{\sigma}_{\mu\nu} \tag{5.7}
$$

and

$$
{}^{\mathrm{Q}}F^{\bar{\sigma}}_{\mu\nu} = {}^{\mathrm{Q}}h_{\mu\nu} + {}^{\mathrm{Q}}J^{\bar{\sigma}}_{\mu\nu} + {}^{\mathrm{Q}}J^{\sigma}_{\mu\nu} - {}^{\mathrm{Q}}K^{\bar{\sigma}}_{\mu\nu}, \tag{5.8}
$$

respectively. The details of these equations are given in Sec. 4.2. The lower-triangular blocks of Eq. (5.3) can be deduced from the Hermiticity of the Fock matrix. At SCF convergence, the Fock matrix elements of the off-diagonal blocks go to zero as follows:

$$
\left\langle {}^{\mathrm{Q}}\varphi_k \middle| {}^{\mathrm{Q}}\hat{F}^{\bar{\sigma}} \middle| {}^{\mathrm{Q}}\varphi_m \right\rangle = 0 \tag{5.9}
$$

$$
\left\langle {}^{\mathrm{Q}}\varphi_k \middle| \frac{1}{2}\left({}^{\mathrm{Q}}\hat{F}^{\sigma} + {}^{\mathrm{Q}}\hat{F}^{\bar{\sigma}} \right) \middle| {}^{\mathrm{Q}}\varphi_a \right\rangle = 0 \tag{5.10}
$$

$$\left\langle {}^{\mathrm{Q}}\varphi_m \middle| {}^{\mathrm{Q}}\hat{F}^{\sigma} \middle| {}^{\mathrm{Q}}\varphi_a \right\rangle = 0, \tag{5.11}$$

where $\{k,l,\cdots\}$, $\{m,n,\cdots\}$, and $\{a,b,\cdots\}$ refer to the closed-, open-, and virtual-shell spinors, respectively. The conditions in Eqs. (5.9)–(5.11) are the quaternion versions of the well-known Brillouin's theorem [66].

In contrast, the diagonal blocks of Eq. (5.3) are arbitrary; the choice of the diagonal blocks has no effect on the density matrices, total electronic energy, and total electronic wavefunction. In the NR framework, the diagonal blocks are commonly given by a linear combination of the alpha and beta UHF Fock matrices. Similarly, KROHF defines the diagonal blocks of the Fock matrix by a linear combination of the pseudo-alpha and pseudo-beta KUHF Fock matrices using arbitrary coupling coefficients *A* and *B*,

$${}^{\mathrm{Q}}\mathbf{R}_{\mathrm{XX}} = A_{\mathrm{XX}}\,{}^{\mathrm{Q}}\mathbf{F}^{\sigma} + B_{\mathrm{XX}}\,{}^{\mathrm{Q}}\mathbf{F}^{\bar{\sigma}}, \tag{5.12}$$

where X = C, O, and V.

Although they do not affect the total energy and properties, the choice of the coupling coefficients may result in two problematic situations. First, the coupling coefficients significantly affect SCF convergence. This is because uneven choices of the coefficients may yield numerically ill-balanced situations. In the ROHF study by Guest and Saunders [56], they pointed out that the use of entirely balanced coefficients,

$$A_{\mathrm{CC}} = A_{\mathrm{OO}} = A_{\mathrm{VV}} = B_{\mathrm{CC}} = B_{\mathrm{OO}} = B_{\mathrm{VV}} = \frac{1}{2}, \tag{5.13}$$

empirically shows good SCF convergence behavior. In the present chapter, the parameter set of Eq. (5.13) is termed the GS set.

Second, the choice of *A* and *B* also affects the spinor energies and coefficients. This is because the spinor energies of KROHF are given by

$$\varepsilon_i = \left\langle {}^{\mathrm{Q}}\varphi_i \middle| A_{\mathrm{XX}}\, {}^{\mathrm{Q}}\hat{F}^{\sigma} + B_{\mathrm{XX}}\, {}^{\mathrm{Q}}\hat{F}^{\bar{\sigma}} \middle| {}^{\mathrm{Q}}\varphi_i \right\rangle = \left(A_{\mathrm{XX}}\, {}^{\mathrm{Q}}\mathbf{F}^{\sigma} + B_{\mathrm{XX}}\, {}^{\mathrm{Q}}\mathbf{F}^{\bar{\sigma}} \right)_{ii} \tag{5.14}$$

and they explicitly depend on the coupling coefficients, *A* and *B*. It is clear from Eq. (5.14) that a thoughtless choice of the coefficients results in physically meaningless spinor energies. Here, a set of coupling coefficients that yields spinor energies to satisfy KT will be derived, following the procedure proposed by Plakhutin, Gorelik, and Breslavskaya [8].

In KT, negative-signed spinor energies equal the corresponding vertical IP or EA. The present chapter assumes that ionization occurs to give a high-spin configuration. Hence, the following three ionization processes are considered: removing a pseudo-beta electron from the *k*-th closed-shell MS, removing a pseudo-alpha electron from the *m*-th open-shell MS, and attaching a pseudo-alpha electron into the *a*-th virtual-shell MS. KT for these situations is written as

$$I_k = -\varepsilon_k \tag{5.15}$$

$$I_m = -\varepsilon_m \tag{5.16}$$

$$A_a = -\varepsilon_a\,, \tag{5.17}$$

where *I* and *A* are IP and EA, respectively. From Eqs. (5.7), (5.8), and (5.14), together with the assumption on the ionization processes mentioned above, the spinor energies in KROHF are given by

$$\begin{aligned} \varepsilon_i = {} & \left(A_{\mathrm{XX}} + B_{\mathrm{XX}} \right) {}^{\mathrm{Q}}h_{ii} \\ & + \sum_k \left(A_{\mathrm{XX}} + B_{\mathrm{XX}} \right) \left(2\, {}^{\mathrm{Q}}J_{ik} - {}^{\mathrm{Q}}K_{ik} \right) \\ & + \sum_m \left\{ \left(A_{\mathrm{XX}} + B_{\mathrm{XX}} \right) {}^{\mathrm{Q}}J_{im} - A_{\mathrm{XX}}\, {}^{\mathrm{Q}}K_{im} \right\}. \end{aligned} \tag{5.18}$$

The vertical IP and EA are given by

$$I_i = E^{\mathrm{KROHF}}_{\mathrm{frozen}}\left(S^{+} \right) - E^{\mathrm{KROHF}}\left(S \right) \tag{5.19}$$

$$A_i = E^{\mathrm{KROHF}}\left(S\right) - E^{\mathrm{KROHF}}_{\mathrm{frozen}}\left(S^{-}\right), \tag{5.20}$$

where $E^{\mathrm{KROHF}}\left(S\right)$ is the KROHF energy for the initial system *S*; similar is the notation for the ionized systems $S^{\pm}$. Here, the FOA underlying KT is adopted: the same orbitals (spinors) and integrals as the initial system S are used to calculate $E^{\mathrm{KROHF}}_{\mathrm{frozen}}\left(S^{\pm}\right)$. From Eqs. (5.1), (5.19), and (5.20), the IPs and EA corresponding to the three ionization processes above are given by

$$I_k = -\left\{ {}^{\mathrm{Q}}h_{kk} + \sum_l \left(2\,{}^{\mathrm{Q}}J_{kl} - {}^{\mathrm{Q}}K_{kl}\right) + \sum_m {}^{\mathrm{Q}}J_{km} \right\} \tag{5.21}$$

$$I_m = -\left\{ {}^{\mathrm{Q}}h_{mm} + \sum_k \left(2\,{}^{\mathrm{Q}}J_{mk} - {}^{\mathrm{Q}}K_{mk}\right) + \sum_n \left({}^{\mathrm{Q}}J_{mn} - {}^{\mathrm{Q}}K_{mn}\right) \right\} \tag{5.22}$$

$$A_a = -\left\{ {}^{\mathrm{Q}}h_{aa} + \sum_k \left(2\,{}^{\mathrm{Q}}J_{ak} - {}^{\mathrm{Q}}K_{ak}\right) + \sum_m \left({}^{\mathrm{Q}}J_{am} - {}^{\mathrm{Q}}K_{am}\right) \right\}. \tag{5.23}$$

By comparing Eqs. (5.21)–(5.23) with Eq. (5.18), the coupling coefficients which satisfy KT,

$$\begin{aligned} A_{\mathrm{OO}} &= A_{\mathrm{VV}} = B_{\mathrm{CC}} = 1 \\ A_{\mathrm{CC}} &= B_{\mathrm{OO}} = B_{\mathrm{VV}} = 0, \end{aligned} \tag{5.24}$$

are obtained.

In this chapter, the parameter set of Eq. (5.24) is termed the PGB set. Incidentally, the PGB set of Eq. (5.24) is the same as that reported in the ROHF study by Plakhutin et al. [8]. This coincidence is reasonable because of the similarity of KROHF to ROHF. Without the SD relativistic effects, the pseudo-alpha and pseudo-beta spin bases are equivalent to the alpha and beta spin bases. In this case, the formulation of KROHF is equivalent to that of ROHF.

Likewise, the sets of coupling coefficients in KROHF are to be common with those in ROHF for the other canonicalization schemes [2,8,56-61]. The sets of coupling coefficients imported from ROHF studies are summarized in Table 5.1. The table includes

the corresponding A and B values for each set based on the study of Roothaan (R) [2], Davidson (D) [57], Binkley, Pople, and Dobosh (BPD) [58], McWeeny and Diercksen (MD) [59], and Fægri and Manne (FM) [60] as well as the GS [56] and PGB [8] sets. Also shown is the coefficient set derived from the Euler equations (EE) [61]. Hereafter, these parameter sets are denoted by the acronyms of the developers (or the equations) for brevity.

Table 5.1. Sets of coupling coefficients for the diagonal blocks of the Fock matrix in KROHF imported from the ROHF studies.

Set	A_{CC}	A_{OO}	A_{VV}	B_{CC}	B_{OO}	B_{VV}
Guest and Saunders (GS)	1/2	1/2	1/2	1/2	1/2	1/2
Roothaan (R)	−1/2	1/2	3/2	3/2	1/2	−1/2
Davidson (D)	1/2	1	1	1/2	0	0
Binkley, Pople, and Dobosh (BPD)	1/2	1	0	1/2	0	1
McWeeny and Diercksen (MD)	1/3	1/3	2/3	2/3	1/3	1/3
Fægri and Manne (FM)	1/2	1	1/2	1/2	0	1/2
Euler equations (EE)	1/2	1/2	1/2	1/2	0	1/2
Plakhutin, Gorelik, and Breslavskaya (PGB)	0	1	1	1	0	0

* References for each set are described in the text.

5.3 Numerical assessments

5.3.1 Computational details

The KROHF code, together with the quaternion linear algebra module including matrix diagonalization [51,67,68], is implemented into the in-house relativistic program package. The codes of other wavefunction theories, i.e., KUHF and GHF, were also implemented for comparison.

The relativistic Hamiltonian adopted here was composed of the IODKH Hamiltonian [29] for the one-electron part and the NR Coulomb operator for the two-electron part,

which is denoted by IODKH/NR. The SD terms as well as the SF terms of the IODKH/NR Hamiltonian were included (SD-IODKH/NR). In several calculations, only the SF terms were considered (SF-IODKH/NR). The basis sets used here were the DKH3-Gen-TK/NOSec-V-TZP [69,70].

In Sec. 5.3.4, the following options were used to assess SCF convergence. The initial guess orbitals were generated by diagonalization of the bare nucleus Hamiltonian. The hybrid algorithm of Pulay's DIIS [71,72] and EDIIS [73] was employed as the SCF acceleration technique. The SCF convergence criteria were set to 10^{-9} and 10^{-5} a.u. for the differences between two successive iterations in the total electronic energies and in the density matrix elements, respectively.

5.3.2 Total energies

In the previous study on canonical ROHF theory [8], the free N atom was used as a test system. Likewise, the test systems in the present chapter are the free pnictogens including the heavier elements, i.e., N through Bi atoms, in their ground states.

Table 5.2 compares the total energies of the free pnictogen atoms computed by KROHF, KUHF, and GHF at the SD-IODKH/NR level. In each system, KROHF gives the identical total energy regardless of the set of coupling coefficients as discussed in Sec. 5.2. The KROHF and KUHF calculations yield total energies close to the GHF results; the differences are less than 4.003 millihartrees. In addition, the magnitude of the total energies is in the following order: $\mathrm{KROHF} \geq \mathrm{KUHF} \geq \mathrm{GHF}$. This trend reflects the so-called Löwdin's dilemma [74] in broken-symmetry studies: the higher symmetry a wavefunction possesses, the higher its energy is. GHF gives the lowest energy because no symmetry constraints are imposed. In KUHF and KROHF, in contrast, time-reversal

symmetry is partly and fully considered, respectively. Hence, the energy of KROHF is highest.

Table 5.2. Total energies (in hartrees) of the pnictogen atoms in their ground states computed by KROHF, KUHF, and GHF at the SD-IODKH/NR level. The values in parentheses represent the differences from the GHF results.

System	KROHF	KUHF	GHF
N	−54.430043 (0.003520)	−54.433563 (0.000002)	−54.433563
P	−341.536028 (0.000443)	−341.536471 (0.000015)	−341.536471
As	−2259.041489 (0.001397)	−2259.042886 (0.000110)	−2259.042886
Sb	−6477.312245 (0.002073)	−6477.314317 (0.000884)	−6477.314317
Bi	−21518.910907 (0.004003)	−21518.914910 (0.001185)	−21518.914910

5.3.3 Spinor energies

This subsection discusses the spinor energies, which are the most significant properties in the present KROHF theory. Here, the GS set, which is a popular set in NR studies, and the PGB set (derived in Sec. 5.2) are adopted for the coupling coefficients to discuss the basic behaviors of the spinor energies in KROHF. (The behavior of other sets is discussed in the next subsection.) Hereafter, KROHF using the GS set is simply referred to as KROHF(GS), as is the case with other sets.

Table 5.3 shows the spinor energies of the Bi atom in the ground state (electronic configuration $[Hg]6p^3$) computed by KROHF(GS), KROHF(PGB), and KUHF using the SD-IODKH/NR Hamiltonian. The spinor energies in KROHF(PGB) at the SF-IODKH/NR level are also shown. The KUHF columns include the information on the pseudo-alpha and pseudo-beta spinors because KUHF is based on the DODS formalism.

As in the KUHF case, both KROHF(GS) and KROHF(PGB) correctly describe the SO splitting of the spinors. The levels of the p-, d-, and f-spinors are split in the ratios of

1:2, 2:3, and 3:4, respectively. The s-spinors, whose orbital angular momenta are zero, are not split. Each spinor exactly possesses a $(2j+1)$-fold degeneracy at the SD level, while a $(2l+1)$-fold degeneracy at the SF level. Consequently, it is suggested that the SD relativistic effects can be correctly described by the present KROHF theory.

In the KROHF(PGB) results, the energy levels of the closed-shell spinors are very close to those of the pseudo-beta spins given by KUHF. For the open- and virtual-shell spinors, the energy levels obtained by KROHF(PGB) are very similar to those of pseudo-alpha spinors calculated by KUHF. These facts are consistent with the assumptions on the ionization processes to get the PGB set to satisfy KT (described in Sec. 5.2).

In KROHF(GS), on the other hand, all spinor energy levels approximately lie in the middle between the corresponding pseudo-alpha and pseudo-beta spinor energy levels given by KUHF. This is because in the construction of the diagonal blocks of the KROHF Fock matrix [Eq. (5.12)] the contribution of the pseudo-alpha and pseudo-beta spins in KUHF are assembled with the same magnitude for all the spinors using the GS set [Eq. (5.13)].

Table 5.3. Spinor energies (in hartrees) of the Bi atom in the ground state computed by KROHF (using the GS and PGB sets) and KUHF at the SD-IODKH/NR level. Also shown is the result of KROHF with the PGB set at the SF-IODKH/NR level. The values in parentheses represent degeneracies.

SF−IODKH/NR		SD−IODKH/NR				
Spinor	KROHF	Spinor	KROHF		KUHF	
	PGB		GS	PGB	pseudo-alpha	pseudo-beta
1s (2)	−3346.673685	$1s_{1/2}$ (2)	−3347.285569	−3347.284197	−3347.286851	−3347.284481
2s (2)	−607.136374	$2s_{1/2}$ (2)	−607.536574	−607.535591	−607.536587	−607.536505
2p (6)	−521.823938	$2p_{1/2}$ (2)	−546.499508	−546.498140	−546.500460	−546.498870
		$2p_{3/2}$ (4)	−470.448008	−470.446388	−470.449135	−470.447202
3s (2)	−149.266017	$3s_{1/2}$ (2)	−149.490542	−149.489180	−149.491590	−149.489774
3p (6)	−124.421921	$3p_{1/2}$ (2)	−129.890973	−129.889199	−129.892575	−129.889617
		$3p_{3/2}$ (4)	−111.614702	−111.612615	−111.616574	−111.613079
3d (10)	−98.165104	$3d_{3/2}$ (4)	−100.201337	−100.200410	−100.201823	−100.201099
		$3d_{5/2}$ (6)	−95.670417	−95.669485	−95.670814	−95.670263
4s (2)	−35.724942	$4s_{1/2}$ (2)	−35.839573	−35.836548	−35.841588	−35.837731
4p (6)	−27.413941	$4p_{1/2}$ (2)	−28.783939	−28.780671	−28.786447	−28.781534
		$4p_{3/2}$ (4)	−24.079901	−24.076118	−24.082877	−24.077043
4d (10)	−17.470092	$4d_{3/2}$ (4)	−17.970767	−17.968706	−17.971726	−17.969871
		$4d_{5/2}$ (6)	−16.954938	−16.952927	−16.955686	−16.954250
5s (2)	−6.667249	$5s_{1/2}$ (2)	−6.816403	−6.814810	−6.817255	−6.815618
4f (14)	−6.585368	$4f_{5/2}$ (6)	−6.716165	−6.706223	−6.721332	−6.710884
		$4f_{7/2}$ (8)	−6.513239	−6.511731	−6.513982	−6.512566
5p (6)	−4.231103	$5p_{1/2}$ (2)	−4.517131	−4.507114	−4.522016	−4.511847
		$5p_{3/2}$ (4)	−3.622844	−3.613293	−3.627229	−3.618020
5d (10)	−1.297464	$5d_{3/2}$ (4)	−1.383347	−1.371634	−1.390085	−1.376375
		$5d_{5/2}$ (6)	−1.249795	−1.238451	−1.256142	−1.243186
6s (2)	−0.574956	$6s_{1/2}$ (2)	−0.686211	−0.585248	−0.786131	−0.587531
6p (6)	−0.316937	$6p_{1/2}$ (2)	−0.155597	−0.343952	−0.346174	0.016760
		$6p_{3/2}$ (4)	−0.095084	−0.262879	−0.265308	0.049478
7s (2)	0.178947	$7s_{1/2}$ (2)	0.182190	0.169394	0.169428	0.212333

Table 5.4 shows the spinor energy deviations from the negative-signed IP/EA values through the FOA of the Bi atom in the ground state computed by KROHF(GS) and KROHF(PGB). The IP/EA values here are evaluated by Eqs. (5.19) and (5.20). As seen in Table 5.3, KROHF(GS) and KROHF(PGB) give different spinor energies. The MaxADs from the IP/EA values under the FOA are 188.355 and 0.207 millihartrees for the GS and PGB sets, respectively. In particular, the absolute values of the deviations for the occupied spinors are less than one microhartree in KROHF(PGB). The reason for the relatively large deviation for the virtual spinors in comparison with the occupied spinors is that the virtual spinors are not optimized in KROHF calculations. As a result, KROHF(PGB) gives physically more reasonable spinor energies than KROHF(GS).

Let us now compare the spinor energies in KROHF with experimental data. Table 5.5 shows the SO splitting of the outermost p-shells of the pnictogen atoms computed by KROHF(GS) and KROHF(PGB) in accordance with KT at the SD-IODKH/NR level. The experimental IPs in the table are taken from the NIST Atomic Spectra Database [75], and directly reflect the effects of SO interactions.

KROHF(PGB) yields similar IPs to the experimental values, while KROHF(GS) gives irrelevant results. In terms of the deviation from the experimental data, the MaxADs are 9.651 and 1.455 eV in KROHF(GS) and KROHF(PGB), respectively, which supports the physical validity of the PGB set. The deviations in the PGB set arise from the effects of spinor relaxation and electron correlation.

From the viewpoint of the splitting widths between the $p_{1/2}$ and $p_{3/2}$ spinors, for the N and P atoms, the absolute values of deviations are smaller in KROHF(GS) than in KROHF(PGB). However, this does not indicate that the GS set is superior to the PGB set for the description of SO splitting. In systems with small relativistic effects, such as N

and P, the splitting widths are relatively narrow. Therefore, the splitting widths are numerically buried in the errors of the spinor energies due to spinor relaxation and electron correlation. It is hence difficult for these systems to directly compare the IPs calculated within the KT and HF framework with the experimental IPs.

In heavier systems where relativistic effects are significant, i.e., As, Sb, and Bi, the GS splitting widths are buried in the spinor energy deviations as seen in the lighter elements. The deviations of the splitting widths are large; the MaxAD of the splitting is 0.465 eV. In contrast, the PGB set yields physically reasonable spinor energies, with deviations less than 0.094 eV. Hence, the PGB set can perform a qualitatively correct evaluation of the splitting widths.

Table 5.4. Deviations of the spinor energies of the Bi atom in the ground state computed by KROHF from the negative-signed IP/EA values under the FOA (in hartrees). The GS and PGB sets were used for the coupling coefficients. The values in parentheses represent degeneracies.

Spinor	GS	PGB	IP/EA(FOA)
$1s_{1/2}$ (2)	−0.001372	0.000000	3347.284197
$2s_{1/2}$ (2)	−0.000783	0.000000	607.535591
$2p_{1/2}$ (2)	−0.001368	0.000000	546.498140
$2p_{3/2}$ (4)	−0.001620	0.000000	470.446388
$3s_{1/2}$ (2)	−0.001362	0.000000	149.489180
$3p_{1/2}$ (2)	−0.001774	0.000000	129.889199
$3p_{3/2}$ (4)	−0.002087	0.000000	111.612615
$3d_{3/2}$ (4)	−0.000928	0.000000	100.200410
$3d_{5/2}$ (6)	−0.000933	0.000000	95.669485
$4s_{1/2}$ (2)	−0.003025	0.000000	35.836548
$4p_{1/2}$ (2)	−0.003269	0.000000	28.780671
$4p_{3/2}$ (4)	−0.003783	0.000000	24.076118
$4d_{3/2}$ (4)	−0.002061	0.000000	17.968706
$4d_{5/2}$ (6)	−0.002011	0.000000	16.952927
$5s_{1/2}$ (2)	−0.001592	0.000000	6.814810
$4f_{5/2}$ (6)	−0.009943	−0.000001	6.706222
$4f_{7/2}$ (8)	−0.001508	0.000000	6.511731
$5p_{1/2}$ (2)	−0.010017	0.000000	4.507114
$5p_{3/2}$ (4)	−0.009551	0.000000	3.613293
$5d_{3/2}$ (4)	−0.011712	0.000000	1.371634
$5d_{5/2}$ (6)	−0.011344	0.000000	1.238451
$6s_{1/2}$ (2)	−0.100962	0.000001	0.585248
$6p_{1/2}$ (2)	0.188355	0.000000	0.343952
$6p_{3/2}$ (4)	0.167796	0.000000	0.262879
$7s_{1/2}$ (2)	0.012588	−0.000207	−0.169602

Table 5.5. SO splitting of the IPs (in eV) for the outermost p-shells of the pnictogen atoms computed by KT at the KROHF level with the SD-IODKH/NR Hamiltonian. The GS and PGB sets were used for the coupling coefficients. The experimental values are also shown. The values in parentheses represent the energy deviations between the KROHF results and the experimental values.

System	Spinor	GS		PGB		Exptl.*
N	$2p_{1/2}$	4.883	(−9.651)	15.415	(0.880)	14.534
	$2p_{3/2}$	4.905	(−9.635)	15.448	(0.908)	14.540
	Splitting	0.022	(0.016)	0.034	(0.028)	0.006
P	$3p_{1/2}$	4.221	(−6.266)	10.592	(0.105)	10.487
	$3p_{3/2}$	4.277	(−6.268)	10.669	(0.124)	10.545
	Splitting	0.056	(−0.002)	0.077	(0.018)	0.058
As	$4p_{1/2}$	3.908	(−5.881)	9.790	(0.001)	9.789
	$4p_{3/2}$	4.162	(−5.942)	10.134	(0.030)	10.104
	Splitting	0.254	(−0.061)	0.344	(0.029)	0.315
Sb	$5p_{1/2}$	3.503	(−5.105)	8.564	(−0.044)	8.608
	$5p_{3/2}$	4.053	(−5.257)	9.295	(−0.016)	9.310
	Splitting	0.550	(−0.152)	0.730	(0.028)	0.702
Bi	$6p_{1/2}$	2.587	(−6.021)	7.153	(−1.455)	8.608
	$6p_{3/2}$	4.234	(−5.076)	9.360	(0.050)	9.310
	Splitting	1.647	(−0.465)	2.206	(0.094)	2.112

* Ref. [75].

5.3.4 Dependence on coupling coefficients

This subsection discusses the behavior of the various sets of coupling coefficients listed in Table 5.1. Table 5.6 shows a similar analysis to Table 5.4, which is extended to the other (R, D, BPD, MD, FM, and EE) sets. The behaviors of KROHF(R), KROHF(D), KROHF(BPD), KROHF(MD), KROHF(FM), and KROHF(EE) are similar to those of KROHF(GS) and KROHF(PGB). Namely, KROHF calculations using these sets also describe the SO splitting of the spinor energy levels, i.e., $(2j+1)$-fold degeneracies of the spinors. Furthermore, the spinor energies given by these sets approximately correspond to the averages of the pseudo-alpha and pseudo-beta spinor energies of KUHF weighted by the coupling coefficients.

In terms of the deviations from the negative-signed IP/EA values based on the FOA, the behaviors of these sets are similar to that of KROHF(GS). Namely, MaxADs are 188.355 millihartrees for KROHF(R), 100.962 millihartrees for KROHF(D), KROHF(BPD), and KROHF(FM), 240.221 millihartrees for KROHF(MD), and 171.976 millihartrees for KROHF(EE), while 188.355 millihartrees for KROHF(GS) as shown in the previous subsection. Consequently, KROHF(PGB) possesses the lowest MaxAD value (0.207 millihartrees), indicating that KROHF(PGB) gives the most reasonable spinor energies.

Table 5.6. Deviations of the spinor energies of the Bi atom in the ground state computed by KROHF using each coefficient set from the negative-signed IP/EA values under the FOA (in hartrees). The values in parentheses represent degeneracies. Refer to Table 5.4 for the GS and PGB results.

Spinor	R	D	BPD	MD	FM	EE	IP/EA(FOA)
$1s_{1/2}$ (2)	0.001372	−0.001372	−0.001372	−0.000915	−0.001372	−0.001372	3347.284197
$2s_{1/2}$ (2)	0.000783	−0.000783	−0.000783	−0.000522	−0.000783	−0.000783	607.535591
$2p_{1/2}$ (2)	0.001368	−0.001368	−0.001368	−0.000912	−0.001368	−0.001368	546.498140
$2p_{3/2}$ (4)	0.001620	−0.001620	−0.001620	−0.001080	−0.001620	−0.001620	470.446388
$3s_{1/2}$ (2)	0.001362	−0.001362	−0.001362	−0.000908	−0.001362	−0.001362	149.489180
$3p_{1/2}$ (2)	0.001774	−0.001774	−0.001774	−0.001183	−0.001774	−0.001774	129.889199
$3p_{3/2}$ (4)	0.002087	−0.002087	−0.002087	−0.001392	−0.002087	−0.002087	111.612615
$3d_{3/2}$ (4)	0.000928	−0.000928	−0.000928	−0.000619	−0.000928	−0.000928	100.200410
$3d_{5/2}$ (6)	0.000933	−0.000933	−0.000933	−0.000622	−0.000933	−0.000933	95.669485
$4s_{1/2}$ (2)	0.003025	−0.003025	−0.003025	−0.002017	−0.003025	−0.003025	35.836548
$4p_{1/2}$ (2)	0.003269	−0.003269	−0.003269	−0.002179	−0.003269	−0.003269	28.780671
$4p_{3/2}$ (4)	0.003783	−0.003783	−0.003783	−0.002522	−0.003783	−0.003783	24.076118
$4d_{3/2}$ (4)	0.002061	−0.002061	−0.002061	−0.001374	−0.002061	−0.002061	17.968706
$4d_{5/2}$ (6)	0.002011	−0.002011	−0.002011	−0.001341	−0.002011	−0.002011	16.952927
$5s_{1/2}$ (2)	0.001592	−0.001592	−0.001592	−0.001062	−0.001592	−0.001592	6.814810
$4f_{5/2}$ (6)	0.009940	−0.009943	−0.009943	−0.006629	−0.009943	−0.009943	6.706222
$4f_{7/2}$ (8)	0.001508	−0.001508	−0.001508	−0.001005	−0.001508	−0.001508	6.511731
$5p_{1/2}$ (2)	0.010017	−0.010017	−0.010017	−0.006678	−0.010017	−0.010017	4.507114
$5p_{3/2}$ (4)	0.009551	−0.009551	−0.009551	−0.006367	−0.009551	−0.009551	3.613293
$5d_{3/2}$ (4)	0.011712	−0.011712	−0.011712	−0.007808	−0.011712	−0.011712	1.371634
$5d_{5/2}$ (6)	0.011344	−0.011344	−0.011344	−0.007563	−0.011344	−0.011344	1.238451
$6s_{1/2}$ (2)	0.100966	−0.100962	−0.100962	−0.067308	−0.100962	−0.100962	0.585248
$6p_{1/2}$ (2)	0.188355	0.000000	0.000000	0.240221	0.000000	0.171976	0.343952
$6p_{3/2}$ (4)	0.167796	0.000000	0.000000	0.199490	0.000000	0.131440	0.262879
$7s_{1/2}$ (2)	−0.013431	−0.000207	0.024976	0.008369	0.012588	0.012588	−0.169602

Figure 5.2 shows the first IPs of the free atoms H to Lr computed by KROHF using each set of coupling coefficients with the SD-IODKH/NR Hamiltonian. Each point corresponds to the result for each atom. The horizontal and vertical axes indicate the IPs calculated through KT and FOA, respectively. The slopes and correlation coefficients (R^2) based on the least squares method are also shown in each graph of Figure 5.2. A point on the 45° line, or slope equaling one, shows good agreement with KT.

As seen in the above paragraph, KROHF(PGB) shows the physically best results of all the sets. Namely, both the slope and R^2 values are 1.000. Similar behaviors are observed in KROHF(D), KROHF(BPD), and KROHF(FM), although the values of the slope and R^2 are slightly smaller than those of KROHF(PGB). In KROHF(GS), KROHF(R), KROHF(MD), and KROHF(EE), there exist two groups on the plots; each group has distinct values of the slope and R^2. The group of slopes equaling 1.000 corresponds to the results of closed-shell structures, while the other group corresponds to the open-shell structures. Namely, KROHF(GS), KROHF(R), KROHF(MD), and KROHF(EE) correctly describe the behaviors of only the closed-shell structures, while they give unphysical spinor energies to the open-shell structures.

The values of the slope and R^2 can be explained from the viewpoint of spinor energies being represented by the weighted averages of KUHF spinor energies through the coupling coefficients. The open-shell groups in KROHF(GS), KROHF(R), and KROHF(EE) have slope values that are close to two. In KROHF(MD), the slope value of the open-shell group is approximately three. These slopes reflect the reciprocal of the coupling coefficient for the pseudo-alpha open-shell part, A_{OO}. This is also the case with KROHF(D), KROHF(BPD), KROHF(FM), and KROHF(PGB).

The dispersion of the plots, i.e., a small value of R^2, is observed in the open-shell

groups of KROHF(GS), KROHF(R), and KROHF(MD), while the others have R^2 values close to one. This reflects the numerical contamination of the pseudo-alpha spinor energies with the pseudo-beta spinor energies, i.e., non-zero values of the coupling coefficients for the pseudo-beta open-shell part, B_{OO}. Consequently, the values of the slope and R^2 close to one, i.e., the good descriptions of the first IPs in KROHF(D), KROHF(BPD), KROHF(FM), and KROHF(PGB) are derived from $\left(A_{\mathrm{OO}}, B_{\mathrm{OO}}\right) = \left(1, 0\right)$.

As mentioned above, the points corresponding to the closed-shell structures are on the 45° line for all sets of coupling coefficients. This is because KROHF is equivalent to KRHF, which satisfies KT, for these points. However, it should be noted that KROHF is not always equivalent to KRHF in closed-shell cases. The necessary and sufficient condition in KROHF to reproduce the KRHF spinor energies is

$$\left(A_{\mathrm{CC}} + B_{\mathrm{CC}} = 1\right) \wedge \left(A_{\mathrm{VV}} + B_{\mathrm{VV}} = 1\right), \tag{5.25}$$

as discussed by Glaesemann and Schmidt [76] for ROHF. This condition normalizes the Fock matrix when assembled in the KROHF procedure, and consequently gives the normalized spinor energies. All the sets of coupling coefficients adopted here satisfy Eq. (5.25).

At the end of this chapter, let us discuss SCF convergence of KROHF. Here, the 29 d- and 30 f-block atoms are adopted as test systems because of their SCF convergence difficulties observed in SD relativistic calculations as seen in the previous study by the author and co-workers [44]. Table 5.7 shows the SCF convergence properties of KROHF using each set of coupling coefficients from Table 5.1. The KUHF and GHF results are also shown for comparison. The table includes the average number of cycles required to achieve SCF convergence (Average), where the elements unconverged within 1000 cycles

are excluded. The number of elements that failed to converge within 1000 cycles is tabulated under #Failure.

As seen in the previous chapter, KUHF shows better SCF convergence behavior than GHF for both d- and f-block elements. From the viewpoint of both Average and #Failure, KROHF(GS) also shows better convergence behavior than GHF for both d- and f-block elements. This is because, in KROHF, the introduction of time-reversal symmetry suppresses the spin degrees of freedom, which are the main source of the convergence difficulties in SD relativistic calculations. However, the efficacy of KROHF(GS) for SCF convergence is inferior to that of KUHF. This is affected by the higher symmetry of the KROHF wavefunction than the KUHF wavefunction. A similar situation appears in the ROHF and UHF calculations. Consequently, both tight and loose symmetry constraints on spin lead to poor SCF convergence behavior.

KROHF(R) shows a similar convergence behavior to KROHF(GS); KROHF(R) is superior in Average but inferior in #Failure. The convergence behavior of KROHF(MD) is also relatively similar to that of KROHF(GS) but worse from the viewpoint of both Average and #Failure. The behavior of KROHF(MD) is rather close to that of GHF.

On the other hand, #Failure of KROHF using the other sets, i.e., KROHF(D), KROHF(BPD), KROHF(FM), KROHF(EE), and KROHF(PGB), are much larger; in particular, the values range from 12 to 18 for f-block systems. This reflects the poorer convergence behavior of these sets. The common point of these sets is that they have zero values in the coupling coefficients, while the GS, R, and MD sets do not. The existence of the zero values in the coupling coefficients would make convergence of KROHF worse. Hence, it is suggested that the GS set is the most useful from the viewpoint of stable convergence behavior. From the physical point of view, however, the PGB set should be

adopted.

Then, as a simple remedy, the following scheme is available. First, a KROHF(GS) calculation is performed. After the calculation converges, the coupling coefficients of the GS set are replaced with the PGB set. Here, this scheme is denoted as KROHF(GS→PGB). In the KROHF(GS→PGB) scheme, the additional KROHF(PGB) calculation converges within one or two SCF cycles. The average values are 151.8 and 212.4 for the d- and f-block systems, respectively. This scheme is reasonable because the variational problems of the KROHF(GS) and KROHF(PGB) are defined on the common HF manifold as described in the previous section. In fact, KROHF(GS→PGB) gives the same spinor energies as the original KROHF(PGB) calculations within the given criterion for SCF convergence. This scheme is, of course, also available in the other sets as well as the PGB set. Furthermore, this approach is effective even in ROHF calculations. Actually, a similar approach is adopted by Tsuchimochi and Scuseria [16] in their NR study. In conclusion, the order of the facility in SCF convergence is written as

$$\begin{aligned} \mathrm{KUHF} &\geq \mathrm{KROHF(GS)} \approx \mathrm{KROHF(GS \rightarrow PGB)} \\ &\geq \mathrm{KROHF(R)} \geq \mathrm{GHF} \geq \mathrm{KROHF(the\ other\ sets)}. \end{aligned} \tag{5.26}$$

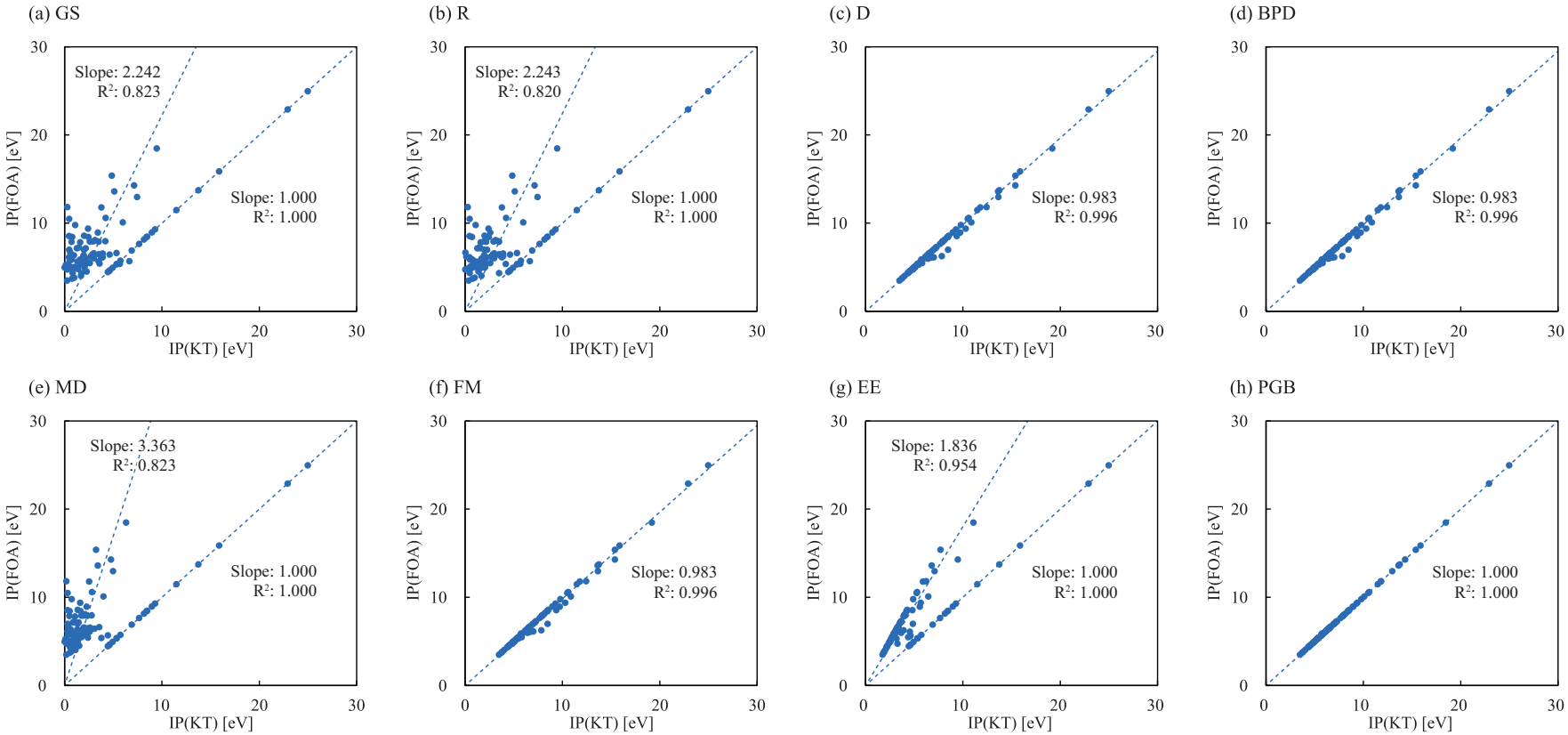

Figure 5.2. Comparison of the KT and FOA results for the first IPs of the free atoms from H to Lr calculated by KROHF using each set of coupling coefficients. Also shown are the values of slopes and correlation coefficients (R^2) based on the least squares analysis.

Table 5.7. SCF convergence properties of KROHF with each coefficient set, KUHF, and GHF for 29 d- and 30 f-block atoms using the SD-IODKH/NR Hamiltonian. Average indicates the average number of cycles to achieve SCF convergence, where elements unconverged within 1000 cycles are excluded. #Failure shows the number of the elements unconverged within 1000 cycles.

System	KROHF								KUHF	GHF
	GS	R	D	BPD	MD	FM	EE	PGB		
d-Block										
Average	150.8	93.8	29.0	29.1	157.0	32.1	77.7	131.4	108.1	173.9
#Failure	0	2	13	13	2	14	1	13	1	2
f-Block										
Average	211.4	182.4	269.4	197.5	288.0	237.4	319.6	190.5	78.8	285.8
#Failure	2	4	17	18	6	17	12	16	0	4

5.4 Conclusion

In this chapter, an open-shell HF theory for SD two-component relativistic calculations, termed KROHF, has been developed. The present KROHF method is formulated as a relativistic analogue of ROHF: KROHF is based on KUHF (proposed in the previous chapter), adopts quaternion algebra, and satisfies time-reversal symmetry, while ROHF is based on UHF, adopts real algebra, and satisfies spin restriction. Furthermore, the canonical ROHF procedure by Plakhutin and his co-workers (PGB), which satisfies KT and Brillouin's theorem, has been extended to the present KROHF theory; the coupling coefficients for the construction of the KROHF Fock matrix have been derived.

The total energies of the pnictogen atoms were first calculated to examine the KROHF method. KROHF gives reasonable but higher total energies in comparison with KUHF and GHF, reflecting the higher symmetry of the KROHF wavefunction. The choice of the coupling coefficients is confirmed not to affect the total energies in KROHF.

Then, the spinor energies for the pnictogen atoms were investigated. It was confirmed that KROHF(PGB) gives physically reasonable spinor energies, which agree well with KT, i.e., the negative-signed spinor energies of KROHF(PGB) are in good agreement with the IP and EA values, while KROHF(GS) does not. The spinor energies given by KROHF(PGB) also describe the effects of SO interactions well.

Furthermore, the behaviors of the various sets of coupling coefficients (including the GS and PGB sets) were discussed. The spinor energies for the Bi atom and the first IP values for H through Lr atoms were investigated. The behaviors of the spinor energies given by each set are well described by the weighted averages of the pseudo-alpha and pseudo-beta KUHF spinor energies through the coupling coefficients. In consequence,

the PGB sets gave the physically best results of all the sets.

Finally, the SCF convergence behavior of KROHF was compared with KUHF and GHF. In KROHF(GS), the SCF convergence behavior is better than GHF but worse than KUHF. In contrast, most of the schemes including KROHF(PGB) show poorer convergence behavior than GHF. The KROHF(GS→PGB) approach, which changes the coupling coefficients, works as a simple remedy to complement the poor SCF convergence behaviors of KROHF(PGB) and the other schemes.

References

[1] J. A. Pople, R. K. Nesbet, *J. Chem. Phys.* **22**, 571 (1954).

[2] C. C. J. Roothaan, *Rev. Mod. Phys.* **32**, 179 (1960).

[3] G. G. Dyadyusha, V. A. Kuprievich, *Theor. Exp. Chem.* **1**, 262 (1965).

[4] K. Hirao, H. Nakatsuji, *J. Chem. Phys.* **59**, 1457 (1973).

[5] B. N. Plakhutin, *J. Struct. Chem.* **55**, 1001 (2014).

[6] R. Carbo, J. M. Riera, A General SCF Theory, Springer, Berlin, 1978.

[7] B. N. Plakhutin, E. R. Davidson, *J. Chem. Phys.* **140**, 014102 (2014).

[8] B. N. Plakhutin, E. V. Gorelik, N. N. Breslavskaya, *J. Chem. Phys.* **125**, 204110 (2006).

[9] B. N. Plakhutin, E. R. Davidson, *J. Phys. Chem. A* **113**, 12386 (2009).

[10] E. R. Davidson, B. N. Plakhutin, *J. Chem. Phys.* **132**, 184110 (2010).

[11] T. A. Koopmans, *Physica (Utrecht)* **1**, 104 (1934).

[12] J. S. Andrews, D. Jayatilaka, R. G. A. Bone, N. C. Handy, R. D. Amos, *Chem. Phys. Lett.* **183**, 423 (1991).

[13] R. D. Amos, J. S. Andrews, N. C. Handy, P. J. Knowles, *Chem. Phys. Lett.* **185**, 256 (1991).

[14] P. J. Knowles, J. S. Andrews, R. D. Amos, N. C. Handy, J. A. Pople, *Chem. Phys. Lett.* **186**, 130 (1991).

[15] W. J. Lauderdale, J. F. Stanton, J. Gauss, J. D. Watts, R. J. Bartlett, *Chem. Phys. Lett.* **187**, 21 (1991).

[16] T. Tsuchimochi, G. E. Scuseria, *J. Chem. Phys.* **133**, 141102 (2010).

[17] A. V. Luzanov, Y. F. Pedash, *J. Struct. Chem.* **27**, 510 (1986).

[18] V. N. Glushkov, *Int. J. Quantum Chem.* **99**, 236 (2004).

[19] R. E. Moss, Advanced Molecular Quantum Mechanics: An Introduction to Relativistic Quantum Mechanics and the Quantum Theory of Radiation, Chapman and Hall, London, 1973.

[20] L. L. Foldy, S. A. Wouthuysen, *Phys. Rev.* **78**, 29 (1950).

[21] M. Douglas, N. M. Kroll, *Ann. Phys. (Leipzig)* **82**, 89 (1974).

[22] B. A. Hess, *Phys. Rev. A* **32**, 756 (1985).

[23] E. van Lenthe, E. J. Baerends, J. G. Snijders, *J. Chem. Phys.* **99**, 4597 (1993).

[24] S. Faas, J. G. Snijders, J. H. van Lenthe, E. van Lenthe, E. J. Baerends, *Chem. Phys. Lett.* **246**, 632 (1995).

[25] R. Samzow, B. A. Hess, G. Jansen, *J. Chem. Phys.* **96**, 1227 (1992).

[26] K. G. Dyall, *J. Chem. Phys.* **106**, 9618 (1997).

[27] T. Nakajima, K. Hirao, *J. Chem. Phys.* **113**, 7786 (2000).

[28] A. Wolf, M. Reiher, B. A. Hess, *J. Chem. Phys.* **117**, 9215 (2002).

[29] M. Barysz, A. J. Sadlej, *J. Chem. Phys.* **116**, 2696 (2002).

[30] C. van Wüllen, C. Michauk, *J. Chem. Phys.* **123**, 204113 (2005).

[31] D. Peng, W. Liu, Y. Xiao, L. Cheng, *J. Chem. Phys.* **127**, 104106 (2007).

[32] J. Sikkema, L. Visscher, T. Saue, M. Iliaš, *J. Chem. Phys.* **131**, 124116 (2009).

[33] W. Liu, *Mol. Phys.* **108**, 1679 (2010).

[34] R. Seeger, J. A. Pople, *J. Chem. Phys.* **66**, 3045 (1977).

[35] H. Fukutome, *Int. J. Quantum Chem.* **20**, 955 (1981).

[36] J.-L. Calais, *Adv. Quantum Chem.* **17**, 225 (1985).

[37] R. McWeeny, Methods of Molecular Quantum Mechanics, Academic Press, London, 1989.

[38] P.-O. Löwdin, I. Mayer, *Adv. Quantum Chem.* **24**, 79 (1992).

[39] S. Hammes-Schiffer, H. C. Andersen, *J. Chem. Phys.* **99**, 1901 (1993).

[40] S. K. Wolff, D. Jayatilaka, G. S. Chandler, *J. Chem. Phys.* **103**, 4562 (1995).

[41] D. Jayatilaka, *J. Chem. Phys.* **108**, 7587 (1998).

[42] J. L. Stuber, J. Paldus, in: E. J. Brändas, E. S. Kryachko (Eds.), Fundamental World of Quantum Chemistry, Kluwer Academic Publishers, Dordrecht, 2003, p. 67.

[43] M. K. Armbruster, F. Weigend, C. van Wüllen, W. Klopper, *Phys. Chem. Chem. Phys.* **10**, 1748 (2008).

[44] M. Nakano, J. Seino, H. Nakai, *Chem. Phys. Lett.* **657**, 65 (2016).

[45] M. Nakano, J. Seino, H. Nakai, *Int. J. Quantum Chem.* **117**, e25356 (2017).

[46] A. Rosen, D. E. Ellis, *J. Chem. Phys.* **62**, 3039 (1975).

[47] D. E. Ellis, G. L. Goodman, *Int. J. Quantum Chem.* **25**, 185 (1984).

[48] F. Wang, W. Liu, *J. Chin. Chem. Soc.* **50**, 597 (2003).

[49] P. Hafner, W. H. E. Schwarz, *Chem. Phys. Lett.* **65**, 537 (1979).

[50] P. Hafner, *J. Phys. B: At., Mol. Opt. Phys.* **13**, 3297 (1980).

[51] N. Rösch, *Chem. Phys.* **80**, 1 (1983).

[52] S. Y. Lee, Y. S. Lee, *J. Comput. Chem.* **13**, 595 (1992).

[53] O. Visser, P. J. C. Aerts, L. Visscher, in: S. Wilson, I. P. Grant, B. L. Gyorffy (Eds.), The Effects of Relativity in Atoms, Molecules, and the Solid State, Springer, Plenum Press, 1991, p. 185.

[54] K. G. Dyall, *Chem. Phys. Lett.* **224**, 186 (1994).

[55] J. Thyssen, Development and Applications of Methods for Correlated Relativistic Calculations of Molecular Properties. Ph.D. Thesis, University of Southern Denmark, Odense, April 2001.

[56] M. F. Guest, V. R. Saunders, *Mol. Phys.* **28**, 819 (1974).

[57] E. R. Davidson, *Chem. Phys. Lett.* **21**, 565 (1973).

[58] J. S. Binkley, J. A. Pople, P. A. Dobosh, *Mol. Phys.* **28**, 1423 (1974).

[59] R. McWeeny, G. Diercksen, *J. Chem. Phys.* **49**, 4852 (1968).

[60] J. K. Fægri, R. Manne, *Mol. Phys.* **31**, 1037 (1976).

[61] V. Fock, *Z. Phys.* **61**, 126 (1930).

[62] G. T. Klimko, M. M. Mestechkin, B. N. Plakhutin, G. M. Zhidomirov, R. A. Evarestov, *Int. J. Quantum Chem.* **37**, 35 (1990).

[63] B. N. Plakhutin, G. M. Zhidomirov, A. V. Arbuznikov, *Int. J. Quantum Chem.* **41**, 311 (1992).

[64] B. N. Plakhutin, in: K. D. Sen (Ed.), Reviews of Modern Quantum Chemistry, World Scientific, Singapore, 2002, p. 16.

[65] I. H. Hillier, V. R. Saunders, *Int. J. Quantum Chem.* **4**, 503 (1970).

[66] L. N. Brillouin, *J. Phys. Radium* **5**, 413 (1934).

[67] J. J. Dongarra, J. R. Gabriel, D. D. Koelling, J. H. Wilkinson, *J. Comput. Phys.* **54**, 278 (1984).

[68] J. J. Dongarra, J. R. Gabriel, D. D. Koelling, J. H. Wilkinson, *Linear Algebra Appl.* **60**, 27 (1984).

[69] T. Koga, H. Tatewaki, T. Shimazaki, *Chem. Phys. Lett.* **328**, 473 (2000).

[70] Y. Osanai, T. Noro, E. Miyoshi, M. Sekiya, T. Koga, *J. Chem. Phys.* **120**, 6408 (2004).

[71] P. Pulay, *Chem. Phys. Lett.* **73**, 393 (1980).

[72] P. Pulay, *J. Comput. Chem.* **3**, 556 (1982).

[73] K. N. Kudin, G. E. Scuseria, E. Cancès, *J. Chem. Phys.* **116**, 8255 (2002).

[74] P. Lykos, G. W. Pratt, *Rev. Mod. Phys.* **35**, 496 (1963).

[75] NIST, Atomic Spectra Database. http://www.nist.gov/pml/data/asd.cfm (accessed

November 1, 2016).

[76] K. R. Glaesemann, M. W. Schmidt, *J. Phys. Chem. A* **114**, 8772 (2010).

Chapter 6

Generalized second-order Møller–Plesset perturbation theory for many-electron two-component relativistic Hamiltonian

6.1 Introduction

To accurately describe the electronic structure of molecules including heavy elements, relativistic and electron correlation effects are indispensable. Accurate standards for modern relativistic quantum chemical calculations are established on the four-component DC or DCB Hamiltonians, which consist of the one-particle Dirac operator and the electron-electron Coulomb or Breit interactions. The four-component method considers both electronic and positronic states. By decoupling the positronic states from the four-component framework, a wide variety of two-component methods, which are computationally more efficient, have been developed. For details and the history of the two-component methods, see the review articles by Liu [1] and Saue [2].

The two-component Hamiltonians are divided into four contributions: the SF and SD parts of the one- and two-electron terms. In many quantum chemical program packages, only the SF one-electron terms are considered because typical NR codes are available with small modifications. Namely, the real-valued formalism using the NR two-electron Coulomb interaction can be applied by replacing the NR one-electron integrals with the SF relativistic one-electron integrals. However, the other relativistic contributions are also important in heavy-element systems.

To include the relativistic two-electron terms, two methodological approaches are

available: the operator and matrix formulations [1]. In the operator formulations, the analytical two-component electronic Hamiltonian is first derived, and the matrix representation of the Hamiltonian is then constructed. Most analytical two-component many-electron Hamiltonians have been derived using the free-particle FW or DKH transformations for the four-component DC Hamiltonian [3-8]. Although these methods require unitary transformations for two-electron integrals, whose computational scaling is $O(n^5)$ with the basis set dimension n, the two-electron LUT scheme, i.e., an extension of local treatment for the relativistic one-electron terms [9,10], reduces the computational cost to $O(n)$ [11]. In contrast, the matrix formulations start from the matrix representation of the four-component DC Hamiltonian, and the algebraic two-component many-electron Hamiltonian is then constructed [12-16]. The matrix formulations avoid the explicit treatment of the complicated two-component operators, although the evaluation of the four-component matrix elements increases the computational prefactor. Mostly, these methodological approaches have been discussed at the HF level of theory for the relativistic two-electron interactions; there has been less discussion at the post-HF level of theory [12].

For the inclusion of the SD terms such as the SO interaction, there are two types of approximate treatment. One type introduces the SD effects as a post-treatment to the NR or SF relativistic calculations using either perturbation theory or the CI method [17,18]. Another type is based on the approximate representation of the SD two-electron operators. For example, in the atomic mean-field approach [19], the effective SD one-electron Hamiltonian is constructed by averaging the two-electron contributions. The screened nuclear SO approximation [20] and the flexible nuclear screening SO approximation [21] avoid the explicit evaluation of the SD two-electron integrals by using simplified physical

models that mimic the SD two-electron effects. Both types of approximate treatment can be used in combination.

For a rigorous approach on the SD terms, a self-consistent treatment based on the GHF method [22-31], where any symmetry constraints are removed, has been used. This is because the spin symmetry of the SD relativistic wavefunction is generally broken due to the non-commutativity of the SD relativistic Hamiltonian with spin operators. Furthermore, two-component post-HF methods, which use the GHF wavefunction as a reference state, have also been developed, such as the GMP2 method [32-35] and the generalized CC theories [36-40]. However, these methods are limited to the treatment of the lower-order SD two-electron relativistic corrections.

In this chapter, a general formulation of the GMP2 method in accordance with the analytical SD two-component relativistic many-electron Hamiltonians has been derived to describe the full relativistic effects within the DC framework. Based on the general formulation, the author has implemented the GMP2 code for the IODKH Hamiltonian for many-electron systems, denoted as IODKH/IODKH, which is one of the most accurate two-component many-electron Hamiltonians. Furthermore, the significance of the two-electron relativistic effect has been examined as well as the SD treatment. This chapter is organized as follows: Theory and implementation are explained in Sec. 6.2. In Sec. 6.3, the present GMP2 method is numerically assessed for atomic and molecular systems. Finally, in Sec. 6.4, concluding remarks are presented.

6.2 Theory and implementation

6.2.1 GMP2 method

The GMP2 method is one of the fundamental electron correlation theories, which uses the GHF wavefunction as a reference state. In the GHF-based method, GSOs are defined by the superposition of AOs for alpha- and beta-spins,

$$\varphi_i = \sum_{\omega}^{\{\alpha,\beta\}} \sum_{\mu}^{\{\mathrm{AO}\}} C_{\mu i}^{\sigma} \chi_{\mu}^{\sigma} \omega, \tag{6.1}$$

where χ denotes the AOs (labeled by Greek letters), C the complex MO coefficients, and ω the spin functions. Note that the spin degrees of freedom are not integrated out in Eq. (6.1).

The GMP2 correlation energy for the general two-component Hamiltonian in Eq. (2.11) is given by

$$E_{\mathrm{corr}}^{\mathrm{GMP2}} = -\frac{1}{4} \sum_{ij}^{\{\mathrm{occ}\}} \sum_{ab}^{\{\mathrm{vir}\}} \frac{\left| \left(ia\middle|g_{12}\middle|jb\right) - \left(ib\middle|g_{12}\middle|ja\right) \right|^2}{\varepsilon_a + \varepsilon_b - \varepsilon_i - \varepsilon_j}, \tag{6.2}$$

where i, j and a, b refer to occupied and virtual orbitals, respectively [32]. The two-electron integrals in the MO basis are constructed from the corresponding AO integrals via a four-index transformation,

$$\left(ia\middle|g_{12}\middle|jb\right) = \sum_{\omega\omega'\tau\tau'}^{\{\alpha,\beta\}} \sum_{\mu\nu\rho\lambda}^{\{\mathrm{AO}\}} \left(C_{\mu i}^{\omega}\right)^* C_{\nu a}^{\omega'} \left(C_{\rho j}^{\tau}\right)^* C_{\lambda b}^{\tau'} \left[\mu\omega\ \nu\omega'\middle|g_{12}\middle|\rho\tau\ \lambda\tau'\right], \tag{6.3}$$

where $\{\omega, \omega'\}$ and $\{\tau, \tau'\}$ denote the spin functions for electrons 1 and 2, respectively. Here, the so-called chemists' notation is used.

In this chapter, programmable expressions of the four-index transformation have been derived for the general two-component two-electron operators in Eq. (2.14). For each operator in Eq. (2.14), Eq. (6.3) is factorized into spatial and spin parts as follows:

$$\left(ia\left|g_{12}\right|jb\right)=\sum_{\omega\omega'\tau\tau'}^{\{\alpha,\beta\}}\sum_{\mu\nu\rho\lambda}^{\{\mathrm{AO}\}}\sum_{\xi_1\xi_2}^{\{x,y,z\}}\left(C_{\mu i}^{\omega}\right)^{*}C_{\nu a}^{\omega'}\left(C_{\rho j}^{\tau}\right)^{*}C_{\lambda b}^{\tau'}$$
$$\left(\mu\nu\left|\Xi_{12}^{\xi_1\xi_2}\right|\rho\lambda\right)\left\langle\omega\left|\Theta_1^{\xi_1}\right|\omega'\right\rangle\left\langle\tau\left|\Theta_2^{\xi_2}\right|\tau'\right\rangle, \tag{6.4}$$

where Ξ and Θ are the spatial and spin parts of the two-electron operators, respectively, and ξ_1 and ξ_2 denote *x*, *y*, or *z* directions. For g_{12}^{SF}, Ξ and Θ are defined as

$$\Xi_{12}^{\xi_1\xi_2}=g_{12}^{\mathrm{SF}} \tag{6.5}$$

and

$$\Theta_1^{\xi_1}=\Theta_2^{\xi_2}=\frac{1}{3}; \tag{6.6}$$

for g_{12}^{SD1},

$$\Xi_{12}^{\xi_1\xi_2}=\Omega_1^{\xi_1}\left(X_{12}\right), \tag{6.7}$$

$$\Theta_1^{\xi_1}=\sigma_1^{\xi_1}, \tag{6.8}$$

and

$$\Theta_2^{\xi_2}=\frac{1}{3}; \tag{6.9}$$

for g_{12}^{SD2},

$$\Xi_{12}^{\xi_1\xi_2}=\Omega_2^{\xi_2}\left(X_{12}\right), \tag{6.10}$$

$$\Theta_1^{\xi_1}=\frac{1}{3}, \tag{6.11}$$

and

$$\Theta_2^{\xi_2}=\sigma_1^{\xi_2}; \tag{6.12}$$

and for g_{12}^{SD3},

$$\Xi_{12}^{\xi_1\xi_2} = \Omega_1^{\xi_1}\left(\Omega_2^{\xi_2}\left(X_{12}\right)\right), \tag{6.13}$$

$$\Theta_1^{\xi_1} = \sigma_1^{\xi_1}, \tag{6.14}$$

and

$$\Theta_2^{\xi_2} = \sigma_1^{\xi_2}. \tag{6.15}$$

The factors, $1/3$, in Eqs. (6.6), (6.9), and (6.11) are introduced to normalize the summation over the direction ξ. By performing spin integration in Eq. (6.4), the programmable forms of the transformation are obtained. Table 6.1 summarizes the formulae of the transformation for each operator using the ladder-like operator defined as

$$\Omega^{\pm} = \Omega^x \pm i\Omega^y. \tag{6.16}$$

The spin pairs in the rows and columns indicate the spin components for electron 1 (ω and ω') and electron 2 (τ and τ'), respectively. Each cell shows the non-zero spatial components of the operators. For example, for the g_{12}^{SD1} type operator, Eq. (6.4) is

$$\begin{aligned}
&\left(ia\left|g_{12}^{\mathrm{SD1}}\right|jb\right) \\
&= \sum_{\omega\omega'\tau\tau'}^{\{\alpha,\beta\}} \sum_{\mu\nu\rho\lambda}^{\{\mathrm{AO}\}} \sum_{\xi_1\xi_2}^{\{x,y,z\}} \left(C_{\mu i}^{\omega}\right)^* C_{\nu a}^{\omega'} \left(C_{\rho j}^{\tau}\right)^* C_{\lambda b}^{\tau'} \left(\mu\nu\left|\Omega_1^{\xi_1}\left(X_{12}\right)\right|\rho\lambda\right)\left\langle\omega\left|\sigma_1^{\xi_1}\right|\omega'\right\rangle\left\langle\tau\left|\frac{1}{3}\right|\tau'\right\rangle \\
&= \sum_{\omega\omega'\tau\tau'}^{\{\alpha,\beta\}} \sum_{\mu\nu\rho\lambda}^{\{\mathrm{AO}\}} \sum_{\xi_1}^{\{x,y,z\}} \left(C_{\mu i}^{\omega}\right)^* C_{\nu a}^{\omega'} \left(C_{\rho j}^{\tau}\right)^* C_{\lambda b}^{\tau'} \left(\mu\nu\left|\Omega_1^{\xi_1}\left(X_{12}\right)\right|\rho\lambda\right)\left\langle\omega\left|\sigma_1^{\xi_1}\right|\omega'\right\rangle \delta_{\tau\tau'},
\end{aligned} \tag{6.17}$$

where δ is the Kronecker delta. Assuming $\left(\omega,\omega',\tau,\tau'\right) = \left(\alpha,\alpha,\alpha,\alpha\right)$, the spatial and spin factors in Eq. (6.17) become

$$\begin{aligned}
&\sum_{\xi_1}^{\{x,y,z\}} \left(\mu\nu\left|\Omega_1^{\xi_1}\left(X_{12}\right)\right|\rho\lambda\right)\left\langle\omega\left|\sigma_1^{\xi_1}\right|\omega'\right\rangle \delta_{\tau\tau'} \\
&= \sum_{\xi_1}^{\{x,y,z\}} \left\{\left(\mu\nu\left|\Omega_1^{x}\left(X_{12}\right)\right|\rho\lambda\right)\left\langle\alpha\left|\sigma_1^{x}\right|\alpha\right\rangle + \left(\mu\nu\left|\Omega_1^{y}\left(X_{12}\right)\right|\rho\lambda\right)\left\langle\alpha\left|\sigma_1^{y}\right|\alpha\right\rangle \right. \\
&\quad \left. + \left(\mu\nu\left|\Omega_1^{z}\left(X_{12}\right)\right|\rho\lambda\right)\left\langle\alpha\left|\sigma_1^{z}\right|\alpha\right\rangle\right\}.
\end{aligned} \tag{6.18}$$

By substituting $\alpha = \begin{pmatrix} 1 & 0 \end{pmatrix}^{\dagger}$ and the definitions of the Pauli matrices [Eqs. (2.5)–(2.7)], the first and second terms in Eq. (6.18) vanish. Consequently, the $(\omega, \omega', \tau, \tau') = (\alpha, \alpha, \alpha, \alpha)$ contribution to the MO integral results in

$$+\sum_{\mu\nu\rho\lambda}^{\{\mathrm{AO}\}} \left(C_{\mu i}^{\alpha}\right)^{*} C_{\nu a}^{\alpha} \left(C_{\rho j}^{\alpha}\right)^{*} C_{\lambda b}^{\alpha} \left(\mu\nu \middle| \Omega_{1}^{z}\left(X_{12}\right) \middle| \rho\lambda\right), \tag{6.19}$$

as in the top-left cell of row g_{12}^{SD1} in Table 6.1. In the same manner, the $(\omega, \omega', \tau, \tau') = (\alpha, \alpha, \alpha, \beta)$ contribution of g_{12}^{SD1} is 0, as in the next cell, because $\delta_{\tau\tau'} = \delta_{\alpha\beta} = 0$ in Eq. (6.17).

Table 6.1. Summary of the formulae for the four-index transformation. α and β in the rows and columns correspond to the spin components for electrons 1 and 2, respectively. Each cell shows the non-zero component of the spatial part of the operators, where X_{12} is omitted for simplicity.

Operator	Spin for elec. 1	Spin for elec. 2			
		$\alpha\alpha$	$\alpha\beta$	$\beta\alpha$	$\beta\beta$
g_{12}^{SF}	$\alpha\alpha$	$+\left(\mu\nu\middle\|g_{12}^{\mathrm{SF}}\middle\|\rho\lambda\right)$	0	0	$+\left(\mu\nu\middle\|g_{12}^{\mathrm{SF}}\middle\|\rho\lambda\right)$
	$\alpha\beta$	0	0	0	0
	$\beta\alpha$	0	0	0	0
	$\beta\beta$	$+\left(\mu\nu\middle\|g_{12}^{\mathrm{SF}}\middle\|\rho\lambda\right)$	0	0	$+\left(\mu\nu\middle\|g_{12}^{\mathrm{SF}}\middle\|\rho\lambda\right)$
g_{12}^{SD1}	$\alpha\alpha$	$+\left(\mu\nu\middle\|\Omega_1^z\middle\|\rho\lambda\right)$	0	0	$+\left(\mu\nu\middle\|\Omega_1^z\middle\|\rho\lambda\right)$
	$\alpha\beta$	$+\left(\mu\nu\middle\|\Omega_1^-\middle\|\rho\lambda\right)$	0	0	$+\left(\mu\nu\middle\|\Omega_1^-\middle\|\rho\lambda\right)$
	$\beta\alpha$	$+\left(\mu\nu\middle\|\Omega_1^+\middle\|\rho\lambda\right)$	0	0	$+\left(\mu\nu\middle\|\Omega_1^+\middle\|\rho\lambda\right)$
	$\beta\beta$	$-\left(\mu\nu\middle\|\Omega_1^z\middle\|\rho\lambda\right)$	0	0	$-\left(\mu\nu\middle\|\Omega_1^z\middle\|\rho\lambda\right)$
g_{12}^{SD2}	$\alpha\alpha$	$+\left(\mu\nu\middle\|\Omega_2^z\middle\|\rho\lambda\right)$	$+\left(\mu\nu\middle\|\Omega_2^-\middle\|\rho\lambda\right)$	$+\left(\mu\nu\middle\|\Omega_2^+\middle\|\rho\lambda\right)$	$-\left(\mu\nu\middle\|\Omega_2^z\middle\|\rho\lambda\right)$
	$\alpha\beta$	0	0	0	0
	$\beta\alpha$	0	0	0	0
	$\beta\beta$	$+\left(\mu\nu\middle\|\Omega_2^z\middle\|\rho\lambda\right)$	$+\left(\mu\nu\middle\|\Omega_2^-\middle\|\rho\lambda\right)$	$+\left(\mu\nu\middle\|\Omega_2^+\middle\|\rho\lambda\right)$	$-\left(\mu\nu\middle\|\Omega_2^z\middle\|\rho\lambda\right)$
g_{12}^{SD3}	$\alpha\alpha$	$+\left(\mu\nu\middle\|\Omega_1^z(\Omega_2^z)\middle\|\rho\lambda\right)$	$+\left(\mu\nu\middle\|\Omega_1^z(\Omega_2^-)\middle\|\rho\lambda\right)$	$+\left(\mu\nu\middle\|\Omega_1^z(\Omega_2^+)\middle\|\rho\lambda\right)$	$-\left(\mu\nu\middle\|\Omega_1^z(\Omega_2^z)\middle\|\rho\lambda\right)$
	$\alpha\beta$	$+\left(\mu\nu\middle\|\Omega_1^-(\Omega_2^z)\middle\|\rho\lambda\right)$	$+\left(\mu\nu\middle\|\Omega_1^-(\Omega_2^-)\middle\|\rho\lambda\right)$	$+\left(\mu\nu\middle\|\Omega_1^-(\Omega_2^+)\middle\|\rho\lambda\right)$	$-\left(\mu\nu\middle\|\Omega_1^-(\Omega_2^z)\middle\|\rho\lambda\right)$
	$\beta\alpha$	$+\left(\mu\nu\middle\|\Omega_1^+(\Omega_2^z)\middle\|\rho\lambda\right)$	$+\left(\mu\nu\middle\|\Omega_1^+(\Omega_2^-)\middle\|\rho\lambda\right)$	$+\left(\mu\nu\middle\|\Omega_1^+(\Omega_2^+)\middle\|\rho\lambda\right)$	$-\left(\mu\nu\middle\|\Omega_1^+(\Omega_2^z)\middle\|\rho\lambda\right)$
	$\beta\beta$	$-\left(\mu\nu\middle\|\Omega_1^z(\Omega_2^z)\middle\|\rho\lambda\right)$	$-\left(\mu\nu\middle\|\Omega_1^z(\Omega_2^-)\middle\|\rho\lambda\right)$	$-\left(\mu\nu\middle\|\Omega_1^z(\Omega_2^+)\middle\|\rho\lambda\right)$	$+\left(\mu\nu\middle\|\Omega_1^z(\Omega_2^z)\middle\|\rho\lambda\right)$

6.2.2 Implementation

In this chapter, the GMP2 method combined with several levels of two-component Hamiltonians was implemented, according to the formulae described in the previous subsection. The most accurate two-component Hamiltonian adopted here is based on the IODKH transformation for the four-component DC Hamiltonian, termed IODKH/IODKH. Here, the strings before and after the slash mark (/) denote the levels of the relativistic corrections for the one- and two-electron parts of the Hamiltonian,

respectively. The definitions of the IODKH-transformed one-electron [41] and two-electron [8] parts of the Hamiltonian are given in Secs. 2.3 and 2.4, respectively. The present GMP2 code is also compatible with the IODKH/NR Hamiltonian, i.e., the combination of the IODKH one-electron terms and the untransformed NR electron-electron Coulomb operator.

In the present implementation, the four-index transformation is performed as four sequential one-index transformations in the same manner as the well-established NR four-index transformation [42],

$$\left(i\nu\left|g_{12}\right|\rho\lambda\right)=\sum_{\omega}^{\{\alpha,\beta\}}\sum_{\mu}^{\{\mathrm{AO}\}}\left(C_{\mu i}^{\omega}\right)^{*}\left(\mu\nu\left|g_{12}\right|\rho\lambda\right), \tag{6.20}$$

$$\left(ia\left|g_{12}\right|\rho\lambda\right)=\sum_{\omega'}^{\{\alpha,\beta\}}\sum_{\nu}^{\{\mathrm{AO}\}}C_{\nu a}^{\omega'}\left(i\nu\left|g_{12}\right|\rho\lambda\right), \tag{6.21}$$

$$\left(ia\left|g_{12}\right|j\lambda\right)=\sum_{\tau}^{\{\alpha,\beta\}}\sum_{\rho}^{\{\mathrm{AO}\}}\left(C_{\rho j}^{\tau}\right)^{*}\left(ia\left|g_{12}\right|\rho\lambda\right), \tag{6.22}$$

and

$$\left(ia\left|g_{12}\right|jb\right)=\sum_{\tau'}^{\{\alpha,\beta\}}\sum_{\lambda}^{\{\mathrm{AO}\}}C_{\lambda b}^{\tau'}\left(ia\left|g_{12}\right|j\lambda\right). \tag{6.23}$$

There are three modifications of the algorithm compared to the NR transformation. The first modification is the use of complex algebra instead of real algebra to describe the SD relativistic effects. The integral values and MO coefficients will be complex numbers in the general case of the SD relativistic calculations. The second modification is the expansion of the two-electron integrals. Namely, the NR two-electron Coulomb integrals are replaced by the g_{12}^{SF}, g_{12}^{SD1}, g_{12}^{SD2}, and g_{12}^{SD3} type two-electron integrals; the transformation for each type of integral follows the formulae in the previous subsection. The third modification is the permutational symmetry, which is accompanied by the

second modification. The g_{12}^{SF} type integrals have the same eight-fold symmetry as the NR two-electron Coulomb integrals,

$$\begin{aligned}\left(\mu\nu\left|g_{12}^{\mathrm{SF}}\right|\rho\lambda\right)&=\left(\nu\mu\left|g_{12}^{\mathrm{SF}}\right|\rho\lambda\right)=\left(\mu\nu\left|g_{12}^{\mathrm{SF}}\right|\lambda\rho\right)=\left(\nu\mu\left|g_{12}^{\mathrm{SF}}\right|\lambda\rho\right)\\&=\left(\rho\lambda\left|g_{12}^{\mathrm{SF}}\right|\mu\nu\right)=\left(\lambda\rho\left|g_{12}^{\mathrm{SF}}\right|\mu\nu\right)=\left(\rho\lambda\left|g_{12}^{\mathrm{SF}}\right|\nu\mu\right)=\left(\lambda\rho\left|g_{12}^{\mathrm{SF}}\right|\nu\mu\right).\end{aligned}\tag{6.24}$$

In contrast, for the spatial parts of the g_{12}^{SD1} and g_{12}^{SD2} type integrals, there exist four-fold-like symmetries,

$$\left(\mu\nu\left|\Omega_1^{\xi_1}\right|\rho\lambda\right)=-\left(\nu\mu\left|\Omega_1^{\xi_1}\right|\rho\lambda\right)=\left(\mu\nu\left|\Omega_1^{\xi_1}\right|\lambda\rho\right)=-\left(\nu\mu\left|\Omega_1^{\xi_1}\right|\lambda\rho\right)\tag{6.25}$$

and

$$\left(\mu\nu\left|\Omega_2^{\xi_2}\right|\rho\lambda\right)=\left(\nu\mu\left|\Omega_2^{\xi_2}\right|\rho\lambda\right)=-\left(\mu\nu\left|\Omega_2^{\xi_2}\right|\lambda\rho\right)=-\left(\nu\mu\left|\Omega_2^{\xi_2}\right|\lambda\rho\right).\tag{6.26}$$

For the spatial part of the g_{12}^{SD3} type integrals, there exists an eight-fold-like symmetry in the diagonal ($\xi_1=\xi_2$) tensor components,

$$\begin{aligned}&\left(\mu\nu\left|\Omega_1^{\xi_1}\left(\Omega_2^{\xi_2}\right)\right|\rho\lambda\right)=-\left(\nu\mu\left|\Omega_1^{\xi_1}\left(\Omega_2^{\xi_2}\right)\right|\rho\lambda\right)\\&=-\left(\mu\nu\left|\Omega_1^{\xi_1}\left(\Omega_2^{\xi_2}\right)\right|\lambda\rho\right)=\left(\nu\mu\left|\Omega_1^{\xi_1}\left(\Omega_2^{\xi_2}\right)\right|\lambda\rho\right)\\&=\left(\rho\lambda\left|\Omega_1^{\xi_1}\left(\Omega_2^{\xi_2}\right)\right|\mu\nu\right)=-\left(\lambda\rho\left|\Omega_1^{\xi_1}\left(\Omega_2^{\xi_2}\right)\right|\mu\nu\right)\\&=-\left(\rho\lambda\left|\Omega_1^{\xi_1}\left(\Omega_2^{\xi_2}\right)\right|\nu\mu\right)=\left(\lambda\rho\left|\Omega_1^{\xi_1}\left(\Omega_2^{\xi_2}\right)\right|\nu\mu\right),\end{aligned}\tag{6.27}$$

and a four-fold-like symmetry in the off-diagonal ($\xi_1\neq\xi_2$) tensor components,

$$\begin{aligned}&\left(\mu\nu\left|\Omega_1^{\xi_1}\left(\Omega_2^{\xi_2}\right)\right|\rho\lambda\right)=-\left(\nu\mu\left|\Omega_1^{\xi_1}\left(\Omega_2^{\xi_2}\right)\right|\rho\lambda\right)\\&=-\left(\mu\nu\left|\Omega_1^{\xi_1}\left(\Omega_2^{\xi_2}\right)\right|\lambda\rho\right)=\left(\nu\mu\left|\Omega_1^{\xi_1}\left(\Omega_2^{\xi_2}\right)\right|\lambda\rho\right).\end{aligned}\tag{6.28}$$

Note that the minus signs in Eqs. (6.25)–(6.28) stem from the anti-commutativity of the cross-product contained in the $\boldsymbol{\Omega}$ operators.

6.3 Numerical assessments

6.3.1 Computational details

This section assesses the performance of the present GMP2 method combined with five levels of Hamiltonians: the one-electron NR Hamiltonian with the two-electron NR Coulomb interaction (NR/NR), the one-electron IODKH Hamiltonian with the two-electron NR Coulomb interaction in the SF (SF-IODKH/NR) and SD (SD-IODKH/NR) formalisms, and the one-electron IODKH Hamiltonian with the two-electron IODKH-transformed Coulomb interaction in the SF (SF-IODKH/IODKH) and SD (SD-IODKH/IODKH) formalisms. For the reference calculations, the four-component DC Hamiltonian was adopted. For comparison, five widely-used two-component Hamiltonians were also used with the two-electron NR coulomb interaction in the SF formalism: the SF-ZORA/NR, SF-RESC/NR, and SF-DKH*n*/NR (n = 1, 2, and 3) Hamiltonians. The higher-order SD contributions in the IODKH transformation for the two-electron terms were neglected to reduce the computational cost, as explained in the previous study [8]. The point nucleus model was used in the evaluation of the electron-nucleus interaction. The NR/NR, SF-IODKH/NR, SD-IODKH/NR, SF-IODKH/IODKH, and SD-IODKH/IODKH calculations were performed using the in-house relativistic program. The DC and SF-ZORA/NR calculations were performed using DIRAC12 [43]. The SF-RESC/NR and SF-DKH*n*/NR calculations were performed using GAMESS [44].

Numerical assessments were performed for He-like atoms (with nuclear charges Z = 2, 10, 20, …, and 110), Ne-like atoms (Z = 10, 20, …, and 110), and 16 diatomic molecules including HX, X_2 (X = F, Cl, Br, I, and At), MH, and M_2 (M = Cu, Ag, and Au). For the atomic systems, the universal Gaussian-type basis sets optimized for the four-component DC calculations by Malli et al. [45] were employed, i.e., (40s40p) for the

He-like atoms and (40s40p25d) for the Ne-like atoms. For the molecular systems, the Sapporo-(DKH3-)DZP-2012 basis sets [46,47] were used in an uncontracted form. The experimental bond lengths [48,49] were used, except for HAt and At_2. The optimized bond lengths reported in previous theoretical studies [50,51] were used for HAt and At_2. In the molecular MP2 calculations, the outermost s/p- and s/p/d-electrons were correlated for the halogens and the coinage metal atoms, respectively.

6.3.2 Accuracy in He- and Ne-like atoms

In relativistic quantum chemistry, He-like atoms with large Z are widely used as test systems because the relativistic effects derived from the $1s^2$ configuration affects the electronic energy and properties significantly. In particular, the behavior of the electron correlation energy with respect to Z depends on the level of accuracy of the relativistic Hamiltonian [52-54]. For example, the absolute value of the correlation energy calculated using SF-DKH3/NR, which is one of the widely-used two-component relativistic Hamiltonians, is largely overestimated in comparison with the DC results [53]. This subsection discusses the Hamiltonian dependence of the MP2 correlation energies of the He-like atoms as well as the Ne-like atoms to examine the accuracy of the present GMP2 method. Here, the MP2 correlation energies are investigated in terms of the four relativistic effects: SF one-electron, SF two-electron, SD one-electron, and SD two-electron effects.

First, the SF one-electron effect is examined. Figure 6.1 shows the MP2 correlation energies of the He-like atoms with Z = 2–110 at the NR/NR, SF-ZORA/NR, SF-RESC/NR, SF-DKHn/NR (n = 1, 2, and 3), SF-IODKH/NR, and DC levels. The nuclear charge Z is shown on the horizontal axis. The vertical axis represents the MP2 correlation

energies in hartrees. The NR/NR correlation energies are almost constant with approximately −0.04 hartrees from Z = 10 to 110. At the four-component DC level, the correlation energies decrease monotonically with increasing Z. The larger absolute values of the correlation energies in DC compared to those in NR/NR are due to the enhancement of the electron repulsion induced by the relativistic orbital contraction.

All the SF one-electron Hamiltonians overestimate the absolute values of the correlation energies compared with the results of the DC calculations, although the energies also monotonically decrease. This can be explained by the excessive shrinkage of the 1s orbital due to the unbalanced treatment of the one- and two-electron parts of the two-component Hamiltonian, as pointed out by Tatewaki and Noro [53]. SF-IODKH/NR, whose one-electron part is equivalent to the four-component Dirac Hamiltonian, gives the limit of the correlation energy when the SF one-electron relativistic effect alone is considered. In SF-ZORA/NR, the absolute values of the correlation energies are significantly overestimated compared with those of SF-IODKH/NR. In SF-RESC/NR, the absolute values of the correlation energies are smaller than those in SF-IODKH/NR, although the values are closer to SF-IODKH/NR compared with SF-ZORA/NR. SF-DKH1/NR also overestimates the absolute values of the SF-IODKH/NR results. In contrast, the behaviors of SF-DKH2/NR and SF-DKH3/NR are similar to that of SF-IODKH/NR. These improvements are due to the inclusion of the higher-order relativistic terms. Consequently, more accurate relativistic treatments than the DKH2 level are required to correctly describe the SF one-electron relativistic effect in the correlation energies; however, the SF one-electron relativistic effect alone is insufficient to describe the correlation energies at the DC level.

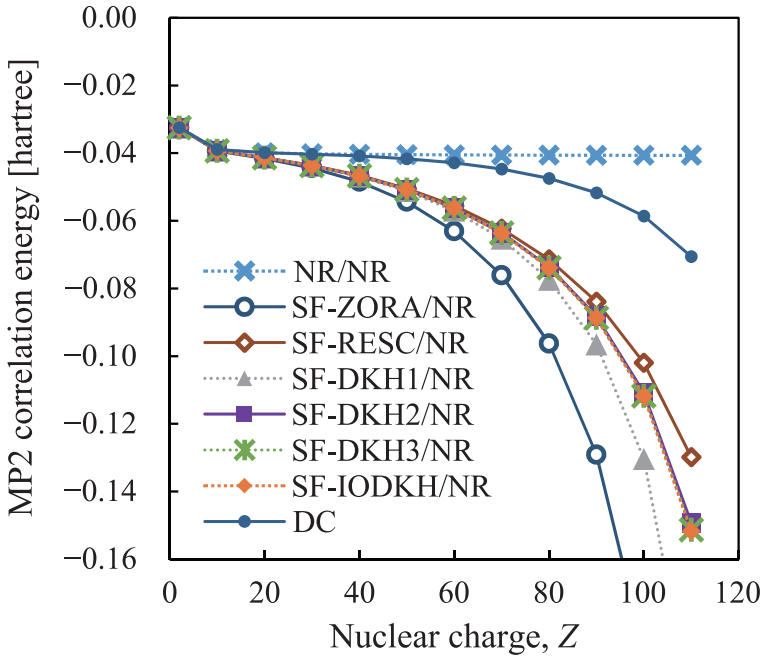

Figure 6.1. MP2 correlation energies for He-like atoms with Z = 2–110 using the NR/NR, SF-ZORA/NR, SF-RESC/NR, SF-DKH*n*/NR (n = 1, 2, and 3), SF-IODKH/NR, and DC Hamiltonians.

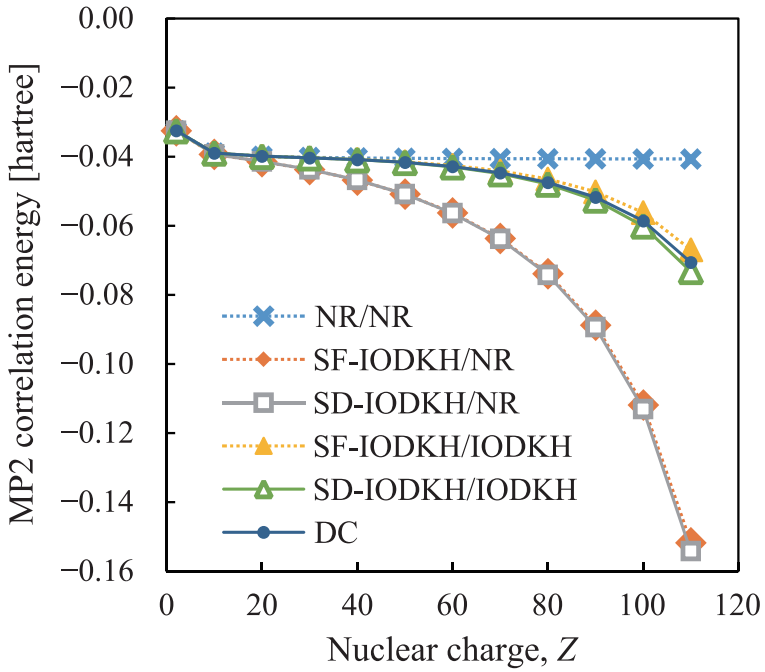

Figure 6.2. MP2 correlation energies for He-like atoms with Z = 2–110 using the NR/NR, SF-IODKH/NR, SD-IODKH/NR, SF-IODKH/IODKH, SD-IODKH/IODKH, and DC Hamiltonians.

Next, the other relativistic effects are examined. Figure 6.2 shows the MP2 correlation energies of the He-like atoms at the NR/NR, SF-IODKH/NR, SD-IODKH/NR, SF-IODKH/IODKH, SD-IODKH/IODKH, and DC levels. Let us focus on the SF two-electron relativistic effect. SF-IODKH/IODKH reproduces the DC correlation energies well, which indicates that both SF one- and two-electron relativistic effects contribute to the correlation energies significantly. The smaller absolute values of the correlation energies in SF-IODKH/IODKH compared with those in SF-IODKH/NR are because the electron-electron Darwin interaction, which is included in the IODKH-transformed two-electron terms, induces the inter-electron attraction.

Now, let us discuss the SD one- and two-electron effects. SD-IODKH/NR overestimates the absolute values of the DC correlation energies, and its behavior is similar to that of SF-IODKH/NR. This indicates that the SD one-electron relativistic effect slightly affects the correlation energies because of the $1s^2$ configuration. SD-IODKH/IODKH reproduces the DC results as well as SF-IODKH/IODKH. The absolute values of the correlation energies in SD-IODKH/IODKH are slightly larger than those in SF-IODKH/IODKH. Additionally, the difference between SF- and SD-IODKH/NR is larger than that between SF- and SD-IODKH/IODKH. This indicates that the SD two-electron effect is larger than the SD one-electron effect in the correlation energies. Consequently, the SF one- and two-electron relativistic effects are essential to reproduce the correlation energies at the DC level for the He-like atoms.

Finally, the relativistic effects in the correlation energies for the Ne-like atoms are examined. Figure 6.3 shows the MP2 correlation energies for the Ne-like atoms with Z = 10–110 using the NR/NR, SF-IODKH/NR, SD-IODKH/NR, SF-IODKH/IODKH, SD-IODKH/IODKH, and DC Hamiltonians. The trends in the correlation energies with

respect to Z are similar to those of the He-like atoms. In NR/NR, almost constant correlation energies are obtained. In DC, the correlation energies decrease with increasing Z. SF-IODKH/NR overestimates the absolute values of the DC results. In SD-IODKH/NR, the absolute values of the correlation energies are slightly larger than those in SF-IODKH/NR.

In contrast, the behavior of the correlation energies in SF-IODKH/IODKH is different from that for the He-like atoms. Namely, SF-IODKH/IODKH underestimates the absolute values of the DC correlation energies, although the behavior is similar to that of DC. In SD-IODKH/IODKH, the behavior of the correlation energies is improved, although the absolute values are slightly overestimated compared with those of DC. Namely, the inclusion of the SD one- and two-electron terms contributes to an increase in the absolute values of the correlation energies in comparison with SF-IODKH/IODKH. The significance of the SD relativistic effects for the Ne-like atoms is due to the $1s^2 2s^2 2p^6$ configuration: the 2p shell, which is the innermost shell affected by SO interactions, is occupied in the ground state. Consequently, the four relativistic terms, i.e., the SF one-electron, SD one-electron, SF two-electron, and SD two-electron terms are essential for the correlation energies of the Ne-like atoms.

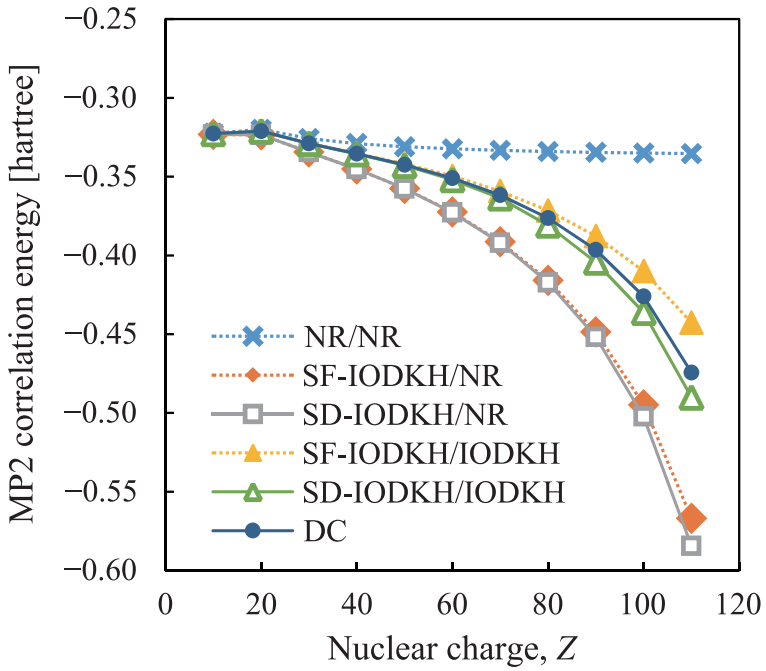

Figure 6.3. MP2 correlation energies for Ne-like atoms with Z = 10–110 using the NR/NR, SF-IODKH/NR, SD-IODKH/NR, SF-IODKH/IODKH, SD-IODKH/IODKH, and DC Hamiltonians.

6.3.3 Accuracy in diatomic molecules

This subsection investigates the accuracy of the present GMP2 method for 16 typical diatomic molecules including the first- to sixth-row elements. Table 6.2 shows the MP2 correlation energies using the NR/NR, SF-IODKH/NR, SD-IODKH/NR, SF-IODKH/IODKH, SD-IODKH/IODKH, and DC Hamiltonians. The original values of the correlation energies are shown for DC, and the deviations from the DC values are shown for the other Hamiltonians. In NR/NR, the MaxAD of the correlation energies is 0.091913 hartrees for Au_2. In SF-IODKH/NR, the correlation energies are improved by one order of magnitude through the inclusion of the SF one-electron relativistic effect, where the MaxAD is 0.003072 hartrees for Au_2. In SD-IODKH/NR, the correlation energies are improved by one more orders of magnitude due to the SD one-electron effect, where the MaxAD is 0.000318 hartrees for Au_2. In SF-IODKH/IODKH, the MaxAD in the

correlation energies is 0.002732 hartrees for Au_2, which is the smaller value compared with SF-IODKH/NR due to the SF two-electron relativistic effect. In SD-IODKH/IODKH, further improvement of the MP2 correlation energies is achieved through the inclusion of the SD two-electron relativistic effect, where the MaxAD is 0.000032 hartrees for Au_2. Consequently, SD-IODKH/IODKH reproduces the DC correlation energies for the typical heavy-element systems with sub-microhartree accuracy.

6.3.4 Computational cost

This subsection discusses the computational cost of the present GMP2 method for 16 diatomic molecules. Table 6.3 shows the CPU times taken for the MP2 calculations at the SD-IODKH/NR, SD-IODKH/IODKH, and DC levels. The speed-up ratios in comparison with the DC results are also shown. A single core of an Intel Xeon E5-2690 (2.90 GHz) processor was used.

In SD-IODKH/NR, the MP2 calculations are 29.6 to 141.5 times faster than those in DC. This is due to two factors. The first factor is the size of the AO space. The number of dimensions of the AO space in DC is approximately 1.6 to 1.7 times more than that in SD-IODKH/NR. The increased AO dimension arises from the small component basis functions generated by the restricted kinetic balance condition, which is a condition to avoid variational collapse in the four-component calculations. The second factor is the number of types of two-electron integrals. In SD-IODKH/NR, one type of two-electron integrals is treated, whereas DC requires 16 types of two-electron integrals involving the large (L) and small (S) component basis functions, i.e., one type of (LL|LL), three types of (LL|SS), three types of (SS|LL), and nine types of (SS|SS) integrals. The (LL|LL)-type

integrals correspond to the NR two-electron integrals appearing in the SD-IODKH/NR calculations.

In SD-IODKH/IODKH, the MP2 calculations are 2.2 to 8.4 times faster than those in DC. The longer CPU time in DC is due to the larger size of the AO space, as explained above. Compared with SD-IODKH/NR, SD-IODKH/IODKH requires approximately 13.5 to 16.8 times greater CPU time. This is because, as DC, SD-IODKH/IODKH also treats 16 types of two-electron integrals. This extra computational cost in SD-IODKH/IODKH would be efficiently reduced by parallelization because the four-index transformation for each type of integral is completely independent.

6.4 Conclusion

In this chapter, the author has proposed a general formulation for the GMP2 method in accordance with the analytical two-component relativistic Hamiltonians for many-electron systems, allowing the description of the full relativistic effects at the DC level. Based on this general formulation, the GMP2 code for the IODKH/IODKH Hamiltonian have been implemented.

For the numerical assessments, the correlation energies for He-like and Ne-like atoms were evaluated. For the He-like atoms, the trend in the MP2 correlation energies of DC with respect to the nuclear charge was reproduced well by the SF- and SD-IODKH/IODKH Hamiltonians, indicating the significance of the SF one- and two-electron relativistic effects. For the Ne-like atoms, on the other hand, the DC results were reproduced well only by the SD-IODKH/IODKH Hamiltonian, indicating the significance of the full relativistic effects, i.e., the SF and SD one-/two-electron effects.

The accuracy and computational cost of the present GMP2 method were also

assessed for 16 typical diatomic molecules including first- to sixth-row elements. In these systems, the MP2 correlation energies using the DC Hamiltonian were reproduced by the SD-IODKH/IODKH Hamiltonian with sub-microhartree accuracy. The CPU times of the present GMP2 calculations for the SD-IODKH/IODKH Hamiltonian were 2.2 to 8.4 times smaller than that for the DC Hamiltonian.

The present method, where the GHF wavefunction is used as a reference state, can be extended to higher-order electron correlation theories including configuration interaction and coupled cluster methods in the same manner.

Table 6.2. MP2 correlation energies (in hartrees) for 16 diatomic molecules. The original values are shown in the DC column; the deviations from the DC values are shown in the other columns.

Molecule	Deviation from DC					DC
	NR/NR	SF-IODKH/NR	SD-IODKH/NR	SF-IODKH/IODKH	SD-IODKH/IODKH	
HF	0.000232	−0.000036	−0.000036	0.000000	0.000000	−0.250145
HCl	0.000220	−0.000009	−0.000008	−0.000001	0.000000	−0.177509
HBr	0.000383	−0.000028	0.000000	−0.000025	0.000000	−0.147837
HI	0.000074	−0.000125	0.000001	−0.000123	−0.000001	−0.124264
HAt	−0.001004	−0.001412	0.000029	−0.001418	−0.000010	−0.117239
CuH	0.008674	−0.000102	−0.000069	−0.000019	−0.000007	−0.828655
AgH	0.016011	0.000098	0.000047	0.000069	−0.000011	−0.590833
AuH	0.049990	0.001358	0.000214	0.001126	−0.000016	−0.543153
F_2	0.000458	−0.000069	−0.000068	−0.000001	0.000000	−0.485178
Cl_2	0.000472	−0.000014	−0.000012	−0.000002	0.000000	−0.326546
Br_2	0.000912	−0.000048	0.000004	−0.000048	−0.000001	−0.267605
I_2	0.000473	−0.000243	0.000005	−0.000246	−0.000002	−0.218481
At_2	−0.010399	0.001614	0.000081	0.001609	−0.000025	−0.205443
Cu_2	0.016714	−0.000214	−0.000130	−0.000044	−0.000012	−1.619134
Ag_2	0.031357	0.000208	0.000087	0.000163	−0.000019	−1.159289
Au_2	0.091913	0.003072	0.000318	0.002732	−0.000032	−1.049347

Table 6.3. CPU time (in seconds) of MP2 calculations for 16 diatomic molecules. A single core of an Intel Xeon E5-2690 (2.90 GHz) processor was used. The values in parentheses show speed-up ratios of the SD-IODKH/NR and SD-IODKH/IODKH calculations to the DC calculations. The number of AOs for one component (or large component) is also shown as n_{AO}.

Molecule	n_{AO}	CPU time				
		SD-IODKH/NR		SD-IODKH/IODKH		DC
HF	45	0.1	(35.0)	1.3	(2.7)	3.4
HCl	74	0.5	(52.2)	7.7	(3.7)	28.3
HBr	131	4.0	(86.5)	60.9	(5.6)	342.0
HI	148	5.8	(89.7)	88.7	(5.8)	515.8
HAt	231	30.6	(131.9)	485.8	(8.3)	4035.0
CuH	125	8.2	(37.7)	116.7	(2.6)	308.4
AgH	145	12.9	(42.7)	183.3	(3.0)	552.7
AuH	219	54.7	(61.0)	904.6	(3.7)	3338.4
F_2	64	0.6	(29.6)	8.0	(2.2)	17.7
Cl_2	122	5.4	(54.5)	74.4	(3.9)	292.3
Br_2	236	55.0	(95.5)	801.0	(6.6)	5249.0
I_2	270	83.6	(110.5)	1231.4	(7.5)	9237.8
At_2	436	584.1	(141.5)	9848.3	(8.4)	82677.3
Cu_2	224	128.8	(38.3)	1808.9	(2.7)	4932.2
Ag_2	264	210.0	(45.0)	3021.8	(3.1)	9440.0
Au_2	412	1087.4	(62.9)	17736.7	(3.9)	68378.4

References

[1] W. Liu, *Mol. Phys.* **108**, 1679 (2010).

[2] T. Saue, *ChemPhysChem* **12**, 3077 (2011).

[3] J. Sucher, *Phys. Rev. A* **22**, 348 (1980).

[4] B. A. Hess, *Phys. Rev. A* **32**, 756 (1985).

[5] R. Samzow, B. A. Hess, G. Jansen, *J. Chem. Phys.* **96**, 1227 (1992).

[6] C. van Wüllen, C. Michauk, *J. Chem. Phys.* **123**, 204113 (2005).

[7] C. Park, J. E. Almlöf, *Chem. Phys. Lett.* **231**, 269 (1994).

[8] J. Seino, M. Hada, *Chem. Phys. Lett.* **461**, 327 (2008).

[9] J. Seino, H. Nakai, *J. Chem. Phys.* **136**, 244102 (2012).

[10] D. Peng, M. Reiher, *J. Chem. Phys.* **136**, 244108 (2012).

[11] J. Seino, H. Nakai, *J. Chem. Phys.* **137**, 144101 (2012).

[12] J. Sikkema, L. Visscher, T. Saue, M. Iliaš, *J. Chem. Phys.* **131**, 124116 (2009).

[13] D. Peng, W. Liu, Y. Xiao, L. Cheng, *J. Chem. Phys.* **127**, 104106 (2007).

[14] W. Liu, D. Peng, *J. Chem. Phys.* **125**, 44102 (2006).

[15] K. G. Dyall, *J. Chem. Phys.* **115**, 9136 (2001).

[16] K. G. Dyall, *J. Comput. Chem.* **23**, 786 (2002).

[17] K. G. Dyall, K. Faegri, Introduction to Relativistic Quantum Chemistry, Oxford University Press, New York, 2007.

[18] P. Schwerdtfeger, Relativistic Electronic Structure Theory, Part 2. Applications, Elsevier Science, Amsterdam, 2004.

[19] B. Schimmelpfennig, AMFI: An Atomic Mean-Field Integral Program, University of Stockholm, Stockholm, Sweden, 1996.

[20] J. C. Boettger, *Phys. Rev. B* **62**, 7809 (2000).

[21] J. Chalupský, T. Yanai, *J. Chem. Phys.* **139**, 204106 (2013).

[22] R. Seeger, J. A. Pople, *J. Chem. Phys.* **66**, 3045 (1977).

[23] H. Fukutome, *Int. J. Quantum Chem.* **20**, 955 (1981).

[24] J.-L. Calais, *Adv. Quantum Chem.* **17**, 225 (1985).

[25] R. McWeeny, Methods of Molecular Quantum Mechanics, Academic Press, London, 1989.

[26] P.-O. Löwdin, I. Mayer, *Adv. Quantum Chem.* **24**, 79 (1992).

[27] S. Hammes-Schiffer, H. C. Andersen, *J. Chem. Phys.* **99**, 1901 (1993).

[28] S. K. Wolff, D. Jayatilaka, G. S. Chandler, *J. Chem. Phys.* **103**, 4562 (1995).

[29] D. Jayatilaka, *J. Chem. Phys.* **108**, 7587 (1998).

[30] J. L. Stuber, J. Paldus, in: E. J. Brändas, E. S. Kryachko (Eds.), Fundamental World of Quantum Chemistry, Kluwer Academic Publishers, Dordrecht, 2003, p. 67.

[31] M. K. Armbruster, F. Weigend, C. van Wüllen, W. Klopper, *Phys. Chem. Chem. Phys.* **10**, 1748 (2008).

[32] D. Yamaki, Y. Shigeta, S. Yamanaka, H. Nagao, K. Yamaguchi, *Int. J. Quantum Chem.* **80**, 701 (2000).

[33] R. Fukuda, H. Nakatsuji, *J. Chem. Phys.* **123**, 044101 (2005).

[34] T. Yoshizawa, M. Hada, *J. Comput. Chem.* **30**, 2550 (2009).

[35] Y. S. Kim, S. Y. Lee, W. S. Oh, B. H. Park, Y. K. Han, S. J. Park, Y. S. Lee, *Int. J. Quantum Chem.* **66**, 91 (1998).

[36] S. Hirata, T. Yanai, R. J. Harrison, M. Kamiya, P. D. Fan, *J. Chem. Phys.* **126**, 024104 (2007).

[37] E. Eliav, U. Kaldor, B. A. Hess, *J. Chem. Phys.* **108**, 3409 (1998).

[38] F. Wang, J. Gauss, C. van Wüllen, *J. Chem. Phys.* **129**, 064113 (2008).

[39] F. Wang, J. Gauss, *J. Chem. Phys.* **129**, 174110 (2008).

[40] E. Epifanovsky, K. Klein, S. Stopkowicz, J. Gauss, A. I. Krylov, *J. Chem. Phys.* **143**, 064102 (2015).

[41] M. Barysz, A. J. Sadlej, *J. Chem. Phys.* **116**, 2696 (2002).

[42] S. Wilson, in: S. Wilson (Ed.), Methods in Computational Chemistry Vol. 1, Springer Science+Business Media, New York, 1987, p. 251.

[43] DIRAC, a relativistic ab initio electronic structure program, Release DIRAC12 (2012), written by H. J. Aa. Jensen, R. Bast, T. Saue, and L. Visscher, with contributions from V. Bakken, K. G. Dyall, S. Dubillard, U. Ekström, E. Eliav, T. Enevoldsen, T. Fleig, O. Fossgaard, A. S. P. Gomes, T. Helgaker, J. K. Lærdahl, Y. S. Lee, J. Henriksson, M. Iliaš, Ch. R. Jacob, S. Knecht, S. Komorovský, O. Kullie, C. V. Larsen, H. S. Nataraj, P. Norman, G. Olejniczak, J. Olsen, Y. C. Park, J. K. Pedersen, M. Pernpointner, K. Ruud, P. Sałek, B. Schimmelpfennig, J. Sikkema, A. J. Thorvaldsen, J. Thyssen, J. van Stralen, S. Villaume, O. Visser, T. Winther, and S. Yamamoto (see http://www.diracprogram.org).

[44] M. W. Schmidt, K. K. Baldridge, J. A. Boatz, S. T. Elbert, M. S. Gordon, J. H. Jensen, S. Koseki, N. Matsunaga, K. A. Nguyen, S. J. Su, T. L. Windus, M. Dupuis, J. A. Montgomery, *J. Comput. Chem.* **14**, 1347 (1993).

[45] G. L. Malli, A. B. F. Da Silva, Y. Ishikawa, *J. Chem. Phys.* **101**, 6829 (1994).

[46] T. Noro, M. Sekiya, T. Koga, *Theor. Chem. Acc.* **131**, 1124 (2012).

[47] T. Noro, M. Sekiya, T. Koga, *Theor. Chem. Acc.* **132**, 1363 (2013).

[48] K. P. Huber, G. Herzberg, Molecular Spectra and Molecular Structure, IV. Constants of Diatomic Molecules, Van Nostrand Reinhold, New York, 1950.

[49] J. Y. Seto, Z. Morbi, F. Charron, S. K. Lee, P. F. Bernath, R. J. Le Roy, *J. Chem. Phys.*

110, 11756 (1999).

[50] Y.-K. Han, C. Bae, S.-K. Son, Y. S. Lee, *J. Chem. Phys.* **112**, 2684 (2000).

[51] L. Visscher, K. G. Dyall, *J. Chem. Phys.* **104**, 9040 (1996).

[52] G. Pestka, H. Tatewaki, J. Karwowski, *Phys. Rev. A* **70**, 024501 (2004).

[53] H. Tatewaki, T. Noro, *Chem. Phys. Lett.* **399**, 480 (2004).

[54] Y. Watanabe, H. Tatewaki, *J. Chem. Phys.* **123**, 074322 (2005).

Chapter 7

Examination of frustrated spin systems based on the two-component approach: A case study for hydrogen ring clusters

7.1 Introduction

In quantum chemical calculations, open-shell or strongly correlated systems that have multi-radical characters are commonly treated using UHF-based methods. This approach assumes the collinearity of spin, i.e., one-dimensional spin alignment. However, multi-radical systems are highly diverse. For example, there exist many non-collinear spin systems, i.e., molecules with two- or three-dimensional spin orientations. The geometrically frustrated spin systems are the typical examples, possessing spin non-collinearity. The correct spin behaviors of the non-collinear or frustrated spin systems cannot be described by means of one-component UHF-based methods because the spin-quantized axis is fixed along one particular direction (normally the *z*-direction) in these methods.

A straightforward approach to investigate the non-collinear systems is to use two-component GHF-based methods [1-9]. In GHF, each of the spin-quantized axes can rotate freely because the spin-orbitals of GHF, termed the GSOs, are composed of a superposition of alpha and beta spin components. Although GHF and its related methods [2,8] have long been studied, they have rarely been adopted in practical applications. The main reason for this is that the GHF wavefunction is generally complex-valued and possesses high spin degrees of freedom, leading to local minima and SCF convergence

problems. Recently, several remedies to these problems have been proposed based on the second-order SCF [10] and DIIS [11] methods. A simple analysis to test the non-collinearity of the obtained solution has also been proposed. In addition, GHF has been extended to electron correlation methods within the NR [12,13] and relativistic [14] frameworks, the real-time propagation method of the time-dependent HF equation [15], and the spin projection method [16]. Thus far, there have been a few examples of application studies performed for the non-collinear or frustrated spin systems by means of GHF or the generalized Kohn–Sham method [17,18], i.e., the GHF's DFT cousin; for example, for fullerenes [19], hydrogen clusters [10,12,20], manganese clusters [21], and iron–sulfur clusters [22]. However, there is still a lot of room to elucidate the fundamental properties of frustrated spin systems. Furthermore, to the best of the knowledge, there is only one example of a post-GHF level study for these systems: for an asymmetric stretching of H_3 [12].

This chapter investigates the core properties of the equilateral triangular H_3 molecule, which is one of the simplest frustrated spin systems, and its extended systems (the H_7 and H_{11} molecules) by means of UHF and UMP2, i.e., one-component (collinear) methods; and by means of GHF and GMP2, i.e., two-component (non-collinear) methods. In particular, the author has focused on the potential energy curves and spin expectation values. This is because the major difference between UHF and GHF is the preserved spin symmetry; that is, UHF preserves the S_z but not S^2 symmetry, while GHF does not [2,8]. In addition, the difference of the spin symmetry leads to a difference in the total energies, which is known as Löwdin's dilemma [23].

This chapter is organized as follows. In Sec. 7.2, the computational details for the present examination is described. Section 7.3 discusses the behaviors of the potential

energy curves and spin expectation values for H_3, H_7, and H_{11}. Finally, Sec. 7.4 gives concluding remarks.

7.2 Computational details

All the calculations were performed at the UHF, UMP2, GHF and GMP2 levels using the Gaussian 09 program [24] and the in-house two-component code. The basis set adopted here was cc-pVDZ [25], which is the minimum required set to describe the polarization of the hydrogen s-orbitals. The geometries of the H_3, H_7, and H_{11} molecules were fixed as an equilateral triangle, heptagon, and hendecagon, respectively. In the UHF and UMP2 calculations, the LS and HS states were assumed for each of the molecules; that is, the doublet and quartet states for H_3, the doublet and octet states for H_7, and the doublet and dodecet states for H_{11}.

7.3 Results and discussion

Figure 7.1 shows the potential energy curves of the H_3 molecule at the UHF, GHF, UMP2, and GMP2 levels of theory. The bond length is indicated on the horizontal axis in ångström units. The vertical axis indicates the total energy in hartrees. Here, the UHF (UMP2) calculations for the LS and HS states are simply denoted as UHF(LS) and UHF(HS) [UMP2(LS) and UMP2(HS)], respectively. In UHF(LS), a potential energy curve that has a minimum value around 1.0 Å is obtained, while a repulsive curve is obtained in UHF(HS). The repulsive character of the UHF(HS) curve is due to Pauli repulsion between all the spin sites. Both of the curves converge to the same total energy value, i.e., approximately −1.5 hartrees, which is three times as large as the exact energy value of the single hydrogen atom (−0.5 hartrees). In GHF, the potential energy curve has

a minimum around 1.0 Å and converges to approximately −1.5 hartrees. However, the total energy values of the GHF solution are smaller than those of UHF(LS) at equilibrium through intermediate regions, indicating that GHF gives a broken-symmetry solution by removing the spin symmetry constraints. In addition, the UHF(LS) curve possesses the local maximum around 1.5 Å, while GHF does not. This behavior in UHF(LS) is because of the spin contamination by the HS (quartet spin) state. In GHF, the absence of a local maximum implies less spin contamination. In UMP2(LS), a bound potential curve is obtained, and the depth of the potential well is greater than that in UHF(LS) because of the inclusion of electron correlation. UMP2(HS) gives a qualitatively similar, repulsive curve to that of UHF(HS). The behavior of the GMP2 curve is similar to that of UMP2(LS). The total energy values of GMP2 are smaller than those of UMP2(LS), which indicates that GMP2 inherits the broken-symmetry character of GHF. All of the MP2 curves correctly converge to the same dissociation limit as those seen in the HF cases.

Incidentally, in Ref. [20], it is pointed out that GHF alone, i.e., without the spin-projection or multi-configurational techniques, cannot describe the equilibrium state of H_3, which is inconsistent with the aforementioned result. Possibly, unstable GHF solutions were obtained in the previous study, while variationally more stable GHF solutions are obtained here.

Figure 7.2 shows $\langle S_z \rangle$ (in the top panel) and $\langle S^2 \rangle$ (in the bottom panel), i.e., the spin expectation values of the S^2 and S_z operators, respectively, for the H_3 molecule at the UHF and GHF levels. The bond length is shown on the horizontal axis in ångström units. The vertical axis indicates the expectation values in atomic units. The HS and LS results are shown for UHF. In UHF(LS) and UHF(HS), the $\langle S_z \rangle$ values are constant for the entire region; the values are exactly $1/2 = 0.5$ and $3/2 = 1.5$, respectively. These

values reflect the doublet and quartet spin states, and also reflect that UHF preserves the S_z symmetry. In GHF, the $\langle S_z \rangle$ values are exactly zero and constant for the entire region, indicating that the non-collinear solutions are correctly obtained. The zero $\langle S_z \rangle$ values are due to the global cancellation of the individual atomic spin magnetization vectors on account of spin frustration. Importantly, $\langle S_x \rangle$ and $\langle S_y \rangle$ are also exactly zero for the entire region in GHF as well as UHF(LS) and UHF(HS), although they are not shown in the figure.

As shown in the bottom panel, $\langle S^2 \rangle$ of UHF(HS) is exactly 3.75. This value is obtained by substituting $S = 3/2$ for $S(S+1)$, which coincides with the exact eigenvalue of the S^2 operator. Thus, the UHF(HS) solution here gives the non-spin-contaminated solutions, which correspond to the exact quartet eigenstate. In UHF(LS), the $\langle S^2 \rangle$ value is close to 0.75, i.e., the exact eigenvalue of the S^2 operator for the doublet states, in the equilibrium region. $\langle S^2 \rangle$ monotonically increases with respect to the bond length, and converges to 1.75 in the dissociation region. This behavior indicates that the magnitude of the spin contamination becomes larger with increasing bond length, as seen in many molecules [26]. A similar behavior concerning $\langle S^2 \rangle$ is obtained in GHF. Namely, the $\langle S^2 \rangle$ value is approximately 0.75 in the equilibrium region, and monotonically increases with respect to the bond length. In the dissociation region, however, the value converges to 1.50, which is smaller than the corresponding UHF(LS) value. Thus, the GHF solution gives a less spin-contaminated solution than UHF for the dissociation process, as previously mentioned.

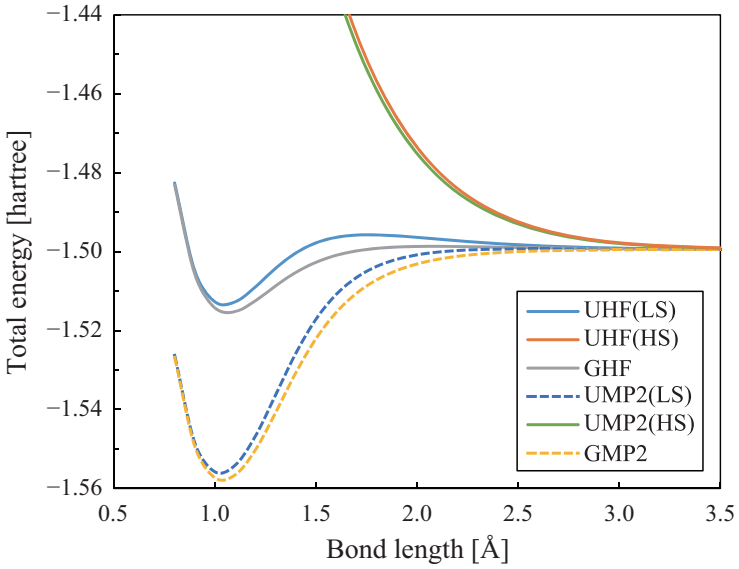

Figure 7.1. Potential energy curves of H_3 at the UHF, GHF, UMP2, and GMP2 levels. The LS and HS solutions of UHF and UMP2 correspond to the doublet and quartet states, respectively.

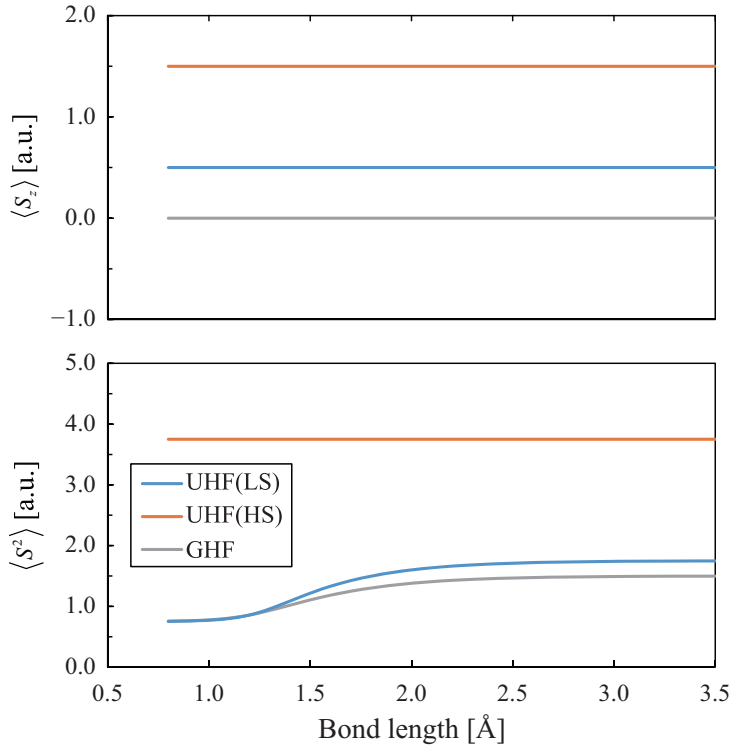

Figure 7.2. Expectation values of S_z (top) and S^2 (bottom) for H_3 at the UHF and GHF. The LS and HS values are shown for UHF.

Next, the results of the extended systems, i.e., the H_7 and H_{11} molecules, are discussed. Figures 7.3 and 7.4 show the potential energy curves of H_7 and H_{11}, respectively. The general trends of these curves are similar to that of the H_3 curves. Namely, in UHF(LS), GHF, UMP2(LS), and GMP2, the curves have minima around 1.0 Å. GHF and GMP2 give lower total energies than UHF(LS) and UMP2(LS), respectively. The potential well depths of UMP2(LS) and GMP2 are larger than those of UHF(LS) and GHF, respectively. The behaviors of the UHF(HS) and UMP2(HS) curves are similar, both of which show the repulsive character. Additionally, these curves approximately converge to the value of multiplying –0.5 hartrees (the exact energy value of the hydrogen atom) by the number of the hydrogen atoms included in each system. The difference between the H_7 and H_{11} curves from the H_3 curve is the absence of the local maximum around the intermediate region in UHF(LS), which does not indicate the lesser degree of spin contamination in H_7 and H_{11} than in H_3, as described later. This is because the contaminating contribution of the HS state in the UHF(LS) solution is relatively reduced by the increase in that of the other intermediate spin states.

Figures 7.5 and 7.6 show the spin expectation values of H_7 and H_{11}, respectively, at the UHF and GHF levels. For the both molecules, constant $\langle S_z \rangle$ values are obtained in the entire region, as seen in the H_3 case. UHF(LS) gives $\langle S_z \rangle = 1/2 = 0.5$, indicating its doublet character. UHF(HS) gives $\langle S_z \rangle = 7/2 = 3.5$ for H_7 and $\langle S_z \rangle = 11/2 = 5.5$ for H_{11}, representing the octet and dodecet characters, respectively. In GHF, the $\langle S_z \rangle$ values are entirely zero, as well as $\langle S_x \rangle$ and $\langle S_y \rangle$, because of the cancellation of the atomic magnetization vectors. Consequently, it is confirmed that the non-collinear solutions are correctly obtained for H_7 and H_{11}.

The $\langle S^2 \rangle$ values of UHF(HS) are exactly 15.75 for H_7 and 35.75 for H_{11}. These

values are obtained by substituting $S = 7/2$ and $11/2$ for $S(S+1)$, respectively, and correspond to the exact eigenvalues of the S^2 operator. In UHF(LS) and GHF, the $\langle S^2 \rangle$ values in the equilibrium region are approximately 0.75, which is close to the exact S^2 eigenvalue for the doublet state. The values increase as the bond length gets longer. Here, Table 7.1 lists the $\langle S^2 \rangle$ values at 3.5 Å in UHF(LS) and GHF. For H_7 and H_{11}, the $\langle S^2 \rangle$ values of GHF at 3.5 Å are smaller than those of UHF(LS), indicating the lesser degree of spin contamination in GHF than in UHF(LS) at the dissociation region, as seen in the H_3 case. Furthermore, in both of UHF(LS) and GHF, $\langle S^2 \rangle$ around the dissociation region becomes larger with increasing ring size, n. Thus, the spin contamination becomes more significant with increasing n. This is because of the large number of degrees of freedom with respect to the orientation of the spin magnetization vectors on each of the spin sites at large ring sizes.

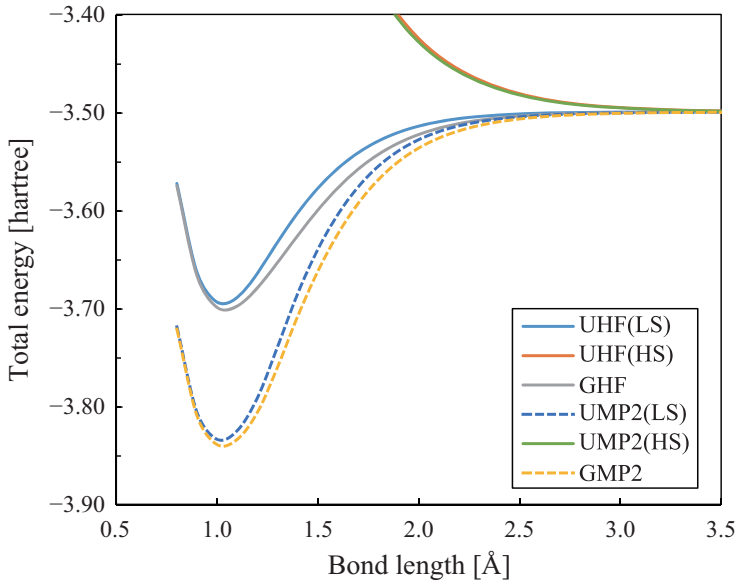

Figure 7.3. Potential energy curves of H_7 at the UHF, GHF, UMP2, and GMP2 levels. The LS and HS solutions of UHF and UMP2 correspond to the doublet and octet states, respectively.

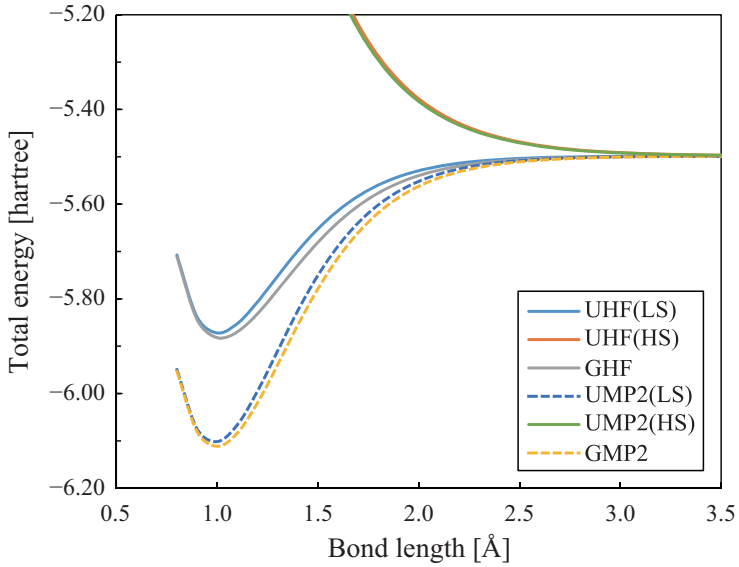

Figure 7.4. Potential energy curves of H_{11} at the UHF, GHF, UMP2, and GMP2 levels. The LS and HS solutions of UHF and UMP2 correspond to the doublet and dodecet states, respectively.

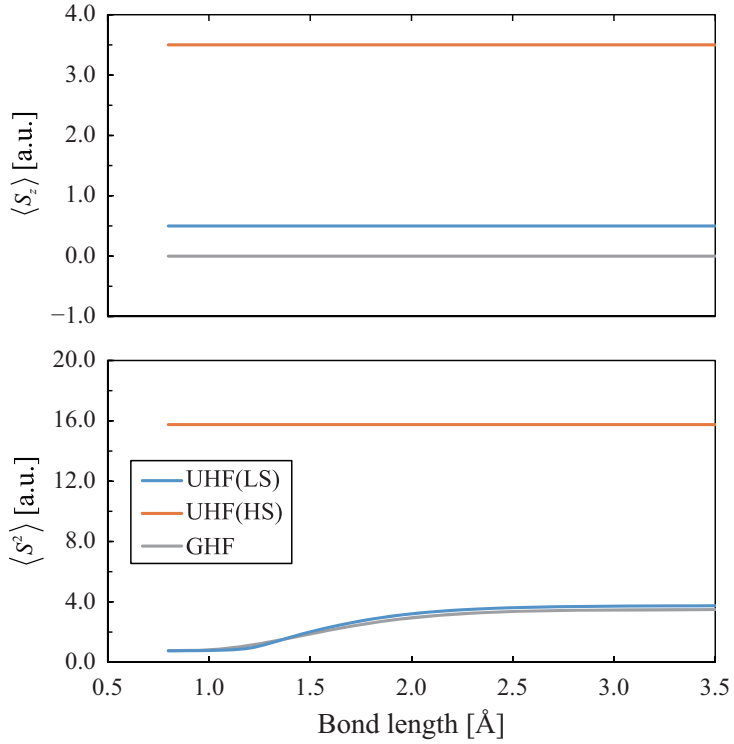

Figure 7.5. Expectation values of S_z (top) and S^2 (bottom) for H_7 at the UHF and GHF. The LS and HS values are shown for UHF.

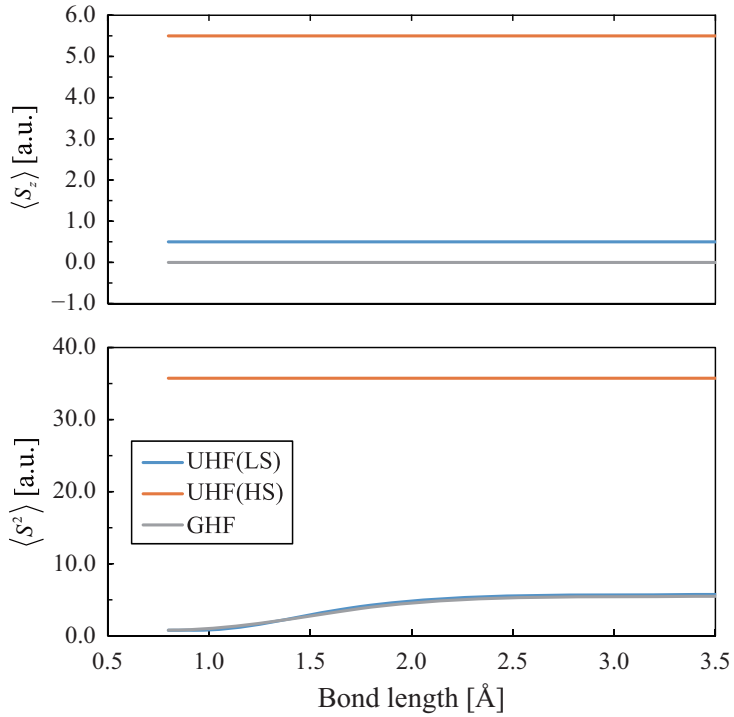

Figure 7.6. Expectation values of S_z (top) and S^2 (bottom) for H_{11} at the UHF and GHF. The LS and HS values are shown for UHF.

Table 7.1. Expectation values of S^2 for the equilateral H_n molecules, where the bond lengths are 3.5 Å, at the UHF and GHF levels. The LS states are assumed in UHF.

n	UHF(LS)	GHF
3	1.75	1.50
7	3.74	3.49
11	5.74	5.49

7.4 Conclusion

In this chapter, the fundamental properties of the hydrogen ring clusters, i.e., H_3, H_7, and H_{11}, have been investigated by means of one-component approaches (UHF and UMP2) and two-component approaches (GHF and GMP2). In particular, the potential energy curves and spin expectation values of these molecules were evaluated.

Concerning the potential energy curves, GHF (GMP2) gives lower total energies in comparison with UHF (UMP2) because of the absence of preserved spin symmetry. Bound potential curves are obtained for UHF(LS), GHF, UMP2(LS), and GMP2, while repulsive curves are obtained for UHF(HS) and UMP2(HS). The potential well depths in UMP2(LS) and GMP2 are larger than those in UHF(LS) and GHF. All the curves converge to the correct and identical dissociation limit for each of the molecules.

The $\langle S_z \rangle$ values of UHF coincide with the exact eigenvalues of the S_z operator, because UHF preserves the S_z symmetry. The $\langle S_x \rangle$, $\langle S_y \rangle$, and $\langle S_z \rangle$ values of GHF are entirely zero, which indicates being the non-collinear solutions. From the $\langle S^2 \rangle$ values, it was revealed that UHF(HS) gives the eigenfunctions of the S^2 operator, while UHF(LS) and GHF give the spin-contaminated solutions, in particular, at long distances. Additionally, the GHF solutions are less spin-contaminated in comparison with the UHF(LS) solutions in the dissociation region.

References

[1] R. Seeger, J. A. Pople, *J. Chem. Phys.* **66**, 3045 (1977).

[2] H. Fukutome, *Int. J. Quantum Chem.* **20**, 955 (1981).

[3] J.-L. Calais, *Adv. Quantum Chem.* **17**, 225 (1985).

[4] R. McWeeny, Methods of Molecular Quantum Mechanics, Academic Press, London, 1989.

[5] P.-O. Löwdin, I. Mayer, *Adv. Quantum Chem.* **24**, 79 (1992).

[6] S. K. Wolff, D. Jayatilaka, G. S. Chandler, *J. Chem. Phys.* **103**, 4562 (1995).

[7] D. Jayatilaka, *J. Chem. Phys.* **108**, 7587 (1998).

[8] J. L. Stuber, J. Paldus, in: E. J. Brändas, E. S. Kryachko (Eds.), Fundamental World of Quantum Chemistry, Kluwer Academic Publishers, Dordrecht, 2003, p. 67.

[9] M. K. Armbruster, F. Weigend, C. van Wüllen, W. Klopper, *Phys. Chem. Chem. Phys.* **10**, 1748 (2008).

[10] J. J. Goings, F. Ding, M. J. Frisch, X. Li, *J. Chem. Phys.* **142**, 154109 (2015).

[11] M. Nakano, J. Seino, H. Nakai, *Chem. Phys. Lett.* **657**, 65 (2016).

[12] D. Yamaki, Y. Shigeta, S. Yamanaka, H. Nagao, K. Yamaguchi, *Int. J. Quantum Chem.* **80**, 701 (2000).

[13] C. A. Jiménez-Hoyos, T. M. Henderson, G. E. Scuseria, *J. Chem. Theory Comput.* **7**, 2667 (2011).

[14] M. Nakano, J. Seino, H. Nakai, *Chem. Phys. Lett.* (submitted).

[15] F. Ding, J. J. Goings, M. J. Frisch, X. Li, *J. Chem. Phys.* **141**, 214111 (2014).

[16] C. A. Jiménez-Hoyos, T. M. Henderson, T. Tsuchimochi, G. E. Scuseria, *J. Chem. Phys.* **136**, 164109 (2012).

[17] S. Yamanaka, D. Yamaki, Y. Shigeta, H. Nagao, Y. Yoshioka, N. Suzuki, K.

Yamaguchi, *Int. J. Quantum Chem.* **80**, 664 (2000).

[18] S. Yamanaka, D. Yamaki, S. Kiribayashi, K. Yamaguchi, *Int. J. Quantum Chem.* **85**, 421 (2001).

[19] C. A. Jiménez-Hoyos, R. Rodriguez-Guzmán, G. E. Scuseria, *J. Phys. Chem. A* **118**, 9925 (2014).

[20] T. Kawakami, R. Takeda, S. Nishihara, T. Saito, M. Shoji, S. Yamada, S. Yamanaka, Y. Kitagawa, M. Okumura, K. Yamaguchi, *J. Phys. Chem. A* **113**, 15281 (2009).

[21] S. Yamanaka, R. Takeda, K. Yamaguchi, *Polyhedron* **22**, 2013 (2003).

[22] K. Yamaguchi, T. Fueno, *Chem. Phys. Lett.* **168**, 56 (1990).

[23] P. Lykos, G. W. Pratt, *Rev. Mod. Phys.* **35**, 496 (1963).

[24] Gaussian 09, Revision A.02, M. J. Frisch, G. W. Trucks, H. B. Schlegel, G. E. Scuseria, M. A. Robb, J. R. Cheeseman, G. Scalmani, V. Barone, G. A. Petersson, H. Nakatsuji, X. Li, M. Caricato, A. Marenich, J. Bloino, B. G. Janesko, R. Gomperts, B. Mennucci, H. P. Hratchian, J. V. Ortiz, A. F. Izmaylov, J. L. Sonnenberg, D. Williams-Young, F. Ding, F. Lipparini, F. Egidi, J. Goings, B. Peng, A. Petrone, T. Henderson, D. Ranasinghe, V. G. Zakrzewski, J. Gao, N. Rega, G. Zheng, W. Liang, M. Hada, M. Ehara, K. Toyota, R. Fukuda, J. Hasegawa, M. Ishida, T. Nakajima, Y. Honda, O. Kitao, H. Nakai, T. Vreven, K. Throssell, J. A. Montgomery, Jr., J. E. Peralta, F. Ogliaro, M. Bearpark, J. J. Heyd, E. Brothers, K. N. Kudin, V. N. Staroverov, T. Keith, R. Kobayashi, J. Normand, K. Raghavachari, A. Rendell, J. C. Burant, S. S. Iyengar, J. Tomasi, M. Cossi, J. M. Millam, M. Klene, C. Adamo, R. Cammi, J. W. Ochterski, R. L. Martin, K. Morokuma, O. Farkas, J. B. Foresman, and D. J. Fox, Gaussian, Inc., Wallingford CT, 2016.

[25] T. H. Dunning Jr., *J. Chem. Phys.* **90**, 1007 (1989).

[26] F. Jensen, Introduction to Computational Chemistry, Wiley, Chichester, 2007.

Chapter 8

General conclusion

In this thesis, the author developed and discussed highly accurate and efficient SD two-component relativistic wavefunction methods to enable black-box treatment to be applied to all the elements in the periodic table.

In Chapter 3, four SCF acceleration algorithms, i.e., the damping, DIIS, EDIIS, and EDIIS+DIIS methods, were extended to the GHF method. Then, the SCF convergence behavior of GHF was examined for He–Lr atoms and metal complexes including $W(CO)_6$, Cr_3, and UF_4. Numerical assessments showed that the EDIIS+DIIS method led to more stable convergence of the SCF calculations with fewer iterations than the other acceleration algorithms for all the test systems.

In Chapters 4 and 5, the KUHF and KROHF methods were developed as new choices for two-component HF calculations for open-shell systems. The KUHF and KROHF methods were defined as relativistic analogies of the UHF and ROHF methods, respectively, using quaternion algebra. The use of quaternion algebra allows the KUHF and KROHF wavefunctions to partially and fully satisfy time-reversal symmetry, respectively, while the GHF wavefunction satisfies no symmetry. Furthermore, the MSs of KUHF and KROHF are formulated on paired spin bases, termed pseudo-alpha and pseudo-beta spin bases, which are represented by the superposition of alpha and beta spin bases. Numerical assessments for coinage metal atoms and pnictogen atoms showed that the total energies of KUHF, KROHF, and GHF were similar but slightly different: the magnitudes of the total energies varied in the order of GHF < KUHF < KROHF. The

spinor energies of KUHF were close to those of GHF, showing $(2j+1)$-fold degeneracies, which confirmed that the SO interactions were descried appropriately. The potential energy curves for HAt showed that KUHF gave similar spin states to those seen in UHF, while GHF gave completely hybridized spin states. The test calculations for d- and f-block atoms demonstrated that SCF convergence in KUHF was several times more rapid than in GHF.

Furthermore, numerical assessments for pnictogen and d- and f-block atoms revealed that the spinor energies and SCF convergence behavior in KROHF strongly depended on the choice of coupling parameters used to construct the Fock matrix. While the choice of the parameter set affected the absolute values of the spinor energies, all parameter sets led to spinor energies with $(2j+1)$-fold degeneracies, indicating that the SO interactions were properly described. The PGB set, which was formulated to satisfy KT, gave physically reasonable spinor energies. However, the GS set showed the most rapid SCF convergence behavior of all the sets. This dilemma was solved by simply switching the parameter set from GS to PGB during the SCF cycles. The SCF convergence behavior in this procedure was superior to that in GHF, although inferior to that in KUHF.

In Chapter 6, a universal formulation of the GMP2 method was derived in accordance with two-component many-electron Hamiltonians to describe the full relativistic effects, i.e., the SF one-electron, SF-two-electron, SD one-electron, and SD two-electron relativistic effects. Based on this general formulation, a GMP2 code combined with the IODKH/NR and IODKH/IODKH Hamiltonians in the SF and SD formalisms was further implemented. Numerical assessments for He-like and Ne-like atoms and 16 typical diatomic molecules using various levels of Hamiltonians showed that the inclusion of the two-electron relativistic terms, as well as the one-electron terms, resulted in a systematic

improvement of the MP2 correlation energies. The MP2 correlation energies obtained using the SD-IODKH/IODKH Hamiltonian agreed particularly well with those from the four-component DC Hamiltonian. Furthermore, the GMP2 method with the SD-IODKH/IODKH Hamiltonian was shown to be computationally more efficient than the four-component MP2 method with the DC Hamiltonian.

In Chapter 7, the fundamental properties of equilateral hydrogen rings were investigated as an application study of two-component methods. In particular, the behaviors of the potential energy curves and spin expectation values with respect to the bond length were compared between the one- (UHF and UMP2) and two-component (GHF and GMP2) calculations. GHF and GMP2 gave lower total energies than UHF and UMP2, respectively, because of the absence of any symmetry constraints. Concerning the spin expectation values, while UHF showed non-zero $\langle S_z \rangle$ values, GHF showed zero values for $\langle S_x \rangle$, $\langle S_y \rangle$, and $\langle S_z \rangle$, reflecting the frustrated spin character. From the $\langle S^2 \rangle$ values, GHF was shown to give solutions that were less spin-contaminated than those of UHF at large bond lengths.

The series of studies presented in this thesis enhance the applicability of SD two-component relativistic wavefunction methods from the viewpoint of accuracy, efficiency, and versatility. The DIIS-based acceleration algorithms improve the SCF convergence of GHF; KUHF and KROHF provide new, simpler choices of a reference wavefunction with better SCF convergence behavior than in GHF; and the present GMP2 reproduces the parent four-component results with less computational cost. Indeed, the utility of the GHF-based methods has also been demonstrated by the application study of frustrated spin systems. Thus, a cornerstone of practical SD two-component relativistic quantum chemistry for all the elements in the periodic table has now been established.

To date, it is a well-known fact that SD interactions play a crucial role in phosphorescence, inter-system crossing, spin crossover, and many other spin-related phenomena. Through the extension to excited-state theories, the present methodologies for the ground state are expected to be applied for the theoretical analysis of these phenomena or theoretical molecular design for, e.g., highly efficient organic luminescent materials.

Furthermore, non-collinear spin states described by the two-component methods discussed herein are vital for new generation matters such as topological materials and quantum spin liquids, which are suggested to be a key of quantum computer, high-temperature superconductor, and so forth. The author hopes that the theoretical methodologies developed in this thesis will assist the exploration of the next frontier of material science.

Acknowledgements

本研究は早稲田大学先進理工学部化学・生命化学科、中井浩巳教授のご指導のもとで行われました。中井教授には研究室配属以来の 6 年間、研究に対する姿勢や考え方をはじめ、一人の責任ある大人としてのあり方に至るまで、多くのことを熱心に教えていただきました。本論文の執筆にあたりましても、数多くのご助言をいただきました。

同学科の古川行夫教授、井村考平教授には、本論文の審査にあたり副査を務めていただきました。先生方にはご多忙ながらも丁寧に査読していただき、貴重なご指導を賜りました。心より感謝いたします。第 2.8 節の研究を推進するにあたり、イリノイ大学アーバナ・シャンペーン校の平田聡教授には貴重なご指導およびご協力をいただきました。イリノイ大学での滞在を通じ、数多くの刺激を受けました。

中井研究室のスタッフおよび先輩方には日頃より大変お世話になりました。特に本論文の全体に渡りまして、所属する「相対論班」のリーダーである清野淳司博士には、研究テーマ、プログラムの作り方、学会発表や論文執筆の細部に至るまで、研究に関するあらゆる事柄に関して一から懇切丁寧にご指導いただきました。吉川武司博士には共にイリノイ大学に訪問していただき、第 2.8 節の研究に限らず、日頃より親身になって数多くのご指導をいただきました。また、今村穣博士、菊池那明博士、小林正人博士、赤間知子博士、西澤宏晃博士、五十幡康弘博士、石川敦之博士、王祺博士、西村好史博士、小野純一博士、大越昌樹博士、周建斌博士の皆様、および研究室秘書の小河原侑子さん、吉村真由美さん、池田麻由理さんに感謝いたします。

同輩である中嶋裕也博士は、学部生時代より互いに切磋琢磨し、共に博士後期

課程に進学しました。大学生活を通して、良きライバルであり、良き相談相手であった中嶋博士に感謝いたします。優秀な後輩諸君にも恵まれ、特に「相対論班」のメンバーには研究に限らず日々の生活においても様々お世話になりました。速水雅生修士には研究やプログラム実装にあたり多くの議論を交わしていただきました。中村亮太修士には第 5 章の研究に関して数多くの協力をいただきました。

また、2015 年度においては、早稲田大学理工学術院総合研究所「アーリーバードプログラム」による研究費の補助をいただき、円滑に研究を進めることができました。ここに御礼申し上げます。

最後に、長年の学生生活を許容し、精神的・経済的に支え続けてくれました家族に感謝いたします。

2017 年 3 月

List of achievements

Original articles

○ 1. “Assessment of self-consistent field convergence in spin-dependent relativistic calculations”

M. Nakano, J. Seino, H. Nakai, *Chem. Phys. Lett.* **657**, 65 (2016).

○ 2. “Development of spin-dependent relativistic open-shell Hartree–Fock theory with time-reversal symmetry (I): The unrestricted approach”

M. Nakano, J. Seino, H. Nakai, *Int. J. Quantum Chem.* **117**, e25356 (2017).

○ 3. “Development of spin-dependent relativistic open-shell Hartree–Fock theory with time-reversal symmetry (II): The restricted open-shell approach”

M. Nakano, J. Seino, H. Nakai, *Int. J. Quantum Chem.* **117**, e25366 (2017).

○ 4. “Universal formulation of second-order generalized Møller–Plesset perturbation theory for a spin-dependent two-component relativistic many-electron Hamiltonian”

M. Nakano, J. Seino, H. Nakai, *Chem. Phys. Lett.* **675**, 137 (2017).

Presentations

International conferences/symposia

1. “Relativistic spin-dependent open-shell Hartree–Fock theory with time-reversal symmetry: Unrestricted and restricted approaches”

   M. Nakano, R. Nakamura, J. Seino, H. Nakai, Current Trends and Future Directions in Relativistic Many Electron Theories (RMET2016), Tokyo (Japan), Sep. 2016 [Invited Lecture].

2. “Relativistic open-shell Hartree–Fock theory with time-reversal symmetry”

   M. Nakano, R. Nakamura, J. Seino, H. Nakai, The International Chemical Congress of Pacific Basin Societies (Pacifichem 2015), Hawaii (USA), Dec. 2015.

3. “Large-scale MP2 calculation based on spin-dependent two-component Hamiltonian and divide-and-conquer approach”

   M. Nakano, J. Seino, H. Nakai, 5th Japan–Czech–Slovakia International Symposium on Theoretical Chemistry, Nara (Japan), Dec. 2013.

4. “Development of Electron Correlation Theory Based on Spin-Dependent Two-Component Hamiltonian”

   M. Nakano, J. Seino, H. Nakai, 6th Asia–Pacific Conference of Theoretical and Computational Chemistry (APCTCC 6), Gyeongju (Korea), Jul. 2013.

Domestic conferences/symposia

1. “スカラー相対論法に基づく分割統治型電子相関プログラムの自動実装”
   吉川武司, 中野匡彦, 平田聡, 中井浩巳, 第 10 回分子科学討論会, 兵庫, 2016 年 9 月.
2. “Koopmans の定理と時間反転対称性を同時に考慮した相対論的開殻 Hartree–Fock 法”
   中村亮太, 中野匡彦, 清野淳司, 中井浩巳, 日本コンピュータ化学会 2015 春季年会, 東京, 2015 年 5 月.
3. “Kramers 制限を課した相対論的開殻 Hartree–Fock 法の開発”
   中野匡彦, 中村亮太, 清野淳司, 中井浩巳, 第 18 回理論化学討論会, 大阪, 2015 年 5 月.
4. “時間反転対称性を利用した新規相対論的開殻 Hartree–Fock 法の開発 : KUHF 法”
   中野匡彦, 清野淳司, 中井浩巳, 日本化学会第 95 春季年会, 千葉, 2015 年 3 月.
5. “時間反転対称性を利用した新規相対論的開殻 Hartree–Fock 法の開発 : KROHF 法”
   中村亮太, 中野匡彦, 清野淳司, 中井浩巳, 日本化学会第 95 春季年会, 千葉, 2015 年 3 月.
6. “スピン－軌道相互作用を露わに考慮した大規模・高精度な相対論的量子化学計算法の開発”
   中野匡彦, 清野淳司, 中井浩巳, 第 4 回 CSJ 化学フェスタ 2014, 東京, 2014 年 10 月.
7. “相対論的電子相関計算における picture change 効果”
   中野匡彦, 清野淳司, 中井浩巳, 日本化学会第 94 春季年会, 愛知, 2014 年 3 月.

8. “CO_2 化学吸収法における吸収・放散反応機構の理論的解明”

寺西慶, 中嶋裕也, 中野匡彦, 佐藤裕, 中井浩巳, 東京, 第 3 回 CSJ 化学フェスタ 2013, 2013 年 10 月.

9. “相対論効果と電子相関効果を同時に取り込んだ大規模計算法の開発”

中野匡彦, 清野淳司, 中井浩巳, 第 7 回分子科学討論会, 京都, 2013 年 9 月.

10. “スピン依存 2 成分相対論法に基づく分割統治型電子相関理論の開発”

中野匡彦, 清野淳司, 中井浩巳, 日本コンピュータ化学会 2013 春季年会, 東京, 2013 年 5 月.

11. “一般化スピン軌道に対応した分割統治法に基づく大規模電子相関計算手法の開発”

中野匡彦, 清野淳司, 中井浩巳, 第 16 回理論化学討論会, 福岡, 2013 年 5 月.

12. “スピン依存 2 成分相対論的ハミルトニアンに対応した分割統治型電子相関理論の開発”

中野匡彦, 清野淳司, 中井浩巳, 日本化学会第 93 春季年会, 滋賀, 2013 年 3 月.

13. “QED 効果を取り入れた 2 電子 Gaunt–Pauli 近似の精度検証”

清野淳司, 中野匡彦, 中井浩巳, 第 15 回理論化学討論会, 宮城, 2012 年 5 月.

14. “スピン依存 2 成分相対論に基づく電子相関計算手法の開発”

中野匡彦, 清野淳司, 中井浩巳, 第 15 回理論化学討論会, 宮城, 2012 年 5 月.

15. “スピン依存 2 成分相対論法に対応した電子相関理論の開発”

中野匡彦, 清野淳司, 中井浩巳, 日本コンピュータ化学会 2012 春季年会, 東京, 2012 年 5 月.

16. “二成分相対論法に基づく一般化電子相関理論の開発”

中野匡彦, 清野淳司, 中井浩巳, 日本化学会第 92 春季年会, 神奈川, 2012 年 3 月.

Awards

1. 卒論発表賞, 早稲田大学 先進理工学部 化学・生命化学科, 2012 年 3 月.
2. Best Poster Award, 6th Asia–Pacific Conference of Theoretical and Computational Chemistry (APCTCC 6), 2013 年 7 月.
3. 最優秀ポスター発表賞, 第 4 回 CSJ 化学フェスタ, 2014 年 11 月.
4. 学生講演賞, 日本化学会第 95 春季年会, 2015 年 4 月.
5. Student Poster Competition Award, The International Chemical Congress of Pacific Basin Societies (Pacifichem 2015), 2015 年 12 月.